Using embedded energy-harvesting nanodevices for neural data communications in the human body

Foirfe chun fónaimh
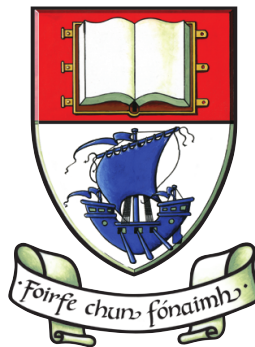
Michael Donohoe, BSc.

School of Science and Computing

Waterford Institute of Technology

This thesis is submitted for the degree of

Doctor of Philosophy

Supervisors: Dr. Brendan Jennings and Dr. Sasitharan Balasubramaniam

April 2020

I would like to dedicate this Thesis to my wife Brenda, daughter Olivia and son Aidan.

Mo bhean, mo chlann, mo neart.

Declaration

I hereby certify that this material, which I now submit for assessment on the programme of study leading to the award of Doctor of Philosophy, is entirely my own work and has not been taken from the work of others save to the extent that such work has been cited and acknowledged within the text of my work.

<div align="right">

Michael Donohoe, BSc.

April 2020

</div>

Acknowledgements

Abstract

Implanted biomedical devices are an important part of the diagnosis and treatment of human illnesses. Such devices need electrical power for operation, transmission systems for data communications and a high level of bio-compatibility to reduce the possibility of inflammation. Powering by battery is widely used but requires removal of the device from the body for battery renewal. Wireless electromagnetic (EM) systems are also in common use but are subject to tissue absorption and potential tissue heating. It would be preferable to use some form of energy-harvesting for power and a more biocompatible method for data communications.

This Thesis proposes the use of ultrasound as a method of providing in-body energy harvesting for an implanted device at a shallow depth of tissue. The medical use of ultrasound for imaging is widespread, well understood and has recommended safety levels. Arrays of devices containing piezoelectric nanowires can convert incident ultrasound energy into electrical pulses. These pulses can stimulate a nerve to generate a stream of modulated signals along the nerve and deliver data packets to a more deeply embedded receiver. The maximum bit rate is 200 bit/s, limited by the rate at which nerves can generate electrical signals. The proposed modulation is simple on-off keying (OOK) to create a stream of logic "ones" and "zeroes". The send and receive timing is asynchronous and the direction of transmission is one-way so no re-sending of faulty packets can be supported.

We model a specific scenario of a stimulus system on the vagus nerve in the neck sending modulated data pulses to an embedded, multi-reservoir drug-delivery system in the brain. The drug-delivery system could use cerebrospinal glucose as a source for energy harvesting. Forward error correction is analysed as a potential method to improve transmission performance. The overall energy-harvesting and communications system is simple, biocompatible and safe.

Publications

- Michael Donohoe, Sasitharan Balasubramaniam, Brendan Jennings, and Josep Miquel Jornet. *Powering In-body Nanosensors with Ultrasounds.*
  IEEE Transactions on Nanotechnology 15(2):151-154, March 2016.

- Michael Donohoe, Brendan Jennings, Josep Miquel Jornet, and Sasitharan Balasubramaniam. *Nanodevice Arrays for Peripheral Nerve Fascicle Activation Using Ultrasound Energy-harvesting.*
  IEEE Transactions on Nanotechnology 16(6):919-930, Nov 2017.

- Michael Donohoe, Brendan Jennings, and Sasitharan Balasubramaniam. *Capacity Analysis of a Peripheral Nerve using Modulated Compound Action Potential Pulses.*
  IEEE Transactions on Communications 67(1):154-164, Jan 2019.

- Michael Donohoe, Brendan Jennings, and Sasitharan Balasubramaniam. *Deep Brain Drug-delivery Control using Vagus Nerve Communications*
  Elsevier Computer Networks 171:107137, April 2020.

.

Contents

List of Figures

List of Tables

List of Acronyms

AET acoustic energy transfer.

ANC autonomous neural control.

AP action potential.

ATP adenosine triphosphate.

AWGN additive white Gaussian noise.

BAN body area network.

BBB blood brain barrier.

BCH Bose-Chaudhuri-Hocquenghem.

BER bit error rate.

BMI brain-machine interface.

CAP compound action potential.

CMOS complementary metal-oxide-semiconductor.

DBS deep brain stimulation.

DC direct current.

DPIM digital pulse interval modulation.

EM electromagnetic.

FEC forward error correction.

FSK frequency shift keying.

ISI inter-symbol interference.

ISM industrial scientific medical.

MAC medium access control.

MC molecular communications.

MCU microcontroller unit.

MICS medical implant communications system.

OOK on-off keying.

PAM pulse amplitude modulation.

PPM pulse position modulation.

PWM pulse width modulation.

PZT lead zirconate titanate.

RF radio frequency.

RS Reed-Solomon.

SNR signal to noise ratio.

TEC time elapse communication.

UART universal asynchronous receiver/transmitter.

VNS vagus nerve stimulation.

ZnO zinc oxide.

Chapter 1

Introduction

Bioelectronic medicine is spearheading a new approach in the diagnosis and treatment of human illnesses and injuries. The objective is to use implanted electronic devices to detect and measure neural electrical activity and/or other metabolic indicators such as temperature and hormone concentration. This collected information may then be processed and used to provide new diagnostic and treatment options for patients. The nervous system in particular can provide valuable diagnostic information since all major organs and muscles of the body are naturally innervated, allowing the brain to both monitor and regulate organ and muscle function. Nerve recording devices could use neural activity detected from the brain or other organs to deliver an appropriate response, modulate a change in organ function and restore health, without the side effects of drug therapies. If a drug must be administered, then an implanted device could be used to deliver the smallest possible dosage of a specific drug as close as possible to the required area in response to detected metabolic changes or neural activity patterns.

A major feature of bioelectronic solutions is the requirement for devices that can be implanted long-term within patients and enable them to live a normal, mobile lifestyle. The devices must be as compact as possible and minimise the possibility of inflammation or rejection. If the implanted device is not wired to an external controller and power supply, then two key issues that arise are (i) continued powering for a self-contained system and (ii) communications for sending instructions and receiving data. The power requirements may be intermittent, depending on the device, but the power supply would have to deliver variable power levels over the longer term using safe non-toxic components. The communications system should also provide sufficient data-transmission capacity, depending on the function of the device, without any medical side-effects. Ideally the device should (i) harvest energy from either the

immediate bio-environment or an external source, avoiding the need for batteries that must be replaced and (ii) use a communications system that is as bio-compatible as possible to minimise the effect, for example, of EM radiation on body tissue. Energy harvesting from the bio-environment would include sources such as thermal (body-heat), mechanical (muscle movement) or bio-chemical (glucose). External energy-harvesting sources include electromagnetic radiation and ultrasound. All of these sources must be capable of providing the power requirements of the implant whenever the need arises. An implant should be able to maintain a low-power sleep mode until called upon to perform a particular function, at which point there would be a surge in demand for power. The external sources are more controllable than internal sources and have the advantage of readily variable intensity. However, an internal source may have more constant availability and be better placed to respond to a sudden power demand. These considerations must be balanced when choosing a power source for harvesting.

The main natural communications paths within the body are the nervous system and the cardiovascular system. The nervous system carries electrical signals to and from the brain in response to internal and external stimuli. These electrical signals can be artificially generated by an implant, at a shallow depth, delivering electrical stimulus pulses to the nerve. In this way, the nervous system could be used as a digital data communications path, if stimulated neural signals were modulated to deliver data packets to an implanted device at a deeper level. This would avoid the need for using conventional wireless communications, although the data rate would be limited by neural physiology. These two topics of energy harvesting for biomedical devices and the use of the nervous system to convey digital data are the central themes of this Thesis.

1.1   Research Hypothesis

Energy harvesting by implanted devices from an external source can be achieved in different ways. The external energy must be able to safely penetrate human tissue and then be converted into electrical energy. Ultrasound provides a safe and practical energy source in relation to the human body and the mechanisms of absorption are well understood. Communicating using the nervous system is also seen as a viable and biocompatible method to deliver commands to an implanted medical device. A more deeply implanted receiving device, shielded by muscle or bone, may not be accessible

by ultrasound so an alternative method of energy-harvesting (e.g. glucose harvesting) would be needed. The overall research hypothesis may be stated as follows:

An ultrasound beam directed into the human body can deliver power to energy-harvesting implanted devices at a shallow tissue depth. The resulting electrical pulses can be used to stimulate specific nerves and create an in-body communications system. A modulated stimulus pattern can be transmitted along a peripheral or cranial nerve and deliver simple activation commands to an embedded drug-delivery system. The drug-delivery system, in turn, could be powered by glucose harvesting.

The research hypothesis is subdivided into five Research Questions that form the basis for the content of this Thesis.

1.1.1   First Research Question

How might ultrasound be used to power implanted devices and what frequencies are preferable?

Ultrasound is used at present for imaging in the human body and there are specific safe-level recommendations of intensity to avoid tissue damage. The ultrasound beam is also a potential energy source that could be harvested by a medical implant once a suitable transducer is identified. The beam intensity reduces with depth through absorption and reflection, reducing the amount of energy that would reach an implanted device. The absorption of the beam is also a function of frequency. This research question analyses the specific use of piezoelectric nanowire devices ("nanodevices"), implanted at a shallow depth, for harvesting ultrasound energy and the potential power output of such devices over a range of ultrasound frequencies.

1.1.2   Second Research Question

How may ultrasound energy-harvesting devices be configured and placed to stimulate a peripheral nerve?

A peripheral nerve in the human body contains bundles of neurons called *fascicles*. Neurons need a minimum level of stimulus current and voltage to be applied in order to create an electrical propagating action potential (AP). This research question seeks to quantify the levels of current and voltage needed to stimulate neurons of different types and diameters at different depths in a peripheral nerve. The question also addresses the fact that an individual piezoelectric nanodevice may not produce sufficient voltage and current to evoke the response. Consequently, multiple devices must then be configured

to deliver the required stimulus voltage and current levels. This nanodevice array must be placed in very close proximity to the nerve, with the minimum amount of tilt in order to maximise the energy-harvesting potential. It must also be encased in a bio-compatible material to minimise the risk of inflammation or rejection.

1.1.3 Third Research question

What is the magnitude and range of the stimulated neural pulse produced by a nanodevice array?
Stimulating a nerve creates APs that propagate along each neuron within a fascicle. The individual APs propagate without attenuation as they are regenerated at regular intervals along the neuron. The collective voltage measured outside the nerve from all the underlying APs is called a compound action potential (CAP). This research question analyses the behaviour of individual and collective neurons when stimulated, and quantifies the characteristics of the resulting CAP when measured at varying distances from the stimulating point. The suitability of such pulses for data transmission is then assessed.

1.1.4 Fourth Research Question

What is the digital data transmission capacity of a nerve and what forms of modulation can be used ?
The CAP of a stimulated nerve could be viewed as a potential data pulse once the range and magnitude for different ensembles of neurons has been determined. The system is unidirectional and low speed, constrained to a limited rate of AP generation by the underlying neural physiology. This research question applies communications theory to determine the maximum bit-rate and transmission range of neural CAP pulses subject to varying levels of background noise. The question also evaluates three different methods of modulation that could be applied to a stream of CAPs to determine their potential throughput.

1.1.5 Fifth Research Question

What form of receiver could be used and how might it be powered?
The neural communications system is limited in speed and capacity, but it could still deliver simple single-byte instructions to a deeper implanted device such as a drug-delivery system. A unidirectional neural transmission system would require some form of forward error correction (FEC), since resending faulty packets is not possible.
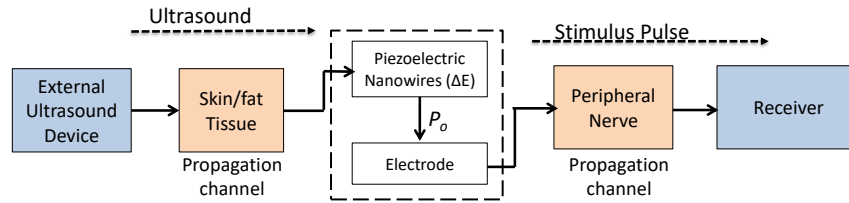
Fig. 1.1 Block diagram of end-to-end path from the ultrasound source to the receiver.

This research question uses a specific scenario of vagus nerve stimulation to answer how a multi-reservoir drug-delivery system in the brain might be activated by short data packets that could incorporate error control. The metabolic cost in terms of the use of adenosine triphosphate (ATP) to carry APs is also calculated. Powering the drug-delivery by glucose harvesting is examined as an alternative to battery powering. An overview of the neural transmission system is shown in Fig. 1.1. Harvested ultrasound energy is converted by piezoelectric nanodevice arrays and releases an electronic pulse that stimulates a peripheral nerve through an electrode. The pulse then is transmitted along the nerve and detected at the remote end by a receiver. The pulses are decoded as packets delivering commands to a drug-delivery system.

1.2   Research Contributiom

The research work was based on the development of mathematical models for ultrasound energy harvesting, nanodevice configuration, neural stimulation, neural data capacity calculation, ATP consumption, forward error correction and glucose harvesting. Coding of the models and plotting of results was done in Matlab. The specific research contributions that were developed in order to answer the research questions are listed below.

- **Power Harvesting**: The modelling of ultrasound in the human body for power harvesting requires calculating the intensity of different ultrasound frequencies at different tissue depths to determine the effects of tissue absorption and beam frequency. These calculated intensities then provide input to a mathematical model to determine the voltage and current generated when an ultrasound beam bends a piezoelectric ZnO nanowire. The model is extended to plot the relationship between the ultrasound beam intensity and the current/voltage output of a $1000\mu m^2$ energy harvesting nanodevice with 20,000 nanowires.

- **Neural Stimulation**: The minimum levels of voltage and current needed to stimulate neurons of different diameters are used as input to calculate nerve stimulation at different depths of penetration into the nerve. A novel array of nanodevices, coupled in series and parallel, is then modelled to produce sufficient levels of voltage and current to stimulate such peripheral nerves. The voltage and current can be varied with the ultrasound intensity and the model shows how higher levels of voltage and current penetrate deeper into a nerve and also selectively stimulate smaller diameter neurons. The effect of tilt on the output of the nanodevice array is also calculated.

- **Neural Data Pulse**: The stimulation of individual neurons is modelled to calculate the extracellular voltage of an AP propagating along a neuron. The relationship between the speed of an AP and neuron diameter is used derive a dispersion model. A spread of modelled APs is generated and summed into a CAP. An equivalent Gaussian pulse model for a simulated CAP captures both the the attenuation of the CAP and the pulse spreading resulting from dispersion. Transmission theory is applied to calculate the signal to noise ratio (SNR) and the maximum possible data throughput of a stream of CAP pulses. Three different modulation methods were analysed: on-off keying (OOK), pulse position modulation (PPM) and digital pulse interval modulation (DPIM) using the Gaussian pulse model.

- **Drug-delivery**: The specific scenario of CAP pulses along the vagus nerve is simulated and the metabolic cost in terms of ATP is calculated. Different methods of FEC are applied to the CAP bitstream to assess any performance improvement and a data packet for a drug-delivery system is presented. The coding gain for FEC is expressed in terms of bit error rate (BER) improvement at a particular SNR and transmission range. The flux of glucose needed in cerebrospinal fluid to produce levels of power for a brain implant is calculated and analysed.

1.3   Thesis Organisation

This document is organised as follows:

- **Chapter 2** provides an overview of current developments in medical implant devices. The different methods of powering and communications are described as well as functions such as neural stimulation, neural recording and

6

drug-delivery. There is also background information on ultrasound, glucose harvesting, the generation of neural APs and molecular communications. A literature review describes research in powering, communications, neural stimulation and recording, drug-delivery, neural data communications and molecular communications.

- **Chapter 3** address the first research question, setting out (i) the rationale for using lower frequency 50 kHz ultrasound as an energy source, (ii) the transmission of ultrasound through human tissue and (iii) the use of piezoelectric nanowire devices as the basis for energy harvesting.

- **Chapter 4** addresses the second research question, modelling how arrays of energy harvesting nanodevices can be coupled together to provide the necessary levels of voltage and current to stimulate a peripheral nerve to different depths.

- **Chapter 5** addresses the third and fourth research questions, modelling the generation of a neural data pulse and determining how the amplitude decreases with transmission distance. Three forms of modulation are described and the resulting capacity and transmission ranges are determined subject to the noise levels that might exist.

- **Chapter 6** addresses the fifth research question, describing a modelled scenario for delivering commands to a multi-reservoir drug-delivery system in the brain via the stimulation of the vagus nerve in the neck. The transmission path is unidirectional and the use of FEC is explored as a method of improving performance. Ultrasound will not penetrate the skull so the potential use of glucose harvesting for powering the brain implant is analysed.

- **Chapter 7** provides summary conclusions to the research work and also proposals for future work.

Chapter 2

Background

2.1 Introduction

The key elements of the research hypothesis are (i) the use of ultrasound to deliver power to a neural stimulus system, (ii) the transmission of modulated neural pulses along a nerve to communicate with a more deeply embedded device and (iii) the delivery of drugs in the brain in response to neurally transmitted instructions. In this chapter the current state of development and research into the types of medical implant that can be deployed is outlined with particular emphasis on powering and communications. Ultrasound generation and glucose energy-harvesting are described in detail to illustrate powering options. The mechanisms of neural stimulation are also described in some detail to illustrate a viable communications option. Research into micro and nano level implants is then described with emerging challenges in communications at a very small scale. Following that, a literature search on all these topics is provided in §2.3..

2.2 Medical Implant Devices

Medical implants embedded in the human body are used for *diagnostic*, *therapeutic* or *assistive* purposes (Andreu-Perez et al., 2015). Diagnostic devices are typically sensors that monitor health conditions such as neural activity, glucose levels and gastrointestinal functions. Therapeutic devices are currently used to treat a variety of medical conditions such as heart arrythmia (cardiac pacemaker), diabetes (insulin pump) and neurological conditions, such as Parkinson's Disease (neurostimulator) (Oluigbo et al., 2012). Assistive devices improve anatomical and physiological

functions such as hearing (cochlear implants), vision (bionic visual implants) and prosthetic limb control (brain-computer interface).

Stimulation of peripheral or cranial nerves is carried out by externally powered electrodes placed on the skin surface (*transcutaneous*) or under the skin (*subcutaneous*) in closer proximity to muscles or nerves (Mortimer and Bhadra, 2004). Electrodes can be single points or multiple arrays with variable voltage and current control. Single point subcutaneous electrodes may partially penetrate a peripheral nerve, or they may be attached as a strip to the nerve surface. A strip electrode may also be configured as a wrap-around cuff. The stimulus current levels for these electrodes can be minimised by placing them as close as possible to the main nerve tissue that needs to be stimulated. Subcutaneous systems require surgically implanted electrodes that are wired to a power and control unit to deliver measured amounts of voltage and current. Therapeutic stimulus implants such as heart pacemakers have been deployed for over 50 years. Newer models are more compact and programmable for different stimulus patterns (Seriwala et al., 2016). The implant is usually placed in a surgically created pocket below the clavicle (collarbone) and the electrodes are on leads that are threaded to the heart. At present most stimulus systems are open-loop, with the operating parameters set by a clinician based on trial-and-error.

Neural activity in different parts of the body can be detected and recorded by single or multiple electrodes. The recorded activity may be from natural processes or in response to specific stimuli. The recorded signals usually represent activity by a collection of neurons rather than single neurons. Recording of brain activity through internal or external electrodes is an important part of neurotherapy. These recordings can help to build up a picture of how different parts of the brain react to external stimuli and the information may be used in the development of prosthesis control. Programmable implanted devices make it easier to vary different input parameters but the goal is to develop *closed-loop systems* that can record neural activity and use this as feedback to adjust applied stimulus parameters automatically.

Therapeutic drugs are usually injected to the bloodstream or ingested in the form of a tablet. Some degree of automation can be provided by systems such as an insulin pump, a drug-delivery system that is worn externally and injects a measured amount of insulin at timed intervals. A closed-loop system would supply insulin in response to a signal from an attached glucose sensor (McAdams and Rizvi., 2016). Closed-loop diagnostic and therapeutic functions of this type may be combined in a device that is termed *theranostic*.

The methods used at present for powering and communicating with medical devices will depend on the frequency of the required treatment (acute or chronic) and the

preferred degree of portability that can be realistically implemented. The device can be externally wired to a combined powering and communications system with the wires penetrating the skin to access internal locations. This can be used for major interventions of a one-off nature or for research into a specific neural response. Alternatively, if continuous therapy is needed then a self-contained battery powered implant can deliver stimulus pulses or a measured amount of a drug in response to pre-set parameters.

There is a drive to develop miniature implants at the micro or nano scale that can be distributed within specific organs or areas of the body for theranostic purposes. These device clusters would communicate with each other and the external world to form the *internet of bio-nano things* (Akyildiz et al., 2015). The small size creates additional challenges in powering and communications. If microscopic batteries are not to be used then some form of energy harvesting is the only alternative. The small physical size would also restrict antenna size if EM communications is to be used. Consequently, alternative forms of bio-communication are being investigated, similar to those used in the nervous system, as viable methods for nanodevice communications.

2.2.1 Implant Powering

The majority of non-wired implants at present are powered by long-life batteries that cannot be re-charged *in situ*. An implant battery has to be replaced at regular intervals, requiring repeated surgical intervention. The alternative is to use some form of energy-harvesting to power the implant directly or to recharge a battery. Current research is directed at power provision through energy-harvesting from external sources (electromagnetic, vibrational) or internal sources such as muscle movement or glucose harvesting (see §2.2.3). Electromagnetic energy-harvesting can use near-field resonant magnetic coupling using coiled antennas at frequencies up to 20 MHz (Kim et al., 2017) but this is efficient only for short distances. The use of lower EM frequencies also results in the need for larger receiving antennas that will increase the size of the implanted device. Power may be delivered over a greater range using higher frequency mid-field (900 MHz) or far-field (2.5 GHz) EM powering. The use of EM power harvesting is subject to technical constraints to meet recommended safety levels (Rabaey et al., 2011) and prevent tissue damage through excessive heating of the implant. The specific absorption rate *(SAR)* describes the quantity of EM power that can be absorbed by a tissue and is defined as:

$$SAR = \frac{\sigma E^2}{\rho}. \tag{2.1}$$

The conductivity of the tissue is σ, the density is ρ and the electric field strength is E. The SAR value is expressed in Watts per kilogram and is averaged over 1 g or 10 g of tissue. In the US the exposure limits for an unrestricted environment, set by the FCC, are 4W/kg for 10g of tissue in the extremities (hands, wrists, feet, ankles) and 1.6 W/kg for 1 g of head, neck and trunk tissue. In other jurisdictions the equivalent ICNIRP and IEEE guidelines specify 2 W/kg for 10 g of head, neck and trunk tissue and 4 W/kg for 10 g of any other limbs (IEEE, 2019). The SAR limits can be converted to power intensities at different frequency ranges and a typical value is 2 W/m^2 for up to 200 MHz and 10 W/m^2 for frequencies greater than 200 MHz (IEEE, 2019). It would also require the wearing of an external powering source if true mobility was required. There are two options proposed for powering embedded nanosensors with ultrasound: (a) piezoelectric nanowires (Wang et al., 2007b) or (b) resonant piezoelectric crystals (Ozeri and Shmilovitz, 2010). Piezoelectric nanowires can be bent by a range of different ultrasound frequencies rather than responding to a specific resonant frequency. Lower frequencies will deliver more energy per cycle and hence are more likely to bend the nanowires. Lower frequencies will also be less subject to absorption in the tissue, but the conversion efficiency of the nanowires is low (<5%) and a larger transducer is needed to produce a lower frequency. Resonant crystals are more efficient at converting ultrasound into electrical energy (>50%) but operate best at higher frequencies where smaller crystals can be used. There are no commercially available implant systems using either of these options at present.
Other power harvesting proposals include thermal (body heat), mechanical (muscle movement) and glucose harvesting.

2.2.2 Ultrasound Generation

Ultrasound refers to frequencies above that of audible sound and nominally includes anything over 20 kHz. In nature, ultrasounds in the range 20-100kHz are commonly used for communication and navigation (sonar) by bats, dolphins and some other species. The speed of ultrasound in air, 331.5 ms^{-1} at sea level and 0°C, is the same as that of any other soundwaves (Hendee and Ritenour, 2003b).
An ultrasound wave is artifically generated when an electric field is applied to an array of piezoelectric crystals, usually lead zirconate titanate (PZT), located on a transducer surface. Electrical stimulation causes mechanical distortion of the crystals resulting in vibration and production of sound waves (i.e. mechanical energy) at a desired frequency (Hendee and Ritenour, 2003a). Efficiency in converting electrical energy to mechanical energy is 90% to 95%. if the resonant frequency of the crystal is applied.

Table 2.1 Rayleigh distance for different transducers and wavelengths.

Radius (mm)	Frequency (MHz)	Wavelength (mm)	R_d (mm)
5	0.5	30.8	0.8
5	1	1.54	16
10	0.5	30.8	3.25
10	1	1.54	65

A point source of ultrasound will radiate pressure waves in all directions (Hendee and Ritenour, 2003b). The initial signal intensity, I_0), will decrease over a distance, r, to a value of I_r according to an inverse square law as follows:

$$I_r = \frac{I_0}{4\pi r^2}. \tag{2.2}$$

Transducers can be designed to radiate sound in many different types of pattern, from omnidirectional to very narrow beams. For a transducer with a circular radiating surface, vibrating in phase, the beam can be shaped in order to narrow the area of transmission although some spreading will occur. An *unfocused* beam can be divided into a near-field *(Fresnel zone)* and a far-field *(Fraunhofer zone)*. In the near-field, the beam narrows from the width of the transducer down to a narrower focal area (Hendee and Ritenour, 2003a). The distance at which this happens is called the Rayleigh distance, R_d, and is is dependent on the transducer radius r_t and the wavelength of the ultrasound in the transmission medium λ as follows:

$$R_d = \frac{r_t^2}{4\lambda}. \tag{2.3}$$

The Rayleigh distance will increase at higher ultrasound frequencies (shorter wavelengths) for a fixed transducer radius as shown in Table 2.1. The wavelength is calculated from the frequency and the speed of sound in human tissue which is approximately 1540 m/s. Complicated interference patterns arise in the Fresnel zone and the intensity is highly variable. In the far-field the beam gradually spreads out and the intensity is more uniform, though decreasing. These effects can be mitigated by using an acoustic lens to focus the beam rather than operating in unfocused mode. Medical diagnostic ultrasound scans use frequencies between 1MHz and 15 MHz. The ultrasound is reflected from denser tissue and bone and detected by a receiver transducer. An image is then built up from the reflected signals. Ultrasound is also used for therapeutic purposes, especially by physiotherapists to promote injury healing.

2.2.3 Glucose Energy Harvesting

The availability of glucose as an energy source in the human body has focused attention on the harvesting of glucose to deliver power to medical implants (Cosnier et al., 2014). The constant supply of glucose from body fluids means that the harvesting can be continuous, as long as it does not seriously deplete the supply of glucose for other purposes. A glucose fuel cell generates energy by electrochemical reactions (oxidation and reduction) at two spatially separated electrodes (anode and cathode). Catalysts are required at the electrodes to enable the reactions. Electrons are released by the oxidation of the glucose at the anode and then flow through an external load to the cathode where the reduction reaction happens. Hydrogen ions (protons) pass from the anode to the cathode through an ion-selective membrane that provides two separate chambers for the electrodes (Rapoport et al., 2012). The complete oxidising of glucose to carbon dioxide (CO_2) and water (H_2O) would theoretically release 24 electrons per molecule of glucose. The reaction would be as follows:

Anode $C_6H_{12}O_6 + 6H_2O \longrightarrow 6CO_2 + 24H^+ + 24e^-$

Cathode $6O_2 + 24H^+ + 24e^- \longrightarrow 12H_2O$

Overall $C_6H_{12}O_6 + 6O_2 \longrightarrow 6CO_2 + 6H_2O$
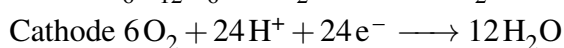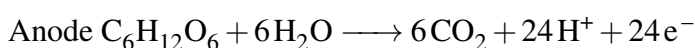
The change in the standard Gibbs free energy, ΔG, is $-2.870 \times 10^6 J/mol$. The reaction potential, V^0, is 1.24 V.

Glucose fuel cells can be divided into three main types depending on the catalyst used:

- *Enzymatic fuel cells* use enzymes such as glucose oxidase and laccase;

- *Microbial fuel cells* use electroactive micro-organisms;

- *Abiotically catalysed fuel cells* use non-biological metals (e. g. platinum) or carbon.

Microbial fuel cells are very efficient and are capable of completely oxidising glucose. They are not considered suitable for implants as they carry the risk of infection from the catalysing microorganism. Enzymatic fuel cells are the subject of research, but it is difficult to guarantee the stability of enzymes over a long period of use. The most favoured type is the abiotically catalysed cell, but this oxidises glucose to gluconic acid and releases only two electrons per glucose molecule. This delivers a lower value of $-2.51 \times 10^5 J/mol$ for the change in Gibbs free energy. Both oxygen and glucose are present in body fluids. The fuel cell construction has to ensure that the amount of oxygen is minimised and the amount of glucose is maximised at the anode. The reverse situation applies at the cathode. Separating the fuel and the oxidant reduces the risk of electrical shorting at the electrodes and improves the overall efficiency.

2.2.4 Implant Communications

If an implant has no wired communications connection then some form of wireless communication is usually employed (Ritter et al., 2014). Short range, near-field, inductive coupling at frequencies up to 20 MHz is used to transfer data from an implanted system while also providing inductive powering (Kim et al., 2017). There are power dissipation issues if the same frequency is used to power the implant (higher transmit power) as well as to communicate with it. At present many implanted devices communicate in the 402 - 405 MHz medical implant communications system (MICS) band with a range of up to 2 m (Teshome et al., 2019). The emerging development of body area network (BAN) provides for implants using the 2.5 GHz industrial scientific medical (ISM) band. Some commercially available devices (e.g. pacemakers) use Bluetooth technology in the ISM band for external communications. Higher EM frequencies experience greater absorption in the human body but they do provide for higher-capacity data links, especially for large-volume neural recordings. The antenna size for a given frequency places a limitation on how small an implant can be. Implants at the micro or nano scale would have to use even higher frequency radiation, like terahertz or infra-red, but this is very strongly absorbed by body tissues and would only be effective over extremely short ranges. An alternative would be to use the nervous system, described below in §2.2.5 and/or biologically based molecular communications, described in more detail in §2.2.6. It is likely that a future BAN will have a combination of the previous technologies for internal and external communications (Atakan et al., 2012) .

2.2.5 Neural Stimulation

The nervous system is one of the fundamental communications systems in the human body. The human nervous system has two broad divisions: (i) the *peripheral nervous system* providing sensing and muscle activation (motor) functions throughout the human body and (ii) the *central nervous system* (the brain and spinal cord) for processing sensory information and sending control signals to/from the peripheral nervous system through the spinal cord (Malmivuo and Plonsey, 1995). There is a third type of nerve, the cranial nerve, that connects the brain directly to certain organs (e.g. eye and facial muscles) without going through the spinal cord. Sensory nerves are described as *efferent* and motor nerves as *afferent*. The nervous system has two main types of cells: neurons for communications and glial cells for support and nutrition.
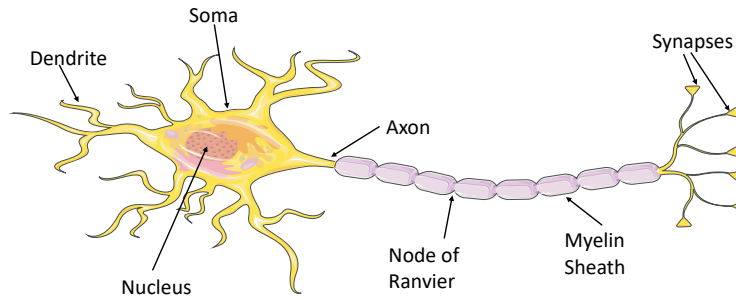
Fig. 2.1 Neuron structure

A neuron consists of *dendrites*, to receive messages from other neurons; a *soma*, or cell body with a nucleus; an *axon*, to transmit neural signals and *synapses* to form junctions with other neurons (Fig. 2.1). The *resting potential* of a neuron is based on an ionic balance of sodium and potassium ions across the neural membrane and has a magnitude of approximately -70 mV. A stimulus must raise this threshold to above -55 mV if a neural signal is to propagate (Malmivuo and Plonsey, 1995). A *sub-threshold stimulus* can also be applied to a neuron but it will not cause the neuron to activate.

The propagation of a sub-threshold pulse down a neuron can be modelled by cable theory. The neuron is divided into compartments and each compartment has an internal axial resistance, external axial resistance, membrane resistance and membrane capacitance. The difference between the external potential, ϕ_o, and the internal potential, ϕ_i at any given time is the membrane potential, V_m. If a neuron has a resting potential of V_r and a sub-threshold stimulus raises the membrane potential to V_m then the deviation in potential from the resting state, V', can be expressed as:

$$V' = V_m - V_r.$$ (2.4)

The cable equation shows the change in membrane voltage for small currents flowing through a neuron (Malmivuo and Plonsey, 1995). The simplest form is for the passive case where the current is sub-threshold and no ion channels in the neuron membrane are activated (Malmivuo and Plonsey, 1995). If a neuron experiences a change of V' in membrane potential from the resting state then the neural cable equation for a signal that has propagated a distance x along an axon may be expressed as follows:

$$\frac{\partial^2 V'}{\partial x^2} = (r_i + r_o)i_m$$ (2.5)

where r_i is the intracellular resistance of axoplasm per unit length of axon and r_o is the resistance of extracellular medium per unit length of axon. The membrane current i_m is the sum of an ionic membrane current i_{mI} and a capacitive membrane current i_{mC} and can be expressed as follows:

$$i_m = i_{mI} + i_{mC}$$
$$= \frac{V'}{r_m} + c_m \frac{\partial V'}{\partial t} \tag{2.6}$$

where r_m is the membrane resistance times unit length of axon and c_m is the membrane capacitance per unit length of axon. Substituting (2.6) into (2.5) we get:

$$\frac{1}{(r_i + r_o)} \frac{\partial^2 V'}{\partial x^2} = \frac{V'}{r_m} + c_m \frac{\partial V'}{\partial t}$$
$$\frac{r_m}{(r_i + r_o)} \frac{\partial^2 V'}{\partial x^2} = V' + r_m c_m \frac{\partial V'}{\partial t} \tag{2.7}$$
$$-\lambda^2 \frac{\partial^2 V'}{\partial x^2} + \tau \frac{\partial V'}{\partial t} + V' = 0.$$

The parameter τ is the *membrane time constant* while the parameter λ is defined as the *length constant*. Under steady-state conditions ($\partial V'/\partial t = 0$) we get an ordinary differential equation:

$$\frac{d^2 V'}{dx^2} - \frac{V'}{\lambda^2} = 0. \tag{2.8}$$

An infinite segment with $V' = V_0$ at $x = 0$ will have a solution of the form:

$$V' = V_0 e^{-x/\lambda}. \tag{2.9}$$

This shows that an initial stimulus voltage will attenuate along the membrane. The rate of attenuation with distance is determined by the length constant for that particular type of neuron. Length constants for non-myelinated mammalian axons, with diameters between 1 μm and 20 μm, range between 0.1 mm to 2 mm. It is possible to derive solutions for a time dependent sub-threshold stimulus, but the complexity is such that it is preferable to use a simulation programme to plot the resulting values of membrane voltage and other variables. Because a sub-threshold stimulus decays over a relatively short distance it is not capable of longer-distance stimulus transmission.
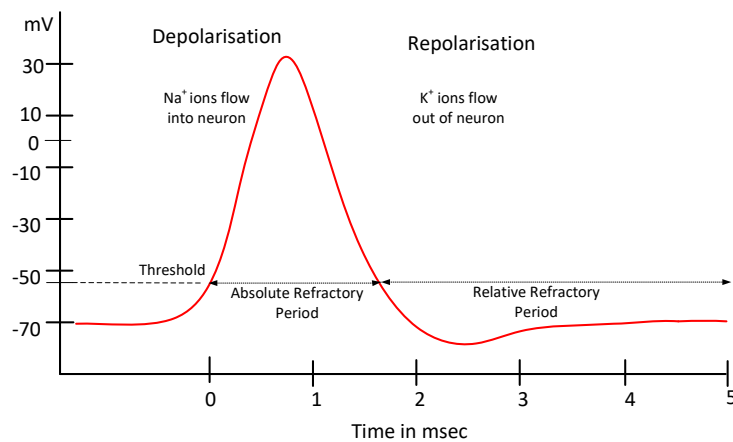
Fig. 2.2 Neural action potential sequence.

If a stimulus raises the resting potential above -55 mV (e.g., by applying a pulse of magnitude 15 mV or greater) then the neuron activates. Ion channels in the neural membrane open and positively charged sodium ions flow across the membrane into the neuron (depolarisation). The potential rapidly increases to about 40 mV (a total increase of 110 mV from rest). At this point the sodium ion channels close, potassium ion channels open and there's a flow of positive potassium ions out of the neuron (repolarisation), generating an AP.

The AP then propagates down the neuron's axon and either transfers to another neuron (via neurotransmitters) or a muscle cell, for example. The first neuron then returns to the rest state. The whole cycle takes between 5 ms and 10 ms and this is defined as the *refractory period* (Malmivuo and Plonsey, 1995). This can be divided into two periods. The first period, the *absolute refractory period*, is the time interval from the initiation of the action potential to just after the peak and it lasts between 1 ms and 2 ms. A stimulus applied during this interval will not result in another action potential no matter how intense the stimulus is. The second period, the *relative refractory period*, is the interval between the end of the absolute refractory period and the return to the rest state and lasts between 3 ms and 4 ms. A stimulus applied during this interval may result in an action potential if the intensity is greater than that needed to provoke an action potential from the rest state (suprathreshold). The action potential sequence of depolarisation and repolarisation is shown in Fig. 2.2. The refractory period also ensures that an AP can only travel in one direction as the neuron will be de-activated in the opposite direction. Larger diameter axons have an insulating sheath of *myelin* that has regular gaps at intervals of 2 mm, called nodes of Ranvier (typical width of 2 μm) where the

17

AP is regenerated. The speed of propagation of an AP is greater in myelinated neurons and will also depend on factors such as axon diameter (§4.2.1). An AP is sometimes referred to as a neural spike, especially in the recording of brain activity.

2.2.6 Nanoscale Networks and Molecular Communications

The future development of miniature implantable devices at the micro and nanoscale will create particular challenges in device communications both within the body and to an external transceiver. Communication using radio frequency (RF) systems is challenging as the small scale limits antenna size. This in turn will dictate shorter wavelengths (higher frequencies) that are heavily absorbed by human tissue. Biological molecular structures such as proteins, DNA, organelles and cell components all exist at the nanoscale and use forms of chemical signalling, or molecular communications (MC), that are now the subject of research and modelling (Farsad et al., 2016). In MC, small information particles convey information from a transmission location to a receiver point. Information particles are typically a few nanometres to a few micrometres in size and could be either biological compounds, such as neurotransmitters, or synthetic compounds, such as gold nano-particles. The communications channel is a liquid or gaseous environment where the information particles can propagate. The transmitter generates or stores the information particles and releases them in a controlled and modulated manner. Some form of processing unit is needed to encode the particles and control the operation of the transmitter. The processing unit could operate chemically or electrically and would require a power source. At the receiving end there is a receptor or detector to measure some property of the received information particles. This property could be the presence or absence of the information particles, the concentration of particles, the time of arrival, or any other measurable parameter (Farsad et al., 2016). If the particles represent coded information then there may also be a need for a central processing unit to decode the received signal. The receiver will also require a power source. Decoding modulated chemical signals may be complicated by the presence of channel noise and inter-symbol interference (ISI) between the pulses of emitted particles.

A projected application for nanoscale devices in medicine is an artificial immune system (Felicetti et al., 2016). Miniature artificial devices could be injected into the body with each device having a specialized role in the location and destruction of pathogens. This mirrors the operation of the immune system, but to function collectively the devices need to communicate and collaborate with each other. Other forms of communicating nanorobots are also proposed for the diagnosis and treatment

18

of complex medical conditions through, for example, targeted drug delivery or nanosurgery.

There is a broad distinction made between short-range microscale (nanometres to millimetres) and long-range macroscale (millimetres to metres) MC (Parcerisa-Giné and Akyildiz, 2009). For microscale MC, the particle propagation methods are :

- diffusion-based propagation, based on Brownian motion through a medium;

- flow-assisted propagation that could use, for example, the cardiovascular system;

- active transport using, for example, molecular motor proteins or cytoskeletal filaments;

- bacterial assisted propagation using self-propelling flagellated bacteria.

The two main forms of propagation at macroscale are diffusion and flow-based propagation. Diffusion can be a very slow process especially over longer distances and the speeds can be at the scale of cm/hour. Flow-based propagation provides higher speeds and can be realised by the following mechanisms:

- Advection, or transport with a bulk fluid flow such as an air current,

- Mechanical dispersion, caused by variations in flow pathways or variations in fluid speed in different regions,

- Convection, generated by differences in temperature within a fluid,

- Turbulent flows in a fluid.

The rate of transmission in all these cases depends on the rate of flow.

Neuro-spike communications is a hybrid model that includes both the transmission of APs along axons (as described in §2.2.5) and the follow-on molecular communication of neurotransmitters across synapses (Balevi and Akan, 2013). It can contain elements of both microscale and macroscale MC. The speed of MC is very low compared to RF communication. The communications channel can also contain background neural and chemical noise. Any data communications protocol will have to overcome these challenges if it is to provide a viable alternative to RF at the nanoscale.

2.3   Literature Review

This section is a literature review of developments in implant devices, powering and communications. The review also includes research into neural stimulation and the modelling of neural activity.

2.3.1 Medical Implant Devices

The evolution of medical devices from external (wearable) to internal (implant) is described in detail by Andreu-Perez et al. (2015), and the authors analyse the challenges in data management and machine learning if closed-loop systems are to emerge. Existing neural stimulus and recording devices have embedded electrodes that are wired to an embedded or external power and control unit to deliver measured amounts of voltage and current. The materials used in fabricating electrodes, their operating parameters and electrochemical properties are surveyed by Cogan (2008). The wrap-around cuff electrode is one of the most popular, (Naples et al., 1988), (Korivi and Ajmera, 2011). The tripolar nerve cuff electrode design is considered the optimum for low-noise measurement of peripheral nerve activity. Design principles for recording with tripolar cuff electrodes are given by Loeb and Peck (1996) The electrical potentials are differentially measured between a single middle contact and two electrically-shorted symmetrical side contacts. This eliminates any voltage drop (i.e., external noise) that is generated along the inside of the nerve cuff. Small flexible strip electrodes, as described by Lee et al. (2016), are proposed for recording from small nerves where a cuff might cause damage. Newer flexible and biocompatible polymer cuff electrode materials, such as paralyne, are recommended by Yu et al. (2014) while Apollo et al. (2015) describe the fabrication of a graphene oxide microfibre electrode. A survey of future developments in interfacing with the nervous system is provided by Rivnay et al. (2017) including optical, magnetic and ultrasound stimulation and recording.

Neural stimulation and recording is of particular importance for functions such as deep brain stimulation (DBS), spinal cord stimulation, cardiac pacemakers, cochlear implants and prosthesis activation. Cardiac pacemakers are one of the most widespread implants currently in use but the leads that run from the embedded unit in the chest to the electrodes in the heart are often a source of inflammation and infection. Developments in leadless technology, pacemaker miniaturisation, improved synchronisation and non-battery powering are described by Seriwala et al. (2016) and Madhavan et al. (2017). These improved devices would simplify surgical placement and minimise scarring as well as reducing the possibility of infection.

The use of DBS for the treatment of Parkinson's Disease is also being more widely used (Martinez-Ramirez et al., 2015). Like the pacemaker, the stimulus unit is placed below the clavicle and the electrodes implanted in the brain. A typical DBS system is described in detail by Oluigbo et al. (2012), who state that the exact mechanism by which DBS works in unknown. There has been some study in defining safe stimulus

levels for brain tissue based on stimulus waveforms, charge densities, electrode size and shape (Shannon, 1992) and safe thresholds have been set for equipment manufacturers. These are under constant review any may have to be modified for emerging types of microelectrode (Cogan et al., 2016). The DBS parameters of pulse width, frequency, amplitude and waveform are analysed by Kuncel and Grill (2004) while the technical features of some products are described by Amon and Alesch (2017). A more advanced closed-loop smart DBS system is proposed by Khan and Deng (2017). The system has a wearable smart controller that can modify the stimulus parameters in response to neural waveform information received from an implanted detection system.

A review of the applications of vagus nerve stimulation (VNS) is provided by Groves and Brown (2005) who note that the exact mechanism of action is still not fully understood. There is ongoing research into the use of VNS for the treatment of epileptic seizures, depression (Browning et al., 2017), heart failure (Howland, 2014), arthritis (Koopman et al., 2016) and Crohn's disease. A closed-loop VNS system is modeled by Ward et al. (2015) using autonomous neural control (ANC), a form of artificial intelligence that adjusts stimulus parameters in real time to mediate both the target therapeutic effects and the side effects. Computational modelling of VNS was performed by Helmers et al. (2012) to study the effect of current and pulse width on fibre activation. The modelled results showed good correlation with real medical results.

Prosthesis development is centred on a brain-machine interface (BMI) that can record neural activity, extract the intended action from that activity, generate the desired action with a prosthetic effector and provide feedback, either through natural sensation or generated and applied by the prosthetic device. The overall system requirements are described by Schwartz et al. (2006) and some of the processing challenges , such as raw data compression, are described by Zhang et al. (2012). The development of a BMI for the hippocampus to assist in memory recall is a topic of research by Berger et al. (2012) and Hampson et al. (2018). A system for detecting brain activity and then transmitting locomotion signals wirelessly to the lower spinal cord is described by Capogrosso et al. (2016). The objective is to bypass a damaged section of the spinal cord while retaining lower limb functionality. Future developments in BMI, called *enplants*, are proposed by Dambrot (2017) based on synthetic genomics, bionanotechnology and quantum communications.

Drug delivery systems at present usually consist of an external pump and reservoir with a subcutaneous needle for injecting the drug at timed intervals. Insulin pump technologies and glucose sensors are described by McAdams and Rizvi. (2016) who also predict the development of a closed-loop bionic pancreas. Other delivery

technologies are still at the experimental stage. Targeted drug-delivery aims to improve the delivery of smaller doses of a specific drug much closer to the area requiring treatment. Drug-delivery to the brain is difficult as the protective blood brain barrier (BBB) presents a challenge for the absorption of drugs (Dong, 2018) to treat, for example, cancer tumours. A drug-delivery system for treating epilepsy is described by Salam et al. (2012) with embedded electrodes to detect seizures and a micromechanical pump to deliver the drug from a refillable reservoir located under the scalp. Electrophoretic drug-delivery, as described by Proctor et al. (2018), applies a voltage difference (typically 1 V) to pump ions from a reservoir across an ion exchange membrane. The system uses a microfluidic ion pump (μFIP) of the type described by Uguz et al. (2017). An alternative method, electrothermal membrane activation, was first proposed by Santini Jr et al. (1999) for multiple drug-delivery and the first clinical trial of a working prototype is described by Farra et al. (2012). A metallic membrane covering each drug reservoir is heated by an applied electrical current, the membrane ruptures and the drug reservoir then releases its contents. This release model is used by Huang et al. (2012) and also by Maloney et al. (2005) in their proposed drug-delivery devices.

2.3.2 Powering and Energy Harvesting

Implanted devices ideally operate at the minimum power level possible in order to conserve, for example, battery life or to minimise heat dissipation. Guiding principles for low-power devices are outlined by (Sarpeshkar, 2012) and these include analogue pre-processing, efficient encoding, parallel architectures and minimising the amount of information that must be processed. Power for implanted devices is usually delivered by a long-life battery of the types described by Bock et al. (2012). The majority of batteries have a lithium metal anode while the cathode could be iodine, manganese oxide or silver-vanadium oxide depending on the power-output requirements. A high power lithium ion microbattery architecture is proposed by Pikul et al. (2013) using electrodes deposited on a nickel scaffold to improve power density. A single-use battery would have to be removed once the charge had dropped to the minimum recommended level. A rechargeable battery would be more durable provided it could be recharged, for example, through energy harvesting. An overview of newer battery technologies and potential harvesting methods is given by Kim et al. (2015). Research into technologically based energy-harvesting systems centres at present on wireless EM systems. Wireless powering can be delivered using near-field EM inductive resonant coupling at frequencies up to 20 MHz as described by Kim et al.

(2017) but this is efficient only for short distances. The use of lower EM frequencies also results in the need for larger antennas that will increase the size of the implanted device. Power may be delivered over a greater range using higher frequency mid-field (900 MHz) (Ho et al., 2013) or far-field (2.5 GHz) EM powering (Xia and Aissa, 2015) although the efficiency is reduced relative to near-field powering. The use of EM energy harvesting is subject to technical constraints to meet recommended safety levels (Rabaey et al., 2011) and prevent tissue damage through excessive heating of the embedded device (Kodera et al., 2018), (Lazzi, 2005). It would also require the wearing of an external powering source if true mobility was required.

A possible alternative to EM harvesting is the use of piezoelectric harvesters that can convert mechanical deformations into electrical energy. The use of ultrasound, or acoustic energy transfer (AET), as a power source is surveyed by (Roes et al., 2013) who notes that the main losses derive from transducer, medium attenuation and spreading. The powering of sensors embedded in tissue using resonant PZT crystals was investigated experimentally by Ozeri and Shmilovitz (2010), using an ultrasound frequency of 673 kHz. The authors describe the choice of ultrasound frequency as trade-off between crystal thickness and focal distance. A similar system with a hybrid data link is described by Charthad et al. (2015) with ultrasound used for both powering and a data downlink while RF is used for an uplink. Another two-tier method of inductive powering and ultrasound powering was modelled by Sanni et al. (2012). The inductive power was delivered to a subcutaneous transponder that then transmitted ultrasound energy to a deeply embedded implant. Ultrasound crystal powering has also been proposed for neural stimulation (Charthad et al., 2018) and drug delivery (Charthad et al., 2016). The use of micro-scale resonant crystals ("neural dust") for neural recording in the brain using ultrasound powering and backscatter was proposed by Seo et al. (2015a). The challenges of developing and operating such devices are outlined by Neely et al. (2018). Ultrasonic beamforming is described in more detail by Bertrand et al. (2014) and Seo et al. (2015b). The recording and stimulating principle has been demonstrated for peripheral nerves (Seo et al., 2016), (Johnson et al., 2018) as these were easier to access than the interior of the brain and a conversion efficiency of 82% was reported. A cuff electrode powered by a PZT crystal, operating at 1 MHz was also demonstrated by Larson and Towe (2011). Simple half-wave rectification of the output AC voltage with a single diode provided a stimulus pulse to the sciatic nerve of a rat. The output power and successful operation depend critically on the positioning and alignment of the crystal, which could easily be changed in a live body. An alternative method of harvesting using a piezoelectric diaphragm array is described by Shi et al. (2016). They array has two resonant modes giving a wider bandwidth and a

wider range of operating ultrasound frequencies. Energy harvesting using zinc oxide (ZnO) nanowires was proposed by Wang and Song (2006) for delivering a periodic direct current (DC) voltage and current. An ultrasound nanogenerator using ZnO nanowires was demonstrated by Wang et al. (2007b), who immersed the device in water and applied ultrasound excitation at 41 kHz. The output current and voltage values were recorded as noisy square waves, but the input intensity of the ultrasound was not recorded, making it difficult to assess the efficiency. The same group carried out ultrasound energy-harvesting tests on fabricated nanowire devices in biofluids (Wang et al., 2007a) that included coupling three devices, first in parallel and then in series to demonstrate boosting current and voltage. Nanowires are not as efficient as resonant piezoelectric crystals for energy conversion (Yang et al., 2017) but can operate at lower ultrasound frequencies. Improvements to ZnO nanowire performance by surface modification is described by Jalali et al. (2013). Their improved fabricated device showed an almost five times greater power density than the original. Harvesting ultrasound power for medical devices remains a topic of research and there are no commercially available products as yet.

A review of different glucose fuel cell technologies suitable for implanted devices is provided by Cosnier et al. (2014) who note the difficulty in comparing features over different sizes and performance measures. An abiotically catalysed glucose fuel cell suitable for implanted devices is described in detail by Kerzenmacher et al. (2008). Glucose energy harvesting from cerebrospinal fluid circulating around the brain is described by Rapoport et al. (2012) and the required flux of glucose is calculated for different efficiencies and power levels. Improvements in glucose harvesting performance have been demonstrated by Kwon et al. (2018) who developed a hybrid biofuel cell that uses a metallic cotton fibre cathode and has a power density of 37 μW per mm^2. A dual source glucose and thermoelectric harvesting system is proposed by Katic et al. (2018) to improve reliability. The system has a maximum output power of 66 μW. Much more work needs to be done before higher levels of power into the milliwatt range can be reliably generated from glucose harvesting.

2.3.3   Device Communications

Wireless communications to and from embedded medical devices use a variety of technologies and frequencies. An overview of media properties and standards is provided by Ritter et al. (2014), while the capacity requirements for telemetry links is discussed by Bihr et al. (2014). Short-range, inductively coupled data transfer is currently used in some implanted systems (Kim et al., 2017), (Jegadeesan et al., 2015),

(Xu et al., 2014) while also providing inductive powering. Higher frequency, higher capacity wireless communications technologies in the MICS and ISM bands are described by Teshome et al. (2019) who also analyse the future challenges of communicating with microscale and nanoscale implants. Smaller devices at these scales will require even higher frequencies in the terahertz, near-infrared or optical bands. The challenges of communications in the terahertz band through human tissue are described by Piro et al. (2015) who note the high level of absorption and the resulting short range. The use of optical signals in the body is modelled by Johari and Jornet (2018), who consider transmission through blood cells in plasma. Optical transmission is also modelled by Wirdatmadja et al. (2019) who look at light propagation in brain tissue. Ultrasound is proposed by Santagati et al. (2013) as an alternative in-body communications with details on a suitable medium access control (MAC) described in (Santagati et al., 2015) and experimental results reported in (Santagati and Melodia, 2017). Research into other proposed non-wireless or optical communications techniques is covered in §2.3.5.

2.3.4   Neural Stimulation

The original empirical model for describing AP generation was devised by Hodgkin and Huxley (1952) based on the axon of the giant squid and, with some modifications, is still in use today. The model has four fourth-order non-linear differential equations that can only be solved by numerical methods. A simplified version, the FitzHugh-Nagumo model, is widely used in computer simulation (Sherwood, 2013). The basic principles of neural stimulation are detailed by Brocker and Grill (2013). The parameters of stimulus pulse duration were modeled by Grill and Mortimer (1996) while the effects of diameter were modeled by Altman and Plonsey (1990). The potential at a point in a conducting extracellular medium from a travelling current source can be calculated from volume conduction (Rutkove, 2007) and this forms the basis for simulating APs. An empirical intracellular AP model for human muscle was devised by Nandedkar and Stalberg (1983), based on an earlier version by Rosenfalck (1969). The intracellular model provides the basis for calculating the extracellular AP (Rattay, 1989), (Rattay, 1999). Extracellular AP propagation monopole models were developed by Plonsey (1974) and Nandedkar and Stalberg (1983) and a dipole model was developed by Dimitrova et al. (1999). These were analysed by Falces et al. (2005) who noted that the dipole model gave better results at neural boundaries and was more consistent with experimental data. Schoonhoven et al. (1986b) used a volume conduction and convolution model to compute extracellular APs and then combined

these mathematically into a CAP. Other CAP models were also developed by Wijesinghe et al. (1991) and Stegeman and Weerd (1982) based on similar principles. A review of models is presented by Schoonhoven et al. (1986a). These models were mainly used to explore the underlying structure of a nerve fascicle based on the relative intensity of different peaks in the CAP (Schoonhoven et al., 1988), (Stegeman et al., 1988). Mapping the topography of fascicles through the median, radial and ulnar nerves was originally undertaken by Sunderland (1945). Further research was done by Jabaley et al. (1980),Stewart (2003), Delgado-Martínez et al. (2016) and Planitzer et al. (2014) to determine improved fascicle maps especially for prosthesis research. These studies showed how the position of a fascicle changed with branching and that key fascicles contained neurons of one type only (either motor or sensory).

A nerve can also be seen as a communications path transporting information via neurons from the body to the brain and vice versa. A whole-body communications system using touch stimuli on a finger as transmitters and brain scan information as a receiver is described by Hanisch and Pierobon (2017). The maximum modelled bitrate is 40 bit/s though the detection system has a lot of background noise from other brain functions. Other research is directed specifically at single neurons, modelling the generation and propagation of individual action potentials (spikes) and examining how such spikes can be modulated to convey information.

2.3.5   Neural and Molecular communications

The manipulation and control of devices at the microscale was originally proposed by Richard Feynman in 1959 (Feynman, 1992), who particularly mentioned biological structures as miniature computation and storage systems. The challenge of devising nanomachines and the communications systems between them is described by Akyildiz et al. (2008) and a survey of modelling research is provided by Farsad et al. (2016). The potential uses of nanodevices and MC in medicine for disease detection, imaging, drug-delivery and nanosurgery are surveyed by Felicetti et al. (2016). An overview of molecular communications methods for clusters of embedded nanodevices is provided by Atakan et al. (2012) who propose a body-area nanonetwork. These clusters could communicate with external devices through gateways as described by Akyildiz et al. (2015). Options for short-range molecular communications include calcium signalling (Clapham, 2007), used extensively in the body and proposed by Taynnan Barros et al. (2015) for use by nanomachines at the cellular level. Molecular motors based on kinesin or dynein motor proteins are modelled by Chahibi et al. (2016) for the transport of molecules against concentration gradients or flows. The capacity of a microfluidic

channel for molecular communications is modelled by Bicen and Akyildiz (2015) in order to quantify the interference experienced. Further modelling of the microfluidic channel was done on end-to-end noise and memory analysis (Bicen and Akyildiz, 2014) and the summed broadcast capacity (Bicen et al., 2018). Using nanonetworks and molecular communications for targeted drug-delivery is the subject of an extensive survey by Chude-Okonkwo et al. (2017). The cardiovascular system has been modelled as a molecular communications channel for the dispersion of drug nanoparticles (Chahibi and Akyildiz, 2014), or engineered antibodies (Chahibi et al., 2015). Longer range molecular communications options, such as pheromones or pollen, are described in detail by Parcerisa-Giné and Akyildiz (2009). Channel models for single-spike intra-neuron and inter-neuron communications, based mainly on experimental knowledge of hippocampal neurons, have been developed by Malak and Akan (2013), Balevi and Akan (2013), Ramezani and Akan (2018), Veletić et al. (2016) and Cacciapuoti et al. (2016). The modelling of a multiple input, single output (*MISO*) neural channel is examined in more detail by Ramezani et al. (2018) who also consider the effects of a neural degenerative disease on the number of available neurotransmitters. The interfacing of nanomachines with neurons is modelled by Galluccio et al. (2012) and by Mesiti and Balasingham (2013) to facilitate functions such as neural stimulation. A neuron channel model using a sub-threshold (non-spiking) stimulus was proposed by Khodaei and Pierobon (2016a) (Khodaei and Pierobon, 2016b), though sub-threshold impulses have a very short range along an axon (Cartee and Plonsey, 1992), (Malmivuo and Plonsey, 1995) and could only be used on the micrometere to millimetre scale.

Data communications through the single median giant axon of the earthworm was modelled by Abbasi et al. (2018) who calculated a data throughput based on the modulation technique of frequency shift keying (FSK). Other potential modulation methods that could be applied to stimulated neural pulses include on-off keying (OOK) and digital pulse-interval modulation (DPIM). DPIM was proposed as a coding system for optical wireless (non-fibre based) communications by Ghassemlooy et al. (1998) who compare the throughput, efficiency and error performance with both OOK and PPM. Versions of DPIM for super-slow bacterial molecular communications have been proposed by Krishnaswamy et al. (2013) (time elapse communication (TEC)) and Barros et al. (2014) (*Dynamic Time-Slot Configuration with Silent Communication*). MacKay and McCulloch (1952) explored the throughput that could be achieved in a single neuron using OOK and DPIM.

Modelling a neural communications channel capacity requires not only input signals but also some input noise. Neural background noise can be modelled as additive white

Gaussian noise (AWGN) with root mean square (*rms*) values in the range 5 μV to 10 μV (Guillory and Normann, 1999; Harrison, 2003). A noisy and unidirectional neural channel can use FEC to improve performance. One form of error correction, *block codes*, add additional parity bits to a byte and are described in (MacWilliams and Sloane, 1977). Block codes can be classed as linear or cyclical and include Hamming linear codes (Wicker, 1995), Golay binary code, Bose-Chaudhuri-Hocquenghem (BCH) cyclic codes (Bose and Ray-Chaudhuri, 1960), Reed-Solomon (RS) cyclic codes (Reed and Solomon, 1960) and Turbo Product codes (Berrou et al., 1993). These types of code are used not only in noisy communications channel but also used to correct errors in digital storage systems. The use of block codes in molecular communications is proposed by Leeson and Higgins (2012) and Lu et al. (2017) for nanomachine communication in molecular networks.

2.4   Summary

Existing wireless implanted devices are usually powered with non-rechargeable batteries that must be periodically changed. This requires repeated surgical intervention with increased risk of infection and scarring. Communication with implants is through short-range wireless and the power consumption of the transmission systems is in the milliwatt range. There are systems under development for EM and ultrasound energy harvesting, to avoid the battery bottleneck, but none are commercially available as yet. Research into using the nervous system for artificial communications is centred at present on analysing single neurons for nanomachine communications rather than groups of neurons that could produce a larger signal amplitude. It is these research gaps in ultrasound power harvesting and neural communications that we wish to address in the following Chapters.

Chapter 3

Ultrasound Energy Harvesting

3.1 Introduction

Medical diagnostic ultrasound scans use frequencies between 1MHz and 15 MHz to build up an image from signals reflected from different tissue layers. The level of penetration of the ultrasound into human tissue depends on the frequency of the ultrasound and the absorption coefficient of the tissue. Higher frequencies experience higher absorption but are sometimes used for better image resolution. The amount of reflection that a beam experiences depends on the relative density of each layer of tissue with the denser tissues showing greater reflectivity. Transmitted ultrasound that has penetrated to a particular depth may be harvested, in turn, to generate electrical pulses from embedded piezoelectric devices. In this chapter we model the characteristics of ultrasound in human tissue and what power levels might be generated by an embedded ultrasound-harvesting piezoelectric device.

3.2 Ultrasound Generation

Ultrasound transducers can be designed to radiate sound in many different types of pattern, from omnidirectional to very narrow beams. For a transducer with a circular radiating surface, vibrating in phase, the beam can be shaped in order to narrow the area of transmission but some spreading will occur. It is possible to produce a beam with a specific focal length by adding an acoustic lens to the transducer. Ideally a target energy-harvesting device would be placed at the focal distance to maximise energy absorption. If the target energy-harvesting device is small (less than 1 cm^2) then the transducer radius and area can also be small in order to reduce the transmitted power while maintaining maximum intensity.
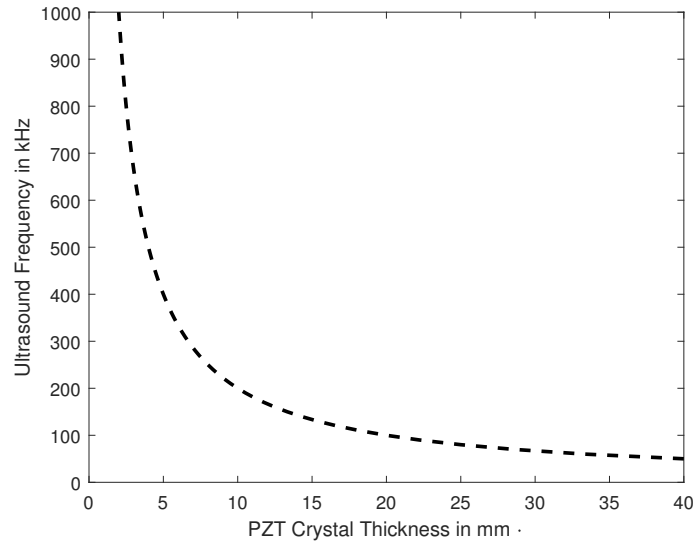
Fig. 3.1 Plot of ultrasound frequency and PZT transducer thickness.

The thickness of a resonant crystal is half of the wavelength of ultrasound in the transducer and can be calculated from the ultrasound frequency and the speed of sound in a resonant crystal as follows:

$$d = \frac{\lambda_t}{2} = \frac{v_t}{2f},$$

(3.1)

where d is the thickness, λ_t is the wavelength, v_t is the speed of sound in the transducer and f is the ultrasound frequency. The speed of sound in a typical PZT resonant crystal is 4000 m/s. A plot of the variation of transducer thickness (d) with frequency (f), based on (3.1), is shown in Fig. 3.1. The plot shows that 1 MHz ultrasound frequency would have a wavelength of 4 mm and require a transducer thickness of 2 mm. Producing a lower frequency, for example 50 kHz, would require crystal thickness of 40 mm. Ultrasound is a non-ionising radiation but there are safety guidelines on using it with human tissue to minimise heating and bubble formation (cavitation). The ultrasound intensity used in our calculations is based on a maximum value of 720 mW/cm^2, which is in line with medical recommendations (Hendee and Ritenour, 2003b).

3.2.1 Absorption and Reflection in Human Tissue

Externally applied ultrasound will penetrate initially through several layers of human skin tissue. An ultrasonic beam of frequency f MHz with an initial intensity of U_o
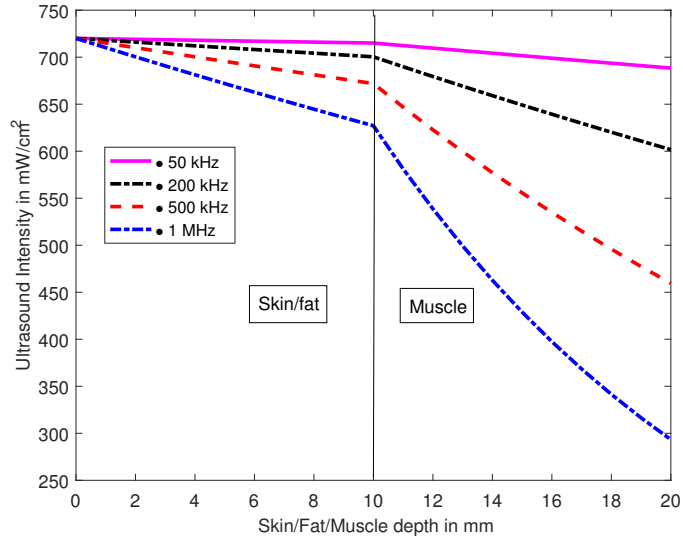
Fig. 3.2 Plot of ultrasound intensity and tissue depth.

Table 3.1 Human tissue acoustic absorption and impedance values.

Tissue	Absorption (db/cm/MHz)	Impedance (MRayl)
Blood	0.18	1.59
Fat	0.6	1.38
Muscle	3.3	1.7
Bone	20	6

penetrating to a depth of *d* cm will have a resultant intensity of U_d:

$$U_d = U_o 10^{-(\alpha f d/10)} \tag{3.2}$$

where the absorption coefficient, α, expresses the power loss in dB/cm/MHz. Absorption coefficient values for some human tissues are shown in Table 3.1 (Hendee and Ritenour, 2003b). A plot of ultrasound intensity (U_d) with respect to tissue depth (*d*), based on (3.2) and absorption coefficient values for fat and muscle, is shown in Figure 3.2. The ultrasound attenuation is calculated through 10mm skin/fat and then 10mm muscle for four different ultrasound frequencies (50 kHz, 200 kHz, 500 kHz, 1 MHz). The plot shows how higher ultrasound frequencies are more strongly absorbed compared to lower frequencies, particularly in the denser muscle tissue.

Acoustic reflections at tissue interfaces (e.g., between fat and muscle) are caused by differences in *acoustic impedance* (the density of the tissue multiplied by the speed of sound); the unit of acoustic impedance is the Rayl (kg.s^{-1}.m^{-2}). If two materials have

31

acoustic impedances Z_1 and Z_2 then the ratio between incident intensity I_o and reflected intensity I_r is represented as:

$$\frac{I_r}{I_o} = \frac{(Z_2 - Z_1)^2}{(Z_2 + Z_1)^2}. \tag{3.3}$$

Acoustic impedance values for some human tissues are also shown in Table 3.1. The reflection at an air/human tissue interface would result in up to 99% of the ultrasound being reflected because of a large difference in the acoustic impedance (429 Rayl for air, 1.38 MRayl for skin/fat). Consequently there should be no air gap between an ultrasound transducer and human tissue.

3.3 Energy Harvesting

An energy-harvesting nanodevice must convert incident ultrasound into mechanical vibrations and then into piezoelectric energy. There are two main methods for harvesting ultrasound: resonant *piezoelectric crystals* or vibrating *piezoelectric nanowires*. The size of a resonant crystal depends on the frequency of the ultrasound: the higher the frequency, the thinner the crystal. Thin crystals of 2 mm or less would imply a resonant frequency in the 1 MHz or greater range. Such a frequency of ultrasound would be more strongly absorbed by human tissue (see §3.2.1) so miniature resonant crystal harvesters could only be deployed at very shallow skin depths (e.g., 2 mm). Therefore, for deeper penetration using lower ultrasound frequencies, we consider piezoelectric ZnO nanowires that can vibrate in response to a range of lower ultrasound frequencies and produce variable amounts of current and voltage.

3.3.1 Piezoelectric ZnO Nanowires

We use an analytical perturbation model for bending a *ZnO* nanowire developed by Gao and Wang (2007). The nanowire is modelled as a thin cylindrical rod with a specific modulus of elasticity (Young's modulus).
Bending a nanowire requires the application of a force that is countered by the elasticity of the nanowire. If a constant force F is applied until a bending before discharge of y_m (as depicted in Fig. 3.3) is achieved, then the balance of forces is as follows:

$$F = \frac{3YIy_m}{L^3} \tag{3.4}$$

Table 3.2 Force, displacement, work and voltage for bending a nanowire.

Force (nN)	Displacement (nm)	Work (fJ)	Voltage (V)
60	109	3.274	± 0.212
80	146	5.821	± 0.284
90	164	7.36	± 0.319
100	182	9.09	± 0.354

where Y is the nanowire's Young's modulus, I is the area moment of inertia and L is the nanowire length. The bending is directly proportional to the applied force. The energy (work) ΔE required to bend the nanowire by an amount y_m is:

$$\Delta E = \frac{3YIy_m^2}{2L^3}. \tag{3.5}$$

The work is proportional to the square of the displacement. The voltage V is approximately linear over the range of applied forces, as analysed by Hinchet et al. (2012), and can be expressed as:

$$V = Gy_m \tag{3.6}$$

where the parameter G has units of volts/nanometre and is a constant for specific values of diameter and length. Values for force, displacement, work and voltage (from (3.4), (3.5), (3.6)) for bending a nanowire that is 50 nm in diameter, 600 nm long and has a Young's Modulus of 129 GPa (Gao and Wang, 2007) are shown in Table 3.2. The value of G is 1.9 x 10^{-3} V/nm. The work required for bending is of the order of femtojoules and the magnitude of bending is sufficient to deliver a piezoelectric energy output. The use of ZnO nanowires for energy harvesting was proposed by Wang and Song (2006) for delivering a periodic DC voltage and current. The nanowires in this type of DC nanodevice are fixed at one end to a substrate while the other end is free and can bend to touch a specially engineered corrugated (zigzag) electrode. External vibrations push the substrate and harvesting electrode together and hence bend the nanowires. The bent nanowire then has a stretched side with a positive charge and a compressed side with a negative charge. The negative charge is released when the compressed surface of the bent nanowire touches the electrode. Systematically bending the nanowires produces a unidirectional current and negative voltage that's collected by the electrode, as shown in Fig. 3.3. The zigzag electrode of the Wang device is made from platinum-coated silicon with parallel etched trenches. The substrate is made from a flexible polymer (preferably biosafe) coated with a thin film of gold. Aligned nanowire
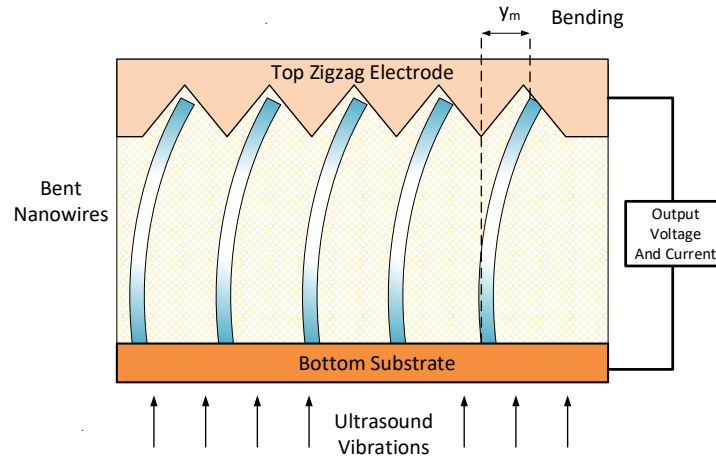
Fig. 3.3 Energy harvesting from bent nanowires using a corrugated top electrode and a conducting substrate.

arrays can be grown on such a flexible substrate to match up with the trenches on the electrode. Spacing between the substrate and the electrode is provided by polymer strips that can be sealed if the device is to be immersed in liquid.

The maximum potential (voltage) at the nanowire's surface is directly proportional to the bending and inversely proportional to the length-to-diameter aspect ratio. The bending creates a piezoelectric negative potential between the upper zigzag electrode and the lower substrate.

The overall power harvesting capability depends on: (i) the amount of bending the nanowires are subjected to; (ii) the bending events per second (frequency); and (iii) the nanowires per unit area (density). Ultrasound is one source of external vibration that can be used for bending the nanowires. The ultrasound vibrations effectively push the electrode and substrate together at the frequency of the ultrasound. This dynamic distortion of the device causes the nanowires to bend but they do not resonate at the ultrasound frequency. The energy per cycle of the ultrasound will determine the amount of bending while the ultrasound frequency will determine the quantity of bends per second. In order to demonstrate vibrational activation, a 2 mm^2 nanogenerator using ZnO nanowires and powered by ultrasounds was developed by Wang et al. (2007b). The device was immersed in water and subjected to ultrasound excitation at 41 kHz. The output current and voltage values were recorded as noisy square waves but the input intensity of the ultrasound was not recorded, making it difficult to assess the efficiency. The same group carried out similar ultrasound energy-harvesting tests in biofluids (Wang et al., 2007a) that included coupling three devices in parallel and then

in series to demonstrate boosting current and voltage. The square-wave output of these devices was as a result of (i) an inbuilt diode characteristic that delivered current in one direction only and (ii) capacitive effects in the contact between the nanowire and the electrode that helped spread the discharge of piezoelectricity through the electrode. The developers theorise that if all nanowires participated in current production, through better alignment and more uniform length, the result would be a much improved square wave DC output. Based on these considerations we model the output of a nanodevice as a DC square wave with no requirement for rectification and hence no additional power consumption or performance degradation.

We now compare the energy (work) levels for bending a nanowire (ΔE) as shown in Table 3.2 with the energy that can be delivered to a nanowire by ultrasound.

3.3.2 Cycle Energy

We need to compare the work levels for bending a nanowire in Table 3.2 with the energy that can be delivered to a nanowire by ultrasound. Initially, we model a single nanodevice that is perpendicular to the ultrasound vibrations (no tilt) and hence can intercept the maximum amount of ultrasound energy. The input intensity is fixed at 720 mW/cm^2, or 7.2 x 10^{-9}W/ μm^2, and the intensity at different depths is calculated using (3.2). At a fixed density of m nanowires per μm^2, the energy per nanowire per cycle, E_{nw}, at an ultrasound frequency of K cycles per second and intensity of U_d W/ μm^2 is calculated as follows:

$$E_{nw} = \frac{U_d}{mK}. \tag{3.7}$$

The total energy per cycle, E_{tot} intercepted by a device of area A_{nw} is as follows:

$$E_{tot} = \frac{A_{nw}U_d}{K} = A_{nw}mE_{nw}. \tag{3.8}$$

A plot of delivered energy per vibrational cycle (E_{tot}) at 50 kHz and 1 MHz, based on (3.8), for a range of nanogenerator areas and different skin/fat depths is shown in Figure 3.4. The nanowire density, m, is set at 20 per μm^2, the initial input intensity is fixed at 720 mW/cm^2, and the intensity at different depths, U_d is calculated using (3.2). At a fixed density, the energy per nanowire per cycle is independent of the area of the nanogenerator. At 50 kHz the energy level is from 7.1 fJ to 6.7 fJ at 1 cm and 10 cm depth, respectively. The energy per cycle per nanowire at 1 MHz is initially over 20 times lower than at 50 kHz (0.03 fJ) and decreases more rapidly with depth. A second plot of energy per cycle per nanowire, also based on (3.8), for a fixed device area (1000 μm^2), but with varying nanowire densities and skin/fat depths is shown in Fig. 3.5.
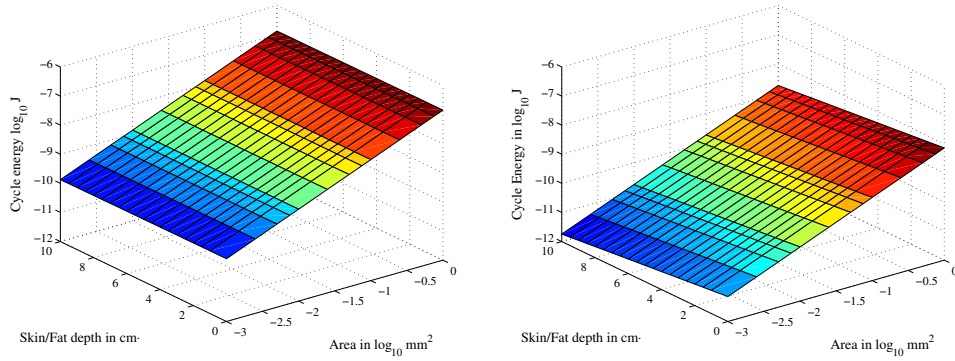
(a) 50 kHz ultrasound wave.   (b) 1 MHz ultrasound wave.

Fig. 3.4 Energy per cycle at 50 kHz (a) and 1 MHz (b) against skin/fat depth and varying nanogenerator area.

Higher nanowire densities will reduce the energy absorbed per nanowire for a fixed area. At 50 kHz the energy per nanowire per cycle drops below 6 fJ at these values (Fig. 3.5: Density 20, Skin/Fat depth 10 cm). At 1 MHz the energy per nanowire is lower than 1 fJ at all densities and depths. Both plots show that for a fixed input intensity, an ultrasound frequency of 50 kHz will deliver more than 6 fJ per cycle to a nanowire provided the density is equal to or lower than 20 nanowires per μm^2. This means that the magnitude of 50 kHz ultrasound cycle energies per nanowire are comparable to the bending energies shown in Table 3.2, but the 1 MHz cycle energies are too low to provide sufficient bending. We will therefore use an ultrasound frequency of 50 kHz as it:

- is above the upper level of human hearing (20 kHz),

- has better penetration with lower absorption through human tissue,

- provides more energy per cycle to bend nanowires than higher frequencies.

By using a lower ultrasound frequency with lower tissue absorption and short-duration (100 μs) infrequent pulses of ultrasound (See §4.2.1) we will minimise any possibility of tissue or nanodevice heating.

Maximum ultrasound power will be transferred to a nanodevice if the incident beam is perpendicular to the device substrate and hence strike the full nanodevice area. If a nanodevice is tilted at an angle to the ultrasound source, then the incident intensity will be reduced (Wang et al., 2009). A nanodevice tilted at an arbitrary angle can be modelled as a combination of a horizontal tilt and a vertical tilt. If U_d is the intensity of
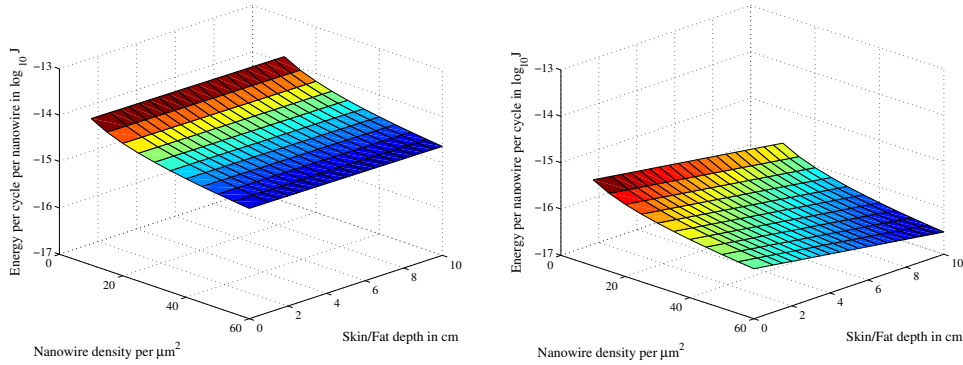
(a) 50 kHz ultrasound wave.   (b) 1MHz ultrasound wave.

Fig. 3.5 Energy per cycle at 50 kHz (a) and 1 MHz (b) against skin/fat depth and varying nanowire density.

a beam at a depth of d cm and a nanodevice is tilted at an angle θ in the horizontal plane and an angle ϕ in the vertical then the resulting intensity on the surface, U_r is:

$$U_r = U_d cos\theta cos\phi. \tag{3.9}$$

A plot of the ultrasound intensity (U_r), based on (3.9), at a skin/fat depth of 5 mm against varying horizontal and vertical tilt angles ($0°$ to $90°$) is shown in Fig. 3.6. The maximum intensity is 717 mW/cm^2 and drops steeply even for relatively small horizontal and vertical angles (e.g. $15°$). Consequently the level of tilt must be minimised if a threshold intensity needs to be maintained to activate a nanodevice.

3.3.3 Power Output Analysis

The total output energy of a nanodevice depends on (i) the energy of the incident ultrasonic wave; (ii) the harvesting area; (iii) piezoelectric efficiency of the nanowires; (iv) absorption or reflection of ultrasound within the nanodevice; and (v) the fraction of nanowires that contribute to the electrical output. The input energy levels range between 5.82 fJ (bending force of 80 nN) and 9.09 fJ (bending force of 100 nN) per nanowire as shown in Table 3.2. The DC *ZnO* nanodevice described in Wang and Song (2006) had a measured average output energy per nanowire of approximately 0.05 fJ, though this did not use ultrasound. A comparison with input energy levels suggests a conversion efficiency of between 0.8% and 0.55%. The output power P_o is computed from the nanodevice area A, the incident ultrasound intensity U_r and the conversion

37
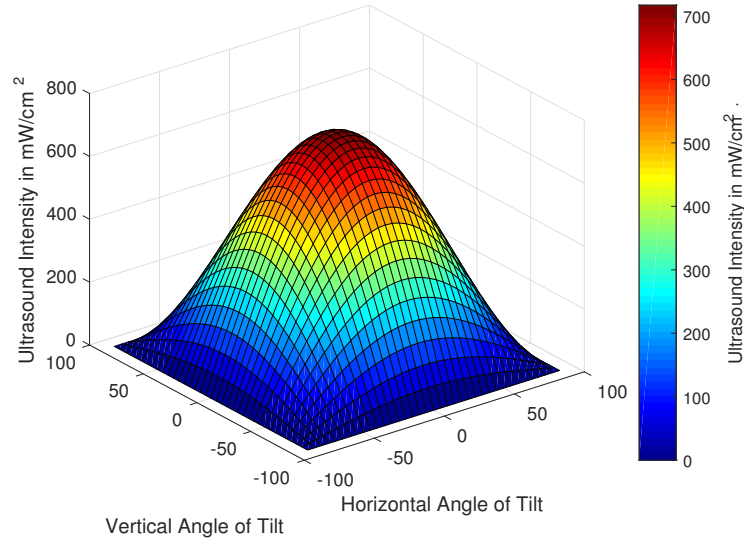
Fig. 3.6 Plot of ultrasound intensity and angles of tilt for a frequency of 50kHz and a skin/fat depth of 5 mm.

efficiency e, and is represented as follows:

$$P_o = AU_r e. \tag{3.10}$$

Thus, a $1000\mu m^2$ ultrasound harvesting nanodevice with 20 nanowires per μm^2 at a depth of 1 cm and incident ultrasound intensity of 710 mW/cm^2 (input work per nanowire of 7.1 fJ) could have a power output of 39 nW when a conversion factor of 0.55% is used. We will standardise our modelling on a $1000\mu m^2$ device for simplicity, giving us the flexibility to couple such devices together in order to increase output current or voltage levels and deliver a range of output power levels.

The voltage output of a nanodevice depends on the magnitude of bending that the nanowires experience. In order to drive any microelectronic circuitry, a voltage level of between -0.2 V and -0.3 V would be necessary. As indicated in Table 3.2 the theoretical output voltage of a nanowire bent by a force of 80 nN is -0.284 V, but experimental results for the same bending force provide a voltage level of -25 mV (Wang, 2008). This is less than 10% of the theoretical values, although the divergence is partly because of the difficulty in measuring at the nanoscale. By conservatively reducing the expected output voltage at 80 nN from -0.284 V to -0.025 V while retaining the same magnitude of bending, we can use (3.11) to calculate a new constant G' and derive new values of output voltage (V_o) for each value of force and bending as follows:

$$V_o = G' y_m. \tag{3.11}$$

38

This will give us the value of G' as 1.712 x 10^{-4} V/nm. We then use this scaling to calculate the output voltage and current of a 1000 μm^2 nanodevice when subjected to increasing intensity of incident ultrasound energy. From (3.5) we can derive the relationship between the amount of bending in the wire (y_m) and the energy needed for bending (ΔE) as follows:

$$y_m = \sqrt{\frac{\Delta E 2 L^3}{3YI}}. \tag{3.12}$$

We also know from (3.7), the amount of energy per nanowire that a specific intensity of ultrasound can deliver (E_{nw}). By substituting for ΔE and also using (3.11), we can derive the relationship between the output voltage (V_o) and incident ultrasound intensity (U_r) for a nanowire as follows:

$$\begin{aligned} V_o &= G' y_m \\ &= G'\sqrt{\frac{\Delta E 2 L^3}{3YI}} \\ &= G'\sqrt{\frac{2L^3}{3YImK}}\sqrt{U_r}. \end{aligned} \tag{3.13}$$

The nanowire size, the density of nanowires (m) and the ultrasound frequency (K) are all fixed so the only variables are the voltage level V_o and the incident ultrasound intensity U_r. The maximum current output of a nanodevice depends on the total charge generated from all the bent nanowires and how quickly the charge is released. In our model we calculate the output current I_o from the output power P_o and voltage V_o as follows:

$$I_o = \frac{P_o}{V_o} = \frac{AU_r e}{V_o}. \tag{3.14}$$

The resulting plots of nanodevice output voltage (V_o) and current (I_o) against ultrasound intensity (U_r), based on (3.13) and (3.14), are shown in Fig. 3.7. The plots are approximately linear except at lower levels of the ultrasound intensity.

3.4   Summary

Ultrasound can be safely transmitted into the human at recommended levels of intensity. The beam can provide sufficient energy for the operation of implanted, energy-harvesting piezoelectric nanodevices at shallow depths under the skin.
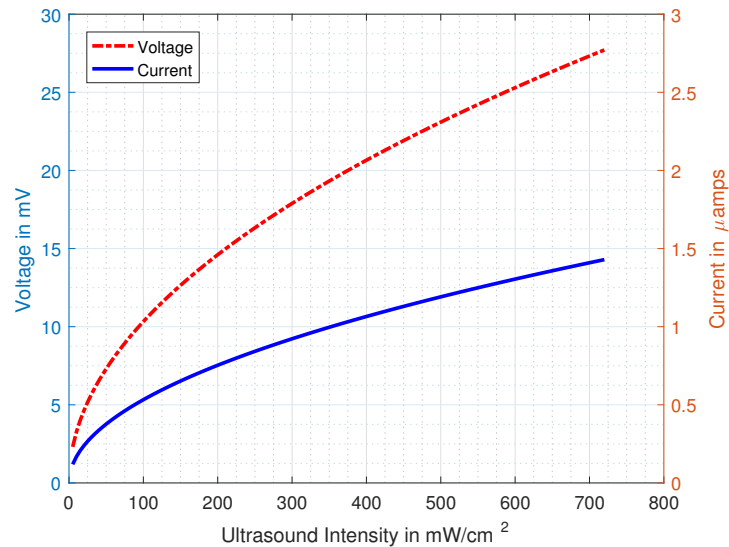
Fig. 3.7 Plot of ultrasound intensity against output voltage and output current for a $1000\mu\text{m}^2$ nanodevice at an ultrasound frequency of 50kHz.

Lower-frequency ultrasound has greater tissue penetration and delivers more energy per cycle to bend the nanowires. Other conditions that need to be considered are:

- The nanodevices should all be at the same depth.

- There should be no dense tissue or bone obstructing the path in order to minimise absorption and reflections.

- The nanowires should bend in response to the cyclic vibrations induced by the ultrasound enenrgy.

- The nanodevices should be inserted so as to minimise any tilt in order to collect the maximum ultrasound intensity.

- The material encapsulating the nanodevice and the device substrate should match the acoustic impedance of body tissue as closely as possible.

Having determined the output voltage and current levels for an ultrasound-harvesting embedded nanodevice, we now examine the current and voltage levels needed to stimulate nerves in the human body.

Chapter 4

Stimulated Neural Activation

4.1   Introduction

In this Chapter we model the use of piezoelectric nanowire devices (nanodevices) that can be safely implanted into patients for the longer-term stimulation of selected peripheral nerves. The nanodevice harvests its energy from ultrasound waves that are emitted by a portable external source. The use of wireless powering and biocompatible materials will provide greater longevity of components, though there are no projections for the ultimate longevity of such a device. The nanodevice will be encapsulated in a casing that must be both bio-compatible (to resist rejection, inflammation and bio-fouling) and non-degradable. Polymer-based bio-compatible materials specifically for substrates, structures and packaging are surveyed by Qin et al. (2014). They show how these materials can meet the requirements of implantable biosensors and describe different packaging methods. Polymer based packaging will also have acoustic impedance similar to human tissue (see §3.2.1) and will have a minimal impact on the performance of the array. The overall scenario is illustrated in Fig. 4.1, where a nanodevice array is embedded into a polymer-based patch of bio-compatible tissue, and placed against a nerve's outer layer (*Epineurium*). The harvested ultrasound energy is converted by the devices and releases an electronic pulse that stimulates the nerve through an electrode. However, the devices must harvest sufficient power for releasing the required threshold amount of current to stimulate neuron bundles (fascicles) at different depths in a nerve. We must determine the levels of current and voltage needed to stimulate neurons, dimension arrays of nanodevices to effect the stimulation and then model the generation of a neural action potential (AP).
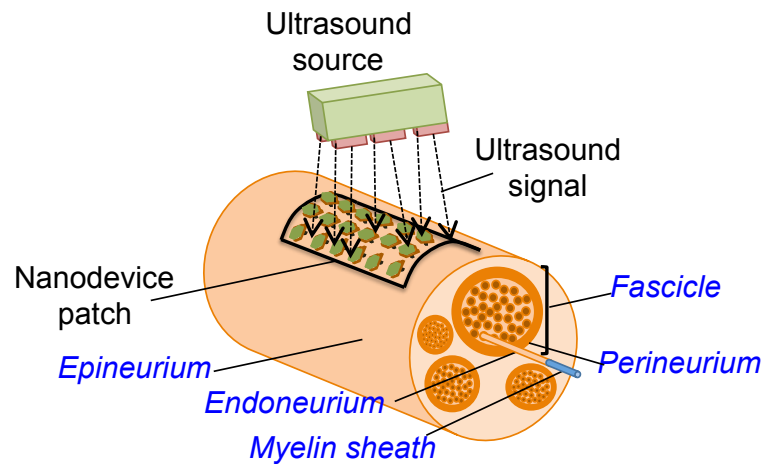
Fig. 4.1 Bio-compatible patch containing nanodevice array powered by externally generated ultrasound waves. The array sends current pulses to stimulate specific *fascicles* (nerve fibre bundles).

4.2 Neural Stimulation

Neurons have a resting potential, based on an ionic balance of sodium and potassium ions across the neural membrane, of approximately -70 mV. If a stimulus raises this potential above -55 mV (e.g., by applying a pulse of magnitude 15 mV or greater) then the neuron activates, generating an AP. The AP cycle duration from activation to completion (typically 5 ms) is called the *refractory period* (T_{ref}). A stimulus applied during this interval will not, in general, result in another action potential. The refractory period also ensures that an AP can only travel in one direction as the neuron will be de-activated in the opposite direction.

A stimulus can be supplied as part of the normal functioning of the nervous system or as an externally induced electrical current. External pulses are usually supplied by *cathodic* stimulation where a negative electrode is placed outside the cell membrane. The negative potential outside the membrane induces a current that reduces the trans-membrane voltage (depolarises) and will trigger an AP if the stimulus current and the resulting change in membrane potential is large enough.

The level of current needed to stimulate a neuron will depend on the excitability of the neuron, the electrode-neuron distance and the pulse duration. Larger diameter axons are more excitable and require lower stimulus energy than smaller diameters. Such larger axons have an insulating sheath of *myelin* and are classed as Aα, Aβ and Aδ. The myelin sheath has regular gaps at intervals of 2 mm, called *nodes of Ranvier* (typical width of 2 μm) where the AP is regenerated. These nodes are also the points at which an external stimulus pulse will enter the neuron.

Table 4.1 Axon Characteristics

Axon Type	Myelin	Diameter (μm)	Speed (m/s)	Chronaxie (μs)
Aα	Yes	13-20	80-120	50-100
Aβ	Yes	6-12	35-75	120
Aδ	Yes	1-5	10-35	170
B	Yes	3	3-15	200
C	No	0.2-1.5	0.5-2.0	400

The electrode voltage and the associated source current are important input values needed in order to determine the resultant currents and voltages induced in the neuron. Numerous research works have modeled the excitation of neurons using monopolar electrodes (BeMent and Jr., 1969; McNeal, 1976; Rattay, 2008) and we assume that such an electrode can be used in our model. In particular, we are interested in determining (i) the magnitude of a stimulus current that triggers an action potential, (ii) the electrode voltage needed to drive that current and (iii) the electrode position. This will allow us to determine the appropriate current and voltage required from the nanodevices to stimulate the neurons in the nerve. The calculation of stimulus current values using experimentally derived empirical equations is described in the next section.

4.2.1 Activation Parameters

The effect of the stimulus can be varied by increasing or decreasing the pulse length, and/or the intensity and hence influencing the activation of neurons of different size and depth in the nerve bundle. The lowest possible stimulus current of an axon is called the *rheobase* but this implies an infinitely long pulse (Brocker and Grill, 2013). The rheobase is usually measured at the source electrode. Due to the tissue resistivity, the rheobase will be higher when the electrode is placed at a certain distance (e.g., on the skin). A more usual parameter is the *chronaxie*, the minimum time required for a stimulus current that's twice the value of the rheobase to stimulate a neuron (Brocker and Grill, 2013). Factors affecting the accuracy of chronaxie measurements are discussed by Geddes (2004) who notes that the most reliable values are obtained when a square stimulus pulse is used. Axon characteristics, including their chronaxie value for different types of neurons are summarised in Table 4.1.

The source current intensity for stimulation must be increased as the distance between the electrode and the neuron increases. The increase in source current intensity with distance is defined by the *current-distance equation* (Brocker and Grill, 2013), which is
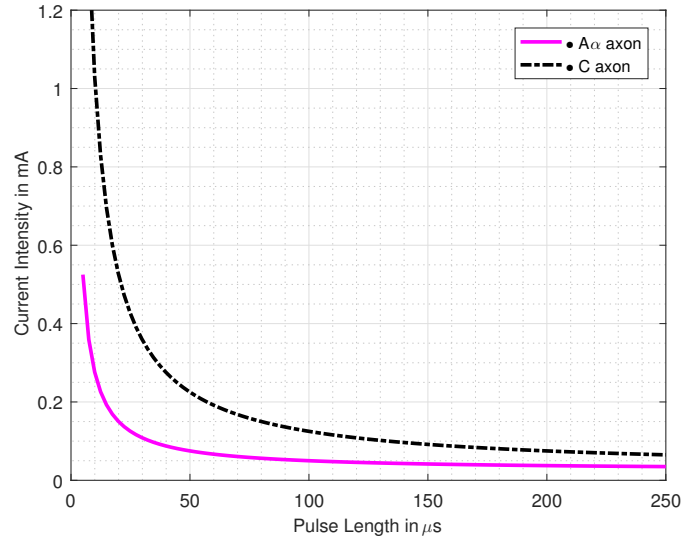
Fig. 4.2 Plot of current against pulse duration for two types of axon, one myelinated (Aα axon) and one unmyelinated (C axon). The current intensity for a pulse duration of 100μs is less than 0.2 mA.

represented as:

$$I_d = I_{th} + kd^2 \tag{4.1}$$

where the minimum threshold current for neuron activation at zero distance is I_{th}, the activation current intensity at a distance d, is I_d and the current-distance constant is k which is specific for different types of axon. Values of k were analysed by Ranck (1975) for a wide range of axon types and measured by varying methods. A more accurate method of determining the value for a peripheral motor neuron was devised by Mahnam et al. (2009) who also calculated a value for the threshold current I_{th}. In our modelling we use this calculated current-distance constant k of 27 μA/mm^2.

The pulse duration and the corresponding threshold pulse current intensity, I_{th}, for neural activation can be plotted using the Lapicque equation (Brocker and Grill, 2013), which is represented as:

$$I_{th} = I_r(1 + \frac{C}{t}). \tag{4.2}$$

where the pulse duration is t, the rheobase current is I_r and the chronaxie is C. The shorter the pulse duration, the higher the threshold intensity needed to activate a neuron. The optimum pulse duration for a specific neuron is the chronaxie. A plot of pulse duration (t) against current intensity (I_{th}), based on (4.2), using two values of chronaxie for a myelinated ($A\alpha$) and unmyelinated (C) axon is shown in Fig. 4.2.

44
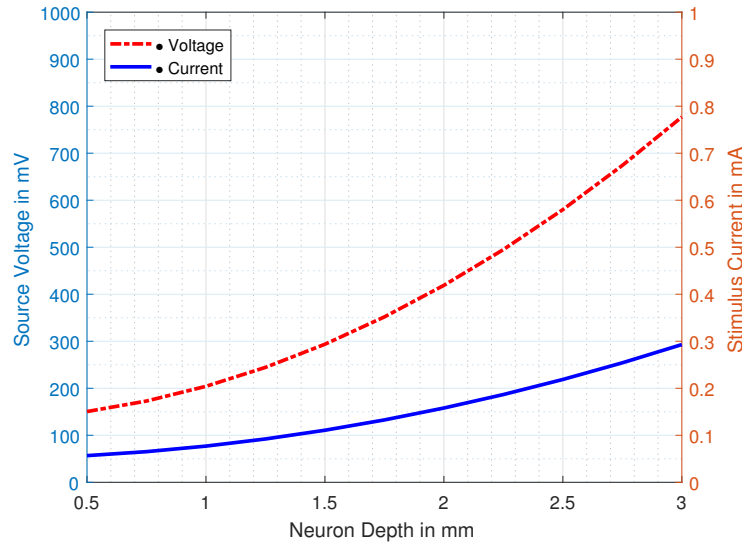
Fig. 4.3 Plot of stimulus current and source voltage for a range of neuron distances and a chronaxie of 100μs.

For an electrode in very close proximity to a nerve we model a rheobase current of 25 μA that's derived from Mahman's value of threshold current (50 μA) and a pulse length of 100 μs. If we consider a pulse length of 100 μs then we can see from Fig. 4.2 that the different axon types could be activated by a stimulus current of less than 0.2 mA.

The magnitude of the stimulus current will also depend on the voltage at the electrode. For a monopolar electrode, the electrical potential field V_u at a distance u is given by the following equation (Brocker and Grill, 2013) :

$$V_u = \frac{I_d}{4\pi\rho u} \tag{4.3}$$

where the stimulus current intensity is I_d and the conductivity of the extracellular tissue is ρ. If we assume a homogenous tissue then we can assign a specific value to the conductivity. A typical value for neuronal tissue conductivity is 0.3 S/m (Joucla and Yvert, 2012). The potential at zero distance is infinite so we assign a radius of 0.1 mm to the electrode in order to provide a minimum value of u and allow for a realistic source voltage (Durand et al., 2005). The variation in stimulus current (I_d) and source electrode voltage (V_u) with neuron depth, based on (4.1) and (4.3), for a neuron with a chronaxie of 100 μs stimulated by a 100 μs pulse is shown in Fig. 4.3. The further the neuron is from the nanodevice array electrode the higher will be the required stimulus voltage/current.

Table 4.2 Electrode voltage and stimulus current for a range of neuron depths.

Neuron Depth (mm)	Electrode Voltage (mV)	Stimulus Current (mA)
0.5	150.5	0.057
1	204	0.077
1.5	293	0.11
2	419	0.158
2.5	580	0.219
3	777	0.293

Values for electrode voltage and stimulus current, derived from (4.1) and (4.3), for a range of neuron depths are shown in Table 4.2. These values are comparable to experimental and modelling results for cuff electrode stimulation of peripheral nerves (Polasek et al., 2007).

The optimum position for a stimulating electrode is at a node of Ranvier but it is possible to trigger an action potential between nodes if the stimulus is strong enough. The stimulus current and corresponding electrode voltage are the key parameters that our energy-harvesting nanodevices must provide in order to stimulate neurons at different depths. We now examine the properties of specific peripheral nerves that we wish to stimulate.

4.2.2 Peripheral Nerve Fascicles

Peripheral nerves have neurons grouped in bundles (fascicles) within a nerve and so it is difficult to trigger a specific neuron. The peripheral nerves of the wrist and forearm that control arm and hand movements are the *radial*, *median* and *ulnar*. At the wrist and elbow, these nerves are buried beneath a layer of skin/fat (between 1 cm and 1.5 cm) and hence are easily accessed (McCahon and Bedforth, 2007). The cross-sectional areas of the nerves vary between 5 mm^2 and 10 mm^2 (Mani et al., 2011). Mapping the topography of fascicles through the median, radial and ulnar nerves was originally undertaken by Sunderland (1945). Further research was done by Jabaley et al. (1980) and Stewart (2003) to determine improved fascicle maps. These studies showed (i) the position of a fascicle could change within a nerve particularly after the nerve had branched and (ii) that key fascicles contained neurons of one type only (either motor or sensory). An accurate mapping of motor neurons to fascicles would provide valuable information for the placement of the nanodevices and the calculation of the probability of stimulating a particular neural response. A distribution of motor and sensory
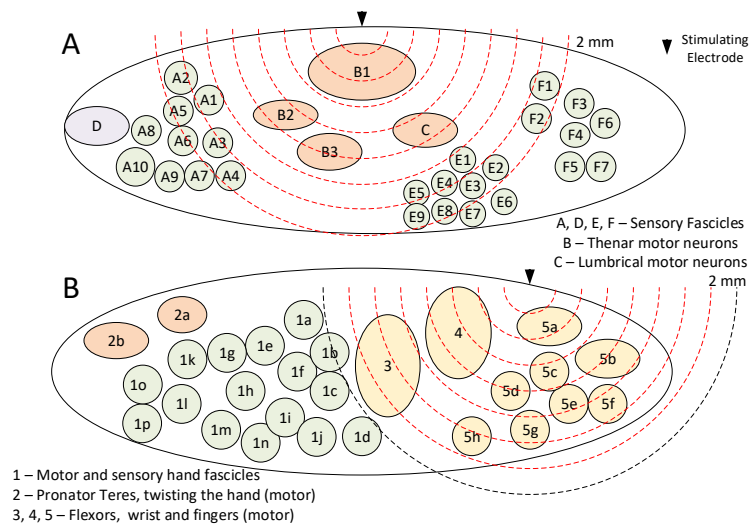
Fig. 4.4 Median nerve fascicles at the wrist (A) and the elbow (B), showing how electrode placement can concentrate the stimulating current on groups of motor fascicles.

fascicles in the median nerve, based on (Jabaley et al., 1980) and (Stewart, 2003), is shown in Fig. 4.4.

We model the median nerve as having an elliptical cross-section with a major diameter of 6 mm, a minor diameter of 2 mm, a cross-sectional area of 9.5 mm^2 and a perimeter of 13.4 mm. If a stimulating electrode is placed at the mid-point on the top surface of such a nerve then the radial distance from this point to the relevant fascicle will determine the level of stimulating current needed. However, if the motor fascicles are concentrated on one side of the nerve then the electrode should be placed on that side of the nerve to avoid stimulating other sensory fascicles. Examples of electrode placement on the median nerve at the wrist and elbow are shown in Fig. 4.4. In both cases the electrodes are placed to maximise access to the motor neuron fascicles and the stimulating current can be set to penetrate to the radial distances shown.

4.3   Nanodevice Neural Activation

A neuron's axon can be stimulated at any point along its length by an electrical pulse of sufficient magnitude. An activating nanodevice must (i) have sufficient voltage and charge for stimulation and (ii) allow for an interval of of at least 5 ms (the refractory period) between discharges. In theory, a neuron could be activated 200 times per second but this would be considered a very high rate for normal neural activity. Activation rates of 10 or less per second are more usual. Nerve stimulus currents are usually in the mA range (see Fig. 4.3), though the closer the stimulating electrode can
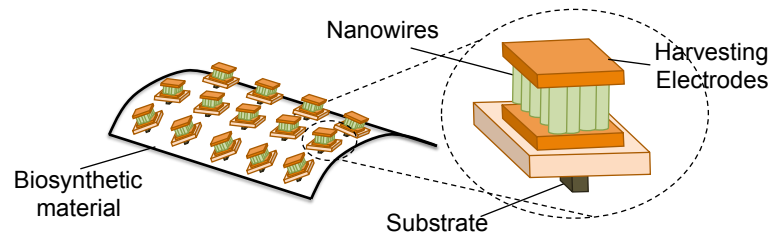
Fig. 4.5 Coupled nanodevices embedded in a patch of synthetic biocompatible tissue.

be placed to the nerve then the lower the requirement. Our modelled nanodevices have a maximum voltage level of tens of mV and produce current in the μA range (see Fig. 3.7). Therefore, based on these requirements, the nanodevices must be coupled together in parallel to increase the current and in series to increase the voltage. The coupling of individual ultrasound harvesting nanodevices in series to boost voltage output and in series to boost current output is described by Wang (2008). The experimental results show that the voltages and currents add as a linear superposition when the ultrasound is activated. The nanodevices should be capable of delivering square-wave pulses of varying duration across two electrodes, a cathode of coupled zigzag electrodes and an anode of coupled substrates, that can in turn stimulate a nerve. The minimum possible pulse length from a nanodevice driven by a 50 kHz ultrasound signal is 20 μs. A longer stimulation time will contain a train of such pulses. The in-built rectification and capacitive properties of the nanogenerator convert this train to a single square-wave DC pulse. Neural stimulation systems usually provide some form of charge balancing, delivering a biphasic pulse of cathodic current followed by anodic current. The claimed benefit is to minimize the degrading effects of charge build-up on the electrode and surrounding tissue. Our system is a passive device array and can only provide monophasic cathodic pulses. It cannot switch to biphasic operation or produce more complex stimulation patterns.

The method of inserting nanodevices in close proximity to neurons then becomes an important factor. We propose encasing an array of coupled nanodevices within a sealed patch of synthetic tissue, as illustrated in Fig. 4.5, and then inserting the patch of tissue at the site. The use of coupled arrays and bio-compatible packaging ensures that the individual nanodevices do not interact with the nerve or nerve fascicle but only act through a single cathode/anode system. The bio-compatible material provides insulation for the array in the surrounding conductive environment.

4.3.1 Array Dimensions

The nanodevice array must deliver a current intensity (I_d) in accordance to (4.1). That intensity in turn is also dependent on the pulse duration as shown in (4.2). If the output current level of a nanodevice at a particular ultrasound intensity is I_o, and the threshold stimulus current for a particular neuron depth is I_d, then the number of rows of coupled nanodevices to generate the threshold current, N_r, is:

$$N_r = \frac{I_d}{I_o}. \tag{4.4}$$

The voltage must also be in the range specified by (4.3) and calculated for an electrode radius of 0.1 mm. If the output voltage of a nanodevice at particular ultrasound intensity is V_o, and the electrode voltage for a particular threshold current is V_e, then the number of columns of coupled nanodevices to generate the threshold voltage, N_c is:

$$N_c = \frac{V_e}{V_o}. \tag{4.5}$$

The median and ulnar nerves are contained in a skin/fat depth between 1 cm and 1.5 cm. The external ultrasound intensity will have dropped below its initial intensity of 720 mW/cm^2 at these depths. Hence we use a maximum intensity of 710 mW/cm^2 with a maximum current and voltage per nanodevice of 1.42 μA and 27.5 mV. The minimum possible area of a patch of nanodevices, A_p will be derived from the number of rows N_r, the number of columns N_c and the area of one nanodevice a_n as follows:

$$A_p = N_r N_c a_n. \tag{4.6}$$

The basic length and width of an array of nanodevices are set by the number of rows and columns. Our nanodevices are 1000 μm^2 and can be modelled as squares of side 32 μm. There will be a need to allow for small variations in dimension as well as a space for coupling connections between the devices. We, therefore, increase the effective size of a nanodevice to 40 μm per side, giving an effective area of 1600 μm^2. A plot of minimum array area (A_p) for a range of neuron depths, pulse durations and two different ultrasound input intensities, based on (4.6), is shown in Fig. 4.6. The plots show how the area increases for greater stimulus depth and shorter pulse lengths, since both of these will result in higher current and voltage. The area decreases for higher ultrasound intensity as each device can produce more current and voltage. Nanodevice array dimensions of length and width are based on translating the number of rows and columns into equivalent dimensions in millimetres. For example, at a
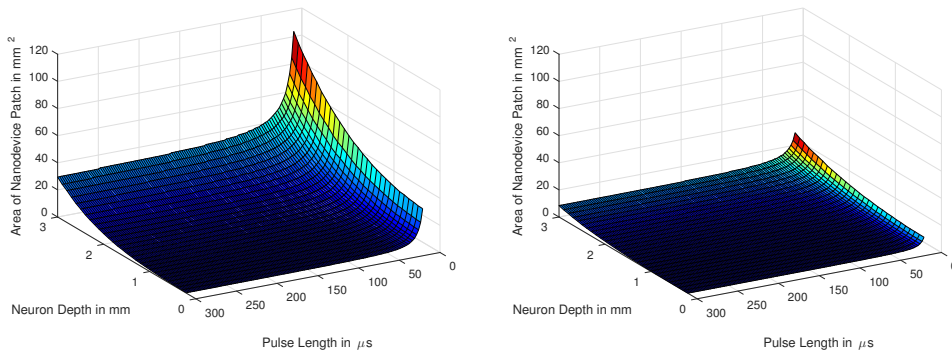
(a) Ultrasound Intensity 200 mW/cm^2 (b) Ultrasound Intensity 710 mW/cm^2

Fig. 4.6 Nanodevice array area for a range of neuron depths, pulse lengths and two ultrasound intensities.

skin/fat depth of between 1 cm and 1.5 cm there would be an ultrasound intensity of 710 mW/cm^2 with a maximum individual nanodevice voltage of 27.5 mV and current of 1.42 μA. It would require 73 nanodevices in series to deliver 2 V and 141 nanodevices in parallel to deliver 200 μA, giving an array of 3 mm by 5.64 mm or 16.92 mm^2. It is possible to subdivide the rows and columns into coupled blocks in order to increase the width and reduce the length of an array. The block coupling would preserve nanodevice parallel and series wiring but would extend some connections to allow the rearrangement of blocks in the array. The maximum possible width of the array is half the circumference of the nerve or fascicle that the array will be placed on.

4.3.2   Selectivity of Activation

A fixed-size array of nanodevices can be designed to stimulate the deepest motor neurons in a nerve but in doing so the current will also stimulate all closer motor neurons. Some degree of depth selectivity can be engineered by (i) using a variable-width ultrasound beam that can irradiate different parts of an array and (ii) reducing the incident ultrasound intensity over the full array.

When the ultrasound beam is directed at smaller areas of an array, then lower intensity stimulus pulses can be generated. We consider an array, for example, with sufficient rows and columns to stimulate motor neurons at a maximum depth in a nerve of 3 mm at maximum ultrasound intensity. The sub- area (length and width) that needs to intercept ultrasound energy for different depths of neuron stimulation is shown in Table 4.3. The *additional* fascicles stimulated at each depth are also shown based on the distribution in Fig. 4.4.

Table 4.3 Array dimensions for neuron activation at specific depths and a constant ultrasound intensity of 710 mW/cm^2.

Depth (mm)	Length (mm)	Width (mm)	Fascicles
1	2.16	0.28	5a, 5c ,4, B1
1.5	3.12	0.55	5b, 5d, 5e, 5f, 5g, 4, B2, B3, C
2	4.44	0.6	5h, 3, A1, A2, A3, A4, A5, F1, F2, E1, E2, E3, E4, E5, E8, E9
2.5	6.16	0.84	1a,1b, 1c, 1d, 1f, A6, A7, A8, A9, F3, F4, F5, F6, E6, E7
3	8.24	1.12	1e, 1g, 1h, 1i, 1j, F7, A10, D

Reducing the intensity of an ultrasound beam on a fixed array size will also reduce the resultant current and voltage and hence the stimulus depth. The stimulus depth d can be expressed as a function of stimulus current I_d by rearranging (4.1) as follows:

$$d = \sqrt{\frac{I_d - I_{th}}{k}}.$$

(4.7)

The stimulus current (I_d) in turn can be expressed as a function of ultrasound intensity (U_r) by combining (4.4), (3.14) and substituting in (4.7) to give the following expression for d:.

$$d = \sqrt{\frac{(N_r I_o) - I_{th}}{k}}$$
$$= \sqrt{\frac{(N_r A e U_r) - I_{th} V_o}{k V_o}}$$

(4.8)

where the number of rows of nanodevices is N_r, the area of a nanodevice is A, the output efficiency is e and the output voltage of a nanodevice is V_o. We will take the example of an array dimensioned to stimulate neurons at a depth in the nerve of 3 mm when subjected to an ultrasound intensity of 710 mW/cm^2. A reduction in ultrasound intensity U_r causes a reduction in stimulus current I_d with a corresponding reduction in stimulus depth d. A plot of the reduction of ultrasound intensity (U_r) on such a fixed-size horizontal array and the effect on stimulus depth (d), based on (4.8), is shown in Fig. 4.7.

In order to calculate the intensity of an ultrasound beam across an elliptical or circular nerve we need to calculate the slope of a tangent at any point on the curved surface. An ellipse with a semi-major axis a and a semi-minor axis b will have a slope s at any
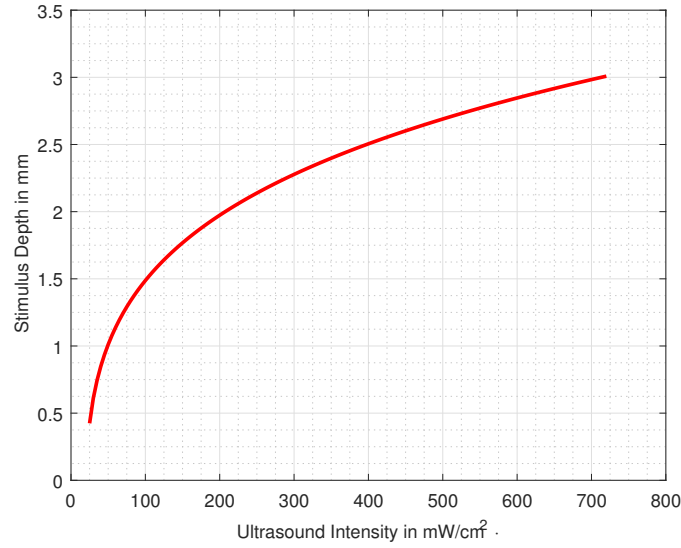
Fig. 4.7 Plot of Ultrasound Intensity vs. Stimulus Depth for a fixed-size array (8.24 mm length, 1.12 mm width) of nanodevices.

point (x, y) as follows:

$$s = \frac{dy}{dx} = -\frac{x/a^2}{y/b^2}.$$ (4.9)

This slope value can be converted to an angle in radians using *arctan*. The ultrasound intensity at a particular depth, U_r, will be reduced around the curved surface as follows:

$$U_e = cos(arctan(s))U_r$$ (4.10)

where U_e is the reduced ultrasound intensity on the curved surface. Examples of how an ultrasound intensity of 710 mW/cm^2 decreases, based on (4.10), from the centre to the edges of an elliptical nerve and a circular nerve are shown in Fig. 4.8. The modelled surface segment of the elliptical nerve has a major axis of 6 mm, a minor axis of 2 mm and a length of 5 mm. The circular nerve segement has a diameter of 6 mm. The reduction in incident ultrasound intensity on a curved patch will cause a reduction in stimulus current and stimulus depth. The actual reduction will depend on how much of the patch rests on the curved edge of the nerve surface. In both cases the maximum intensity occurs on the part of the nerve surface that is normal or near-normal to the incident beam (e.g., the midpoint). As the angle of curvature increases, the intensity decreases but the effect is more pronounced on a circular cross-section. This suggests that the width of a nanodevice array, or the deployment of multiple arrays, must be tailored to the type of nerve (elliptical or circular cross-section) in order to maximise energy harvesting.

52

(a) Elliptical cross-section.　　　　　　(b) Circular cross-section.
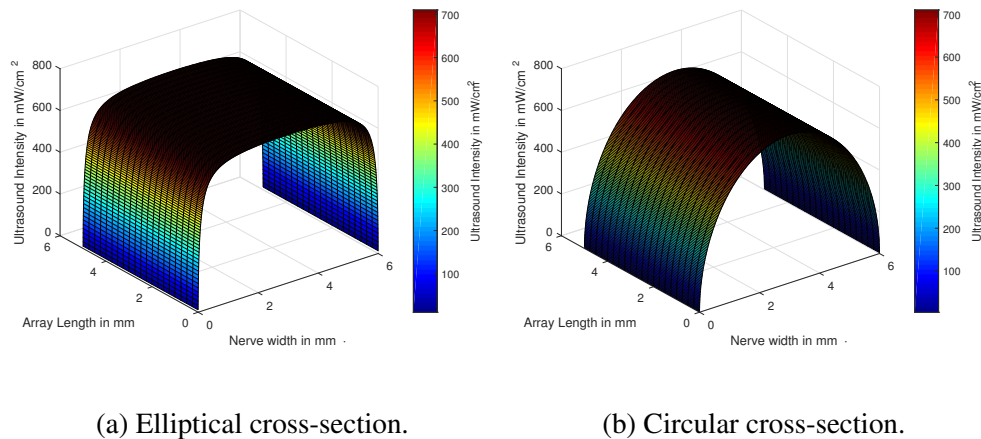
Fig. 4.8 Ultrasound intensity across (a) an elliptical cross-section nerve (major axis 6mm) and (b) a circular cross-section nerve (diameter 6mm).

The maximum possible AP pulse rate is limited by the refractory period of the stimulated fascicles. A higher aggregate pulse rate could be achieved through selectively stimulating individual fascicles. Selective stimulation implies that one fascicle can be activated without activating neighbouring fascicles (spatial selectivity). Stimulating single fascicles would provide a method for increasing the number of pulses per second that could be transmitted along a nerve. It is also possible to selectively stimulate neurons of a particular diameter in a fascicle that contains different types of neuron (diameter selectivity). A stimulus pulse from an electrode will selectively stimulate fascicles based on the following parameters:

- The strength and duration of the stimulus current will determine how deep into the nerve the stimulus will travel;

- The closest fascicles will be stimulated before more distant ones (current-distance relationship);

- Among close fascicles, myelinated neurons will be stimulated before non-myelinated (pulse duration);

The most difficult fascicle targeting to achieve is to stimulate a deep fascicle without stimulating closer fascicles. The only method for achieving this in limited circumstances is the generation of sub-threshold stimulus pre-pulses as described by Grill and Mortimer (1995). These pre-pulses can temporarily raise the stimulus threshold of the closest fascicle allowing a follow-on pulse to stimulate a deeper fascicle. However pulse timing, pulse length and pulse interval are crucial in implementing this.

A further degree of selectivity can be achieved by deploying multiple electrodes at different locations across a nerve surface. This would require either embedding separate arrays or providing multiple arrays within a single patch. The stimulating electrodes would be positioned as close as possible to the target fascicles and engineered to deliver the stimulus current. The electrodes would be energised either singly simultaneously by the ultrasound beam and the system could be modelled as a multipole electrode with careful attention paid to interaction between the stimulus currents (Sweeney et al., 1990; Tarler and Mortimer, 2004).

4.4   Summary

There are specific minimum levels of current, voltage and stimulus pulse-length needed to stimulate APs in nerve fascicles. Energy harvesting nanodevices must be coupled in series and parallel in order to provide the required stimulus energy levels. Higher levels of voltage and current will penetrate to a greater depth into a nerve and stimulate more fascicles. However the activation of a neuron by a stimulus depends not only on the depth but also on the neuron diameter and whether or not the neuron has a coating of myelin. Larger diameter myelinated neurons are more readily stimulated than smaller diameter and unmyelinated neurons. A limited degree of selective activation of specific fascicles is possible but greater selectivity would require multiple arrays and multiple electrodes.

Chapter 5

Neural Data Transmission System

5.1 Introduction

The previous chapter described the stimulation of nerves by energy-harvesting nanodevice arrays. In this chapter we describe how a nerve can provide a digital communications channel using *multiple* stimulated neurons in fascicles as data pulses. In order to dimension such a transmission system we need to know: (i) the maximum number of pulses per second that a nerve can support; (ii) the amplitude and attenuation of the pulse to determine the pulse range and intensity; (iii) the level of noise or distortion in the nerve and (iv) the modulation that is suited to the natural signaling properties of the nerve.

These values and parameters allow us to calculate the resulting bit rate at different distances from the stimulus point. The embedded transmission device would generate modulated stimulus pulses along a nerve for interpretation by an embedded receiving device. The information rate will depend on many factors such as: (i) the number and type of neurons that are stimulated; (ii) the spread in velocities of the APs; and (iii) the exact position of the detecting electrodes. The stimulus pulses should not interfere with the normal working of the nervous system and should be applied in situations where the muscle or organ at the nerve extremity was damaged and could not terminate normal nerve impulses.

5.2 Single and Compound Action Potentials

The levels of single and multiple action potentials can be measured as follows:

- The *intracellular action potential (IAP)* is the trans-membrane voltage measured from the inside of the neuron to the outside across the neural membrane and will have a maximum value of approximately 30 mV.

- The extracellular action potential or *single fibre action potential (SFAP)* is measured on the outside of the neuron with respect to the surrounding extracellular medium and will be much smaller in magnitude (nanovolts) than the IAP.

- The *compound action potential (CAP)* is the algebraic sum of multiple SFAPs arising from the same external stimulus and measured on the outside of the neuron. The magnitude will depend on how many neurons are simultaneously activated.

5.2.1 Intracellular and Extracellular Action Potential

An empirical IAP model devised by Nandedkar and Stalberg (1983) was based on an earlier version by Rosenfalck (1969). This model can be expressed in the space domain and the time domain to generate the shape and magnitude of the IAP based on experimental values. The space domain version is expressed across a distance *z* while the time domain version uses the transform $z = vt$ where *v* is the velocity of the IAP and *t* is the time parameter. Three shaping parameters are used: α for the rising part of the IAP, β for the exponential reduction and γ for the resting potential. The empirical formula for the time domain IAP, $\phi_{iap}(t)$, may be written as:

$$\phi_{iap}(t) = \alpha t^3 e^{-\beta t} - \gamma \tag{5.1}$$

The time-based version produces an IAP that has a duration appropriate for a range of cellular tissue including neurons of different types. This formula was originally devised for muscle fibre with $\alpha = 49152$ mV/ms^3, $\beta = 8$/ms, $\gamma = 90$ mV and a velocity of 4 $m.s^{-1}$. We modify the shape of the time-based version to match the experimental shape of a myelinated neuron IAP by: i) changing the resting potential, γ, to -70 mV, ii) setting the value of $\alpha = 36864$ mV/ms^3 to generate a peak voltage of 30 mV and iii) retaining the value of β. Our modified empirical equation is:

$$\phi_{iap}(t) = 36864t^3 e^{-8t} - 70. \tag{5.2}$$

A plotted example of our modelled IAP ($\phi_{iap}(t)$), based on (5.2), for a myelinated neuron is shown in Fig. 5.1. We will use this time-based IAP model in our calculation
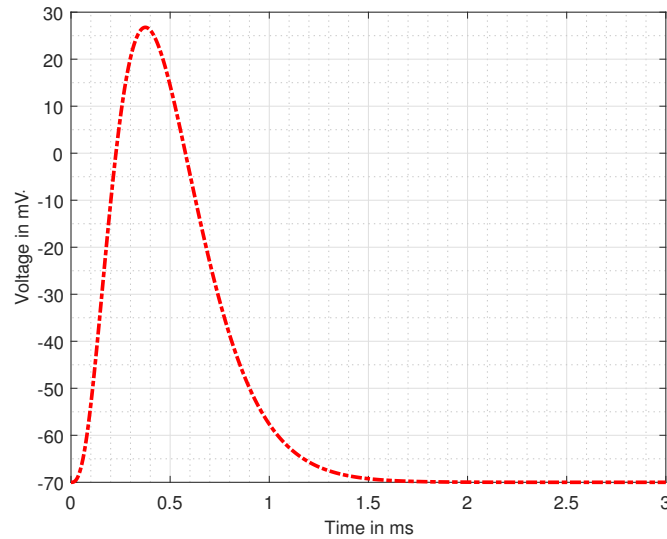
Fig. 5.1 Time-based intracellular action potential (IAP) model for a myelinated neuron.

of the extracellular single fibre action potential *(SFAP)*.

The calculation of potential at a point in a conducting extracellular medium arising from a travelling current source is based on the principles of volume conduction (Rutkove, 2007). The SFAP is computed from a convolution of (i) a source excitation and (ii) a weighting function based on the exact position of the detecting electrode along the fibre. If we model a single neuron as a long thin cylinder then we can define the direction of propagation of an SFAP as along the *z* axis and the initial excitation point as $(0,0,0)$. The detection point for the SFAP is outside the fibre at location (x_0, y_0, z_0) in the extracellular domain as shown in Fig. 5.2. The extracellular potential at this point will vary with the radial distance from the propagating source of excitation (Malmivuo and Plonsey, 1995). The radial distance will vary specifically with the longitudinal propagation distance and can be expressed as $r(z)$ once the detection point is a fixed perpendicular distance *p* (in the *xy* plane) from the fibre. The potential at a specific time can be expressed as an integration of the contributions of all transmembrane current sources of length *dz*. Two types of model have been developed for SFAPs: monopole models based on transmembrane current (second derivative of the IAP) and dipole models based on dipole moment (first derivative of the IAP). Monopole models were developed by Plonsey (1974) and Nandedkar and Stalberg (1983) and a dipole model was developed by Dimitrova et al. (1999). These were analysed by Falces et al. (2005) who noted that the dipole model gave better results at boundaries and was more consistent with experimental data. We will use a dipole model in our derivation of the SFAP and our formulation is based on the equation
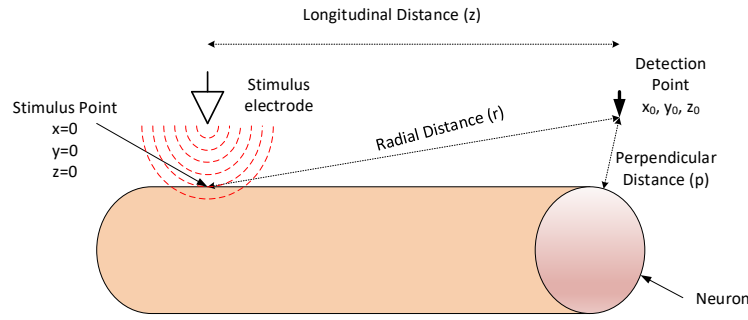
Fig. 5.2 Schematic view of the stimulating and detection of single fibre action potentials (SFAPs) along a single neuron.

derived by Falces et al. (2005). The extracellular potential at time t, $\phi_e(t)$, for a neuron of radius a can be modelled as the output signal of a linear system and computed as the convolution of two time dependent functions as follows:

$$\phi_e(t) = \frac{a^2 \sigma_i}{4 \sigma_e v} \frac{\partial \phi_{iap}(t)}{\partial t} * \frac{\partial \frac{1}{r_v(t)}}{\partial t} \qquad (5.3)$$

where the intracellular conductivity is σ_i, the extracellular conductivity is σ_e and the conduction velocity is v. The radial distance, $r_v(t)$, can be expressed as:

$$r_v(t) = \sqrt{(z_0 - vt)^2 + p^2} \qquad (5.4)$$

where the longitudinal distance is (z_0) and the perependicular distance is p. The radial distance will be at minimum when the IAP reaches the longitudinal distance (z_0) of the electrode from the source. The SFAP conduction velocity, v, is also proportional to the diameter of a neuron, $d(=2a)$, and can be expressed as:

$$v = hd \qquad (5.5)$$

where the constant of proportionality, h, is approximately 6 for myelinated neurons when the velocity is expressed in m/s (or mm/ms) and the diameter is expressed in μm (Struijk, 1997). We fix the value of extracellular conductivity, σ_e, at 0.3 S/m and the intracellular conductivity, σ_i, at 1 S/m (Joucla and Yvert, 2012). Our modelled example of SFAPs for myelinated neurons of two different diameters, based on (5.3), is shown in Fig. 5.3a. The duration of the SFAP is the same in each case (approximately 2.55 ms) but the time taken to reach the detection point is longer for the lower diameter (and lower velocity) neuron. The recorded SFAPs are tri-phasic with both positive and
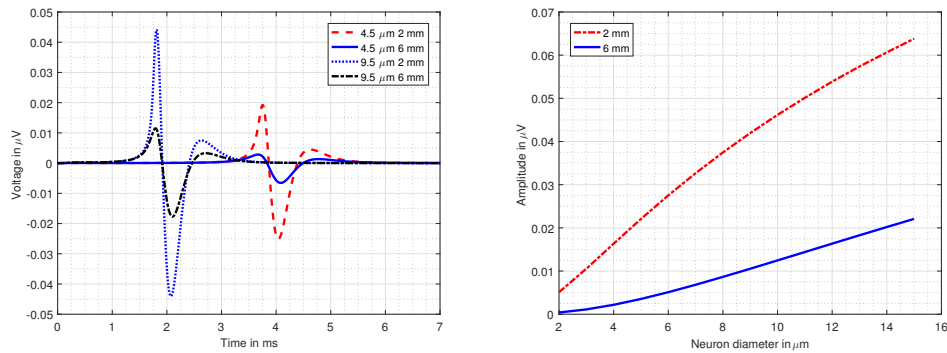
(a) SFAPs for 4.5 μm and 9.5 μm neurons.   (b) SFAP amplitude (positive peak).

Fig. 5.3 Variation of SFAP amplitude with neuron diameter and two electrode perpendicular distances at a fixed longitudinal distance of 100 mm.

negative peaks. The amplitudes of the SFAP peaks depend not only on the relative positions of the source and detecting electrode but also on the conductivity ratio between the intracellular medium and the extracellular medium, as shown in (5.3). The relationship between SFAP amplitude (for positive/negative peaks) and neuron diameter is approximately linear for the range of diameters that we are studying (Struijk, 1997) and is shown for the larger positive peak, based on (5.3), in Fig. 5.3b. The highest frequency for generating SFAPs is limited by the refractory period (up to 5 ms) and will be approximately 200 pulses/sec.

An SFAP for a single neuron is difficult to detect because of its low amplitude and the possibility of interference from other neurons. However, a stimulus pulse of sufficient strength will trigger multiple SFAPs in one or more fascicles. The SFAPs will sum algebraically to give a compound action potential (*CAP*) which is easier to detect by an extracellular receiver because of the higher summed voltage although the peak voltage may still be of the order of microvolts or low millivolts.

5.2.2   CAP Simulation

We model CAP measurement over multiple neurons in a similar way to that shown for a single neuron in Fig. 5.2. The peripheral nerves that we are considering (sural, median, radial) are elliptical or circular in cross-section with average radii ranging from 1.7 mm (median) to 1.5 mm (sural). The minimum perpendicular detection distance occurs when the detecting electrode is on, or very close to, the surface of the nerve. The neurons are at varying distances from the detection point with corresponding differences in SFAP amplitudes. Wijesinghe et al. (1991) show the average distance of neurons from the centre of the nerve can bet set at a value of 0.66 of the nerve radius

without loss of accuracy in CAP calculation. We adapt this model with the neurons concentrated at the centre of the nerve and the detecting electrode set at slightly greater than the typical peripheral nerve radius. A minimum perpendicular detection distance of 2 mm ensures that the nerve dimensions and neuron distances are properly accounted for in simulating multiple SFAPs without overestimating the magnitude of the resulting CAP. The duration (width in time) of a CAP will depend on what fraction of the neurons in the fascicles are stimulated and the velocity of propagation of the SFAPs. Schoonhoven et al. (1986b) used a volume conduction and convolution model, similar to the one we described in §5.2.1, to compute SFAPs and then combined these mathematically into a CAP. Models for CAPs were also developed by Wijesinghe et al. (1991) based on similar principles. The general formulation states that a CAP at a time t and distance l from the stimulating electrode may be expressed as:

$$CAP(t,l) = \sum_{j=1}^{N} \phi_{ej}(t - \tau_j; v_j) \qquad (5.6)$$

where there are N active fibres in total in the nerve, ϕ_{ej} is the SFAP of the jth neuron and the conduction velocity is v_j (constant for a given neuron). The arrival time of the stimulus at the detection point, τ_j, is derived from the distance l and the SFAP velocity v_j as follows :

$$\tau_j = \frac{l}{v_j}. \qquad (5.7)$$

If the neurons are of different diameter then the SFAPs will have different velocities and the CAP at distance l will show spreading from the variation in SFAP arrival times. Substituting (5.5) in (5.7) we get the arrival time based on diameter:

$$\tau_j = \frac{l}{hd_j}, \qquad (5.8)$$

where d_j is the neuron diameter and the constant of proportionaliy, h, is set at 6 for myelinated neurons. The CAP amplitude will reduce with longitudinal distance because the underlying multi-speed SFAP bi-phasic peaks will progressively start to cancel each other out (Wijesinghe et al., 1991) giving a reduced summation. We compute the *dispersion*, D, as the rate of change of propagation time t with respect to neuron diameter d and distance z at any given point as follows:

$$D = \frac{1}{z}\frac{dt}{dd} \qquad (5.9)$$
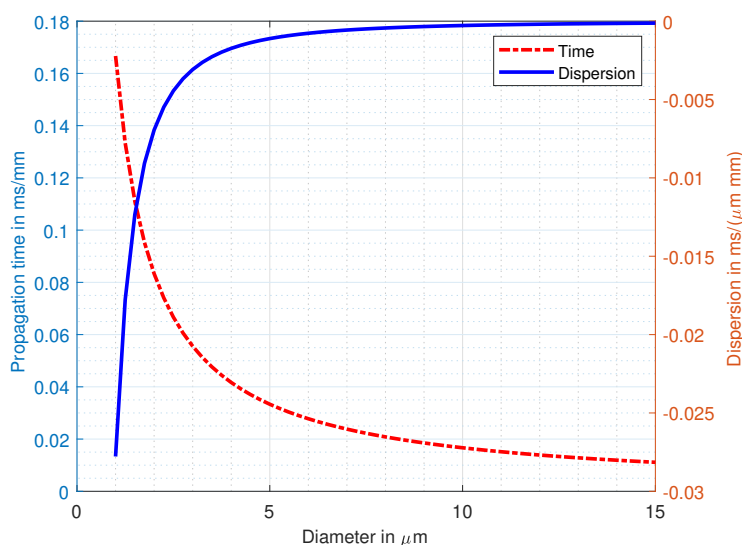
Fig. 5.4 Spread of arrival times of SFAPs in ms/mm for varying neuron diameters. The dispersion in ms/μm/mm is also shown.

Dispersion is expressed per unit length as ms/μm/mm. Each neuron diameter has its own value of dispersion but it is possible to use a single value of dispersion over a narrow range of diameters to simplify calculation of pulse spread. This spreading in time of a CAP is analogous to the dispersion that occurs in an optical fibre when a propagating optical pulse contains a range of wavelengths (Snyder A.W., 1983) that travel at slightly different velocities. A plot of propagation times for SFAPs over a range of diameters (and hence velocities), based on (5.8), is shown in Fig. 5.4 for a distance of one mm. The dispersion of the SFAPs, based on (5.9), is also shown in Fig. 5.4. A nerve or fascicle with a greater proportion of smaller diameter neurons and lower conduction velocities will generate a CAP with a lower amplitude and with greater spreading over distance than a fascicle with a greater proportion of larger diameter neurons. Axon densities and diameter distributions for the radial and sural nerves were estimated by O'Sullivan and Swallow (1968). We model a nerve with a total of 10,000 neurons, similar to the *sural nerve model* used by Stegeman et al. (1988). A peripheral nerve of this type has multiple fascicles with a bimodal spread of neural diameters around 4.5 μm and 9.5μm as shown in Fig. 5.5a.

We use this distribution to generate three different CAPs: (i) a bimodal CAP from all the neuron diameters, (ii) a single mode CAP from the distribution of lower speed neurons with smaller diameters and (iii) a single mode CAP from the higher speed neurons with larger diameters. The resulting CAPs are generated by summing all the calculated SFAPs, based on (5.6), and are shown in Fig. 5.5b. We fix the perpendicular
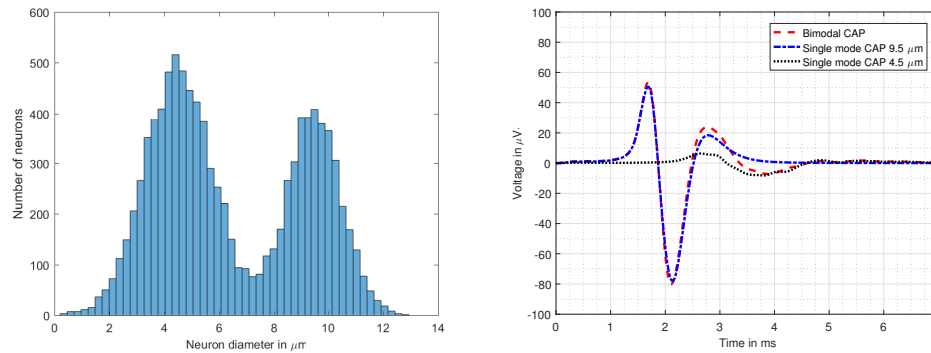
(a) Histogram of sural nerve neurons.   (b) Bimodal CAP and single-mode CAPs.

Fig. 5.5 Histogram and CAPs for sural nerve with 6000 neurons with a mean diameter of 4.5 μm and 4000 neurons with a mean diameter of 9.5 μm.

distance of the detection electrode at 2 mm. A single mode CAP can be generated from higher velocity SFAPs if the stimulus pulse intensity and duration are set to stimulate larger diameter neurons in a fascicle. A more intense and longer duration stimulus pulse will stimulate both larger and smaller diameter neurons creating a bimodal CAP with higher velocity and lower velocity SFAPs. The bimodal CAP shows that the larger diameter neurons dominate even though numerically there are more neurons of lower diameter. The change in amplitude (positive and negative peaks) and duration (spread) of a CAP will be important parameters in assessing the use of CAPs as pulses for data transmission.

5.2.3   CAP Data Pulses

A data transmission system requires a data source, transmission channel and a receiver. In our model an external source will convert data into coded ultrasound stimulus pulses for transmission to an embedded nanodevice array. The array will stimulate fascicles in a nerve and create a corresponding stream of coded CAPs. A receiver at the distant end must detect these CAPs, record them and interpret them using some decoding algorithm. We will use the positive peak of a single mode CAP as a measure of the amplitude of a pulse. This peak will decline with distance and the CAP will broaden. We now define an equivalent data pulse format primarily to simplify our computations while retaining all the attributes of a CAP.

- We model the CAPs using Gaussian pulses to replicate the attributes of CAPs (decreasing amplitude, increasing width) as they propagate along a nerve without contravening the limit set by the refractory period.

62

- The amplitude is based on a mean neuron diameter $\bar{d}$ and a standard deviation in diameter σ_d.

- The width of the Gaussian pulse in time is a standard deviation based on the spread of propagation velocities of the constituent SFAPs.

- The symbol rate of the nerve can be calculated within the constraints of the *refractory period* and the *inter-symbol interference (ISI)* caused by pulse spreading.

- The maximum possible capacity (Shannon capacity) of the nerve is computed from the symbol rate and the *signal-to-noise ratio (SNR)* of the nerve. The actual capacity will depend on constraints like the refractory period and the modulation method.

We evaluate our neural transmission system by modelling two single mode CAPs as Gaussian pulses. The amplitude is based on the average of a number of summations of SFAP positive peaks for (i) 6000 neurons with a mean diameter, of 4.5 μm and a standard deviation in diameter of 1 μm and (ii) 4000 neurons with a mean diameter of 9.5 μm and a standard deviation in diameter of 1 μm. The equation for our Gaussian pulse voltage with respect to time, $V(t)$, is as follows:

$$V(t) = A_{max} e^{\frac{-(t-\mu_{cap})^2}{2\sigma_{cap}^2}} . \tag{5.10}$$

The peak amplitude of the Gaussian pulse CAP (from the summed SFAPs) at the point of measurement (z) is the positive peak A_{max}. The time (in ms) at which the peak amplitude is detected at the fixed detection point provides the mean, μ_{cap}, of the modelled pulse. The width of a CAP in time has a minimum value set by the width of the underlying SFAPs (2.55 ms). Our equivalent Gaussian pulse replicates this minimum value with a core standard deviation of one-sixth of this width (0.425 ms). The total standard deviation in time of the modelled CAP, σ_{cap}, is calculated from two components: (i) a core standard deviation of $\sigma_0 = 0.425ms$ added to (ii) the broadening due to dispersion calculated from the standard deviation of the underlying diameters (and hence velocities) at any time t. We can calculate the pulse broadening, ΔP, over a length z due to dispersion as follows:

$$\Delta P = D_{\bar{d}} \sigma_d z \tag{5.11}$$
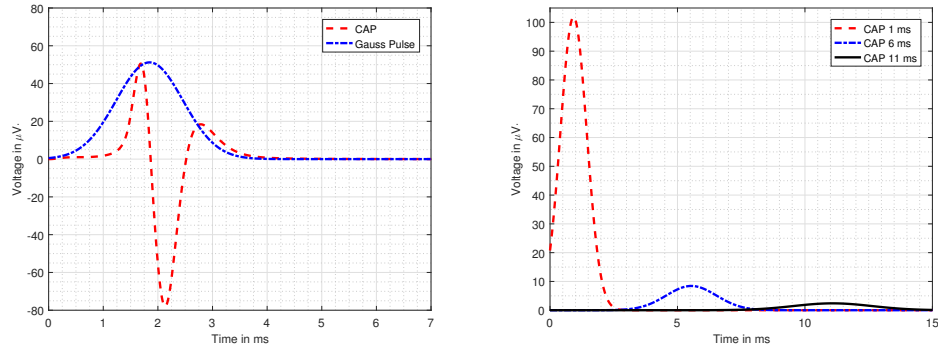
(a) Gaussian pulse compared with equiv-
alent CAP at a detection distance of 100
mm.

(b) Gaussian CAP pulse amplitude and
spreading at intervals of 1 ms, 6 ms and
11 ms.

Fig. 5.6 Gaussian pulses modelled on a CAP generated from 4000 neurons with a mean diameter of 9.5μm and standard deviation of 1 μm

where the dispersion of the mean diameter is $D_{\bar{d}}$ (see §5.2) and the standard deviation of the diameter range is σ_d. The modelled CAP Gaussian pulse will then have a total standard deviation (in ms) as follows:

$$\begin{aligned} \sigma_{cap} &= \Delta P + \sigma_0 \\ &= D_{\bar{d}}\sigma_d z + \sigma_0 \\ &= D_{\bar{d}}\sigma_d z + 0.425. \end{aligned} \qquad (5.12)$$

This ensures that the width of the modelled Gaussian pulse, a combination of the underlying CAP width plus the broadening due to dispersion, is comparable to the width of the corresponding simulated CAP. Examples of CAPs modelled as a Gaussian pulses, based on (5.10) and (5.12), are shown in Fig 5.6. The peak amplitude for a fascicle with k neurons at a measuring distance z is $A_k(z)$. This peak amplitude can be averaged over a number of simulations and modelled by an empirical exponential function as follows:

$$A_k(z) = G_k e^{-\alpha_k z} \qquad (5.13)$$

The empirical parameters G_k and α_k will have values that depend on the mean neuron diameter, the standard deviation of the diameters and the number of neurons in the fascicle. The reduction in amplitude and the increase in spread of our modelled CAPs as the detection distance increases, based on (5.13), is shown in Fig. 5.7. We now examine how a stimulated stream of CAPs can be used for data communications.

64
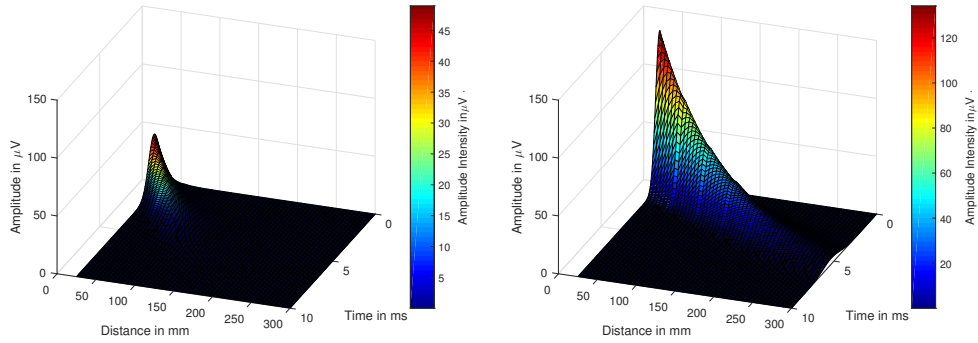
(a) CAP for 6000 neurons with a mean di-
ameter of 4.5μm.

(b) CAP for 4000 neurons with a mean di-
ameter of 9.5μm.

Fig. 5.7 Gaussian pulse model of CAPs showing decrease in amplitude and increase in pulse spread with distance and time.

5.3 Neural Data Channel

We model CAPs as symbols to convey information in bits. The capacity of the system is determined by (i) the symbol rate (symbols per second), (ii) the number of different symbols and (iii) the number of bits that each symbol represents. The maximum possible symbol rate is limited to 200/s by the total refractory period, T_{ref}, if a normal level of stimulus is used (see §4.2). Pulse spreading increases the probability of ISI and is countered by reducing the symbol rate. The basic symbol rate for any Gaussian pulse is calculated using a peak-to-peak time difference at the point of detection of approximately four times the standard deviation ($4\sigma_{cap}$). If we compare T_{ref} with $4\sigma_{cap}$ we get the following expressions for symbol rate S_{cap}:

$$
\begin{aligned}
S_{cap} &= \frac{1}{T_{ref}}, T_{ref} \geq \frac{1}{4\sigma_{cap}} \\
S_{cap} &\approx \frac{1}{4\sigma_{cap}}, T_{ref} < \frac{1}{4\sigma_{cap}}.
\end{aligned}
\tag{5.14}
$$

The symbol rate will be in symbols/s if σ_{cap} is expressed in seconds. By substituting (5.12) we can calculate the effect of pulse spreading on the symbol rate:

$$
\begin{aligned}
S_{cap} &\approx \frac{1}{4(D_{\bar{d}}\sigma_d z + \sigma_0)}, T_{ref} < \frac{1}{4\sigma_{cap}} \\
&\approx \frac{1}{4(D_{\bar{d}}\sigma_d z + 0.425)}.
\end{aligned}
\tag{5.15}
$$

Fig. 5.8 Symbol rates for a CAP of 6000 neurons with a mean diameter of 4.5 μm and a CAP of 4000 neurons with a mean diameter of 9.6 μm. The symbol rate drops at the point where the inter-pulse interval exceeds the refractory period.

The symbol rate crossover points from T_{ref} to $4\sigma_{cap}$ for our modelled CAPs, based on (5.15), are shown in Fig. 5.8. The symbol rate itself does not define the channel capacity as the presence of noise in a channel will dictate the number of symbols, M, and the number of bits per symbol (log_2M) that the channel can support. We assume our multi-neuron path has additive white Gaussian noise AWGN with root mean square (*rms*) values in the range 5 μV to 10 μV (Guillory and Normann, 1999; Harrison, 2003). This is in accordance with models for neural noise based on experimental microneurographic measurements of normal (as opposed to stimulated) CAPs (Diedrich et al., 2003; Lewicki, 1993). Some models for single neuron AP generation also assume Gaussian noise (Balevi and Akan, 2013) though others propose the addition of some non-Gaussian frequency-dependent noise (Martinez et al., 2009) to provide more accuracy in single-spike capacity and sorting models. Amplitude reduction of the CAP with distance, *z*, will lower SNR and hence reduce maximum channel capacity. The SNR is the ratio between CAP power and noise power and is derived from the *root mean square (rms)* noise level, σ_n, and the rms amplitude of the CAP, $A_{kz}/\sqrt{2}$ (5.13) as follows:

$$
\begin{aligned}
SNR(z) &= \frac{A_k(z)^2}{2\sigma_n{}^2} \\
&= \frac{(G_k e^{-\alpha_k z})^2}{2\sigma_n{}^2}.
\end{aligned}
\tag{5.16}
$$

The SNR is a simple ratio but it can also be expressed in decibels (*dB*) as follows:

$$SNR_{dB}(z) = 10log_{10}\left(\frac{(G_k e^{-\alpha_k z})^2}{2\sigma_n{}^2}\right).$$ (5.17)

The SNR decreases with both distance, as a result of amplitude reduction, and with increasing noise level. In order to compare different modulation methods a normalised form of SNR is calculated to give a ratio of energy per bit, E_b and a noise per hertz, N_0. This is calculated as follows:

$$\frac{E_b}{N_0} = \frac{(SNR)B}{f_b},$$ (5.18)

where B is the bandwidth in Hertz and f_b is the channel data rate.

5.3.1 Channel Capacity

The maximum possible theoretical capacity, C bit/s, of a noisy channel with bandwidth U is given by Shannon's formula (Shannon, 1949):

$$C = Ulog_2(1 + SNR).$$ (5.19)

In this case the bandwidth will be the symbol rate, S_{cap}, divided by 2 (Freeman, 1998). Substituting (5.14), (5.15) and (5.16) we get :

$$C_{cap}(z) = \begin{cases} \frac{1}{2T_{ref}}log_2\left(1 + \frac{(G_k e^{-\alpha_k z})^2}{2\sigma_n{}^2}\right), \\ \qquad\qquad if\ T_{ref} \geq \frac{1}{4\sigma_{cap}} \\ \frac{1}{4(D_{\bar{d}}\sigma_d z + 0.425)}log_2\left(1 + \frac{(G_k e^{-\alpha_k z})^2}{2\sigma_n{}^2}\right), \\ \qquad\qquad if\ T_{ref} < \frac{1}{4\sigma_{cap}} \end{cases}$$ (5.20)

The equations shows that the unrestricted channel capacity for a nerve or fascicle at any given distance z from the stimulus point depends on:

- the **refractory period** of the neurons, T_{ref};

- the **number** of neurons k and the **mean diameter** (determining the CAP amplitude);

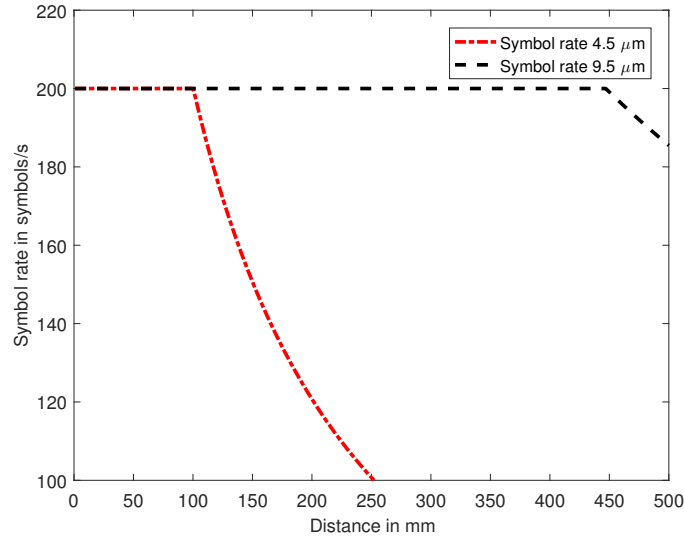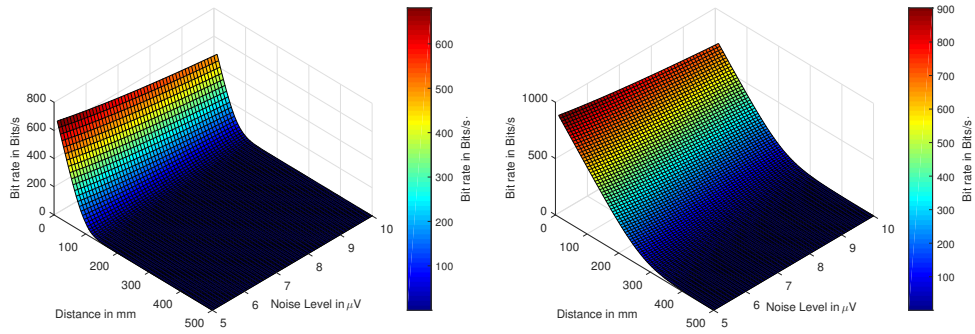(a) Channel capacity CAP (4.5 μm) .   (b) Channel capacity CAP (9.5 μm).

Fig. 5.9 Capacity plots for (a) CAP of 6000 neurons with a mean diameter of 4.5 μm and (b) a CAP of 4000 neurons with a mean diameter of 9.5 μm.

- the background **neural noise level** (σ_n;)

- the **spread of neuron diameters** around the mean value (σ_d);

- the **dispersion** of the mean neuron diameter ($D_{\bar{d}}$).

The Shannon calculation can be applied to our neural channel as it can be modelled as a transmission system with bandwidth 100 Hz and AWGN. However the following conditions will apply:

- The calculation does not define the type or types of modulation (symbols and bits per symbol) that may be needed to achieve this theoretical bit rate.

- There is a ceiling symbol-rate of 200/s.

- The capacity will be greater than or equal to 200 bit/s as long as the SNR is greater than or equal to 3 (4.77 dB).

The plots in Fig. 5.9 are based on (5.20) and show the maximum possible bit rates without the refractory period limit. The number of symbols for a capacity C can be calculated using the Nyquist formula:

$$C = 2U log_2 M \tag{5.21}$$

where U is the bandwidth, M is the number of symbols and $log_2 M$ represents the number of bits per symbol. Symbols can be generated using different modulation techniques (e.g. amplitude or frequency modulation) but the transmission system itself

may limit the options. By equating (5.19) with (5.21) we can show that the number of symbols, M, will depend on the SNR as follows:

$$M = \sqrt{(1 + SNR)}$$
$$= \sqrt{\left(1 + \frac{(G_k e^{-\alpha_k z})^2}{2\sigma_n{}^2}\right)}. \quad (5.22)$$

The higher the SNR, the greater the channel capacity but more symbols must be created to achieve that capacity. The number of bits per symbol, b_s, is:

$$b_s = log_2(M)$$
$$= \frac{1}{2} log_2 \left(1 + \frac{(G_k e^{-\alpha_k z})^2}{2\sigma_n{}^2}\right). \quad (5.23)$$

If there is a limit on the number of symbols that can be employed, there will be a consequent limit on the number of bits per symbol and the result will be a reduced capacity.We now examine what data modulation methods can be applied to these intermittent baseband CAP pulses to compute the attainable bit rate.

5.3.2   Modulation Methods

The amplitude of a CAP will depend on the number of neurons that are activated and is subject to statistical variation. It would be difficult to encode information using stepped amplitude levels so pulse amplitude modulation (PAM) is not considered. The width of a CAP is also subject to some statistical variation and cannot be varied systematically at source so we do not consider pulse width modulation (PWM). Although a CAP has both positive and negative peaks, these are produced simultaneously and it is not possible to use the positive peak to represent a logic "1" and a negative peak to represent a logic "0" . Consequently the encoding will be *unipolar* using the presence or absence of a pulse to encode information. Three different encoding methods are now discussed.

- **Digital Pulse Interval Modulation** (*DPIM*) uses timed intervals between pulses as symbols in order to transmit a data value. The inter-pulse interval is sub-divided into timeslots and the value (in bits) is determined by the number of timeslots. The detection point must correctly calculate the number of timeslots between pulses in order to avoid data errors.

- **Pulse Position Modulation** (*PPM*) uses the position of a pulse within a fixed time interval to convey symbols repesenting multiple bits. The timed interval could allow, for example, a pulse to occupy one of two positions (1 bit per pulse) or one of four positions (2 bits per pulse) with the interval increasing in length for the greater number of positions.

- **On-off Keying** (*OOK*) would send a voltage pulse to represent a binary "1" and no pulse (for the same time duration as one pulse) to represent a binary "0". This represents two symbols ($M = 2$) with one bit per symbol. There are two variants: (i) unipolar *non-return to zero (NRZ)* where 1 and 0 are of similar duration and unipolar (ii) *return to zero (RTZ)* where each positive pulse (1) returns to a zero level for part of the timed duration.

5.3.3 Digital Pulse Interval Modulation

DPIM has been proposed as a coding system for optical wireless (non-fibre based) communications by Ghassemlooy et al. (1998) who compare DPIM throughput, efficiency and error performance with both OOK and pulse position modulation (*PPM*). Versions of DPIM for super-slow bacterial molecular communications have been proposed by Krishnaswamy et al. (2013) (TEC) and Barros et al. (2014) (*Dynamic Time-Slot Configuration with Silent Communication*). MacKay and McCulloch (1952) explored the throughput that could be achieved in a single neuron using OOK and DPIM and we base our CAP DPIM calculations on their work. In our variant of DPIM coding, one information symbol is represented by a CAP pulse plus the time interval until the next CAP (T_s). A maximum and minimum duration is set on this inter-pulse interval (T_{max}, T_{min}) and it is then sub-divided into timeslots of a set length (Δt). The number of symbols, *M* will be:

$$M = \frac{T_{max} - T_{min}}{\Delta t}. \tag{5.24}$$

The symbol size *n* will vary with T_s and will range between 1 and *M* timeslots. The mean value of T_s, if all *M* values are used equally frequently, will be $\frac{1}{2}(T_{max} + T_{min})$ and the average symbol rate, S_{avg}, will be:

$$S_{avg} = \frac{2}{T_{max} + T_{min}}. \tag{5.25}$$

The number of bits per symbol will be $log_2(M)$. The minimum value, T_{min}, is the total refractory period, T_{ref}. We choose the timeslot length Δt as the minimum time to

Table 5.1 DPIM parameters.

T_{ref} (ms)	Δt (ms)	T_{max} (ms)	Symbols	Bits/symbol	Bits/s	Achievable
5	5	30	4	2	133	Yes
5	2.5	25	6	2.58	206	No
5	1.66	21.66	7	2.8	258	No
5	1.25	20	8	3	300	No

distinguish between two consecutive modelled Gaussian pulses ($4\sigma_{cap}$). Substituting from (5.12) and (5.24) we calculate the average bit rate, B_{avg}, in the absence of noise using the average symbol rate and the number of bits per symbol:

$$
\begin{aligned}
B_{avg} &= \frac{2}{T_{max}+T_{min}} log_2 \left(\frac{T_{max}-T_{min}}{\Delta t} \right) \\
&= \frac{2}{T_{max}+T_{ref}} log_2 \left(\frac{T_{max}-T_{ref}}{4\sigma_{cap}} \right) \\
&= \frac{2}{T_{max}+T_{ref}} log_2 \left(\frac{T_{max}-T_{ref}}{4(D_{\bar{d}}\sigma_d z+0.425)} \right)
\end{aligned}
\tag{5.26}
$$

If we set $T_{max} = a\Delta t$ and $T_{min} = b\Delta t$, partial differentiation with respect to T_{max} shows that the maximum value of a is when:

$$
\frac{a+b}{a-b} = ln(a-b).
\tag{5.27}
$$

The optimum value of T_{max} is found by iteration based on (5.27) once values are assigned to T_{ref} and Δt. The values are shown in Table 5.1. The parameter Δt (ms) increases in value with distance and the number of bits per symbol drops. If we assume binary coding then the number of symbols must be a power of 2 and the number of bits per symbol must be an integer. The only achievable value within the limits set by our model is 4 symbols at 2 bits per symbol as shown in Table 5.1. This results in an average bit rate of 133 bit/s, inferior even to the 200 bit/s refractory limit ceiling. Consequently, we do not consider DPIM suitable for neural data transmission in our model.

5.3.4 Pulse Position Modulation

PPM is used at present in optical communications systems (Ghassemlooy et al., 1998) as an alternative to OOK. Each pulse is a symbol that can represent multiple bits. The

pulse can take a different position in time within a timed symbol interval. In our neural model we are constrained to a pulse-length of 5 ms and the symbol interval will be a multiple of this. The capacity C can be expressed as follows:

$$C = \frac{log_2 M}{M t_p},$$ (5.28)

where M is the number of symbols, $log_2(M)$ is the number of bits per symbol and t_p is the length of a pulse. A pulse can take one of M positions within a symbol interval of $M t_p$. The simplest form of PPM uses two possible pulse positions in a symbol interval of $2t_p$ duration and each pulse of length t_p represents a one-bit symbol (a "1" or a "0") . The advantages of PPM over OOK are in the area of greater power efficiency and easier detection at the receiver (Ghassemlooy et al., 1998). However PPM is not suited to asynchronous transmission as accurate timing has to be maintained over symbol intervals that can be many multiples of pulse lengths (Ghassemlooy et al., 1998). The bit rate is *half* that of OOK as only one bit of information is delivered for every two-pulse interval. This bit-rate reduction also holds for higher order four-symbol (two bits per pulse) or eight-symbol (three bits per pulse) PPM systems. We wish to maximise the bit rate of our neural transmission system so we will not use PPM.

5.3.5   On-off Keying

The OOK bit rate is the same as the symbol rate and is a maximum of 200 bits/s. This rate can be sustained until either (i) the SNR drops below 4.77 dB or (ii) pulse broadening changes the symbol rate. The crossover point for pulse broadening has been illustrated in Fig 5.8. The reduction in OOK bit rate caused by a falling SNR, based on (5.20) and with a ceiling of 200 bit/s, is plotted in Fig. 5.10. Our results show that CAP amplitude reduction and SNR have a much greater effect on reducing the OOK 200 bit/s transmission distance than pulse broadening (Fig. 5.10).

5.4   Summary

The neural serial communications channel, described in this chapter, uses CAPs as data pulses to communicate with a receiver placed further along the nerve. The maximum achievable range between transmitter and receiver depends critically on the on the number and diameters of the activated neurons (contributing to the CAP amplitude and width) and the level of background neural noise. These values and parameters allow us to calculate the resulting bit rate at different distances from the stimulus point. It would
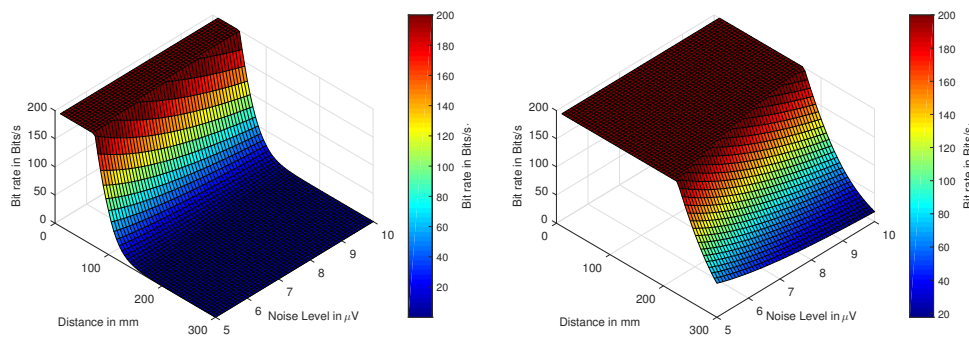
(a) OOK bit rate for CAP of 4.5 μm.   (b) OOK bit rate for CAP of 9.5 μm.

Fig. 5.10 OOK bit rates for (a) CAP of 6000 neurons with a mean diameter of 4.5 μm and (b) a CAP of 4000 neurons with a mean diameter of 9.5 μm.

be possible to improve on the transmission range by increasing the intensity of the applied stimulus and creating a CAP of higher amplitude, but only if not all available neurons of larger diameter had been activated. If all larger diameter neurons have been activated then any further increase in the applied stimulus intensity will trigger smaller diameter, lower velocity neurons resulting in a greater broadening of the CAP without necessarily increasing the amplitude (as shown previously in Fig 5.5b).

Of the three modulation methods analysed, OOK, PPM and DPIM, the only feasible method is OOK given the lower bit-rate of PPM and the timing constraints imposed by the neural channel on the DPIM inter-pulse interval. The OOK bit rate is limited by the refractory period of the neurons and results in a maximum data rate of 200 bits/s. Transmission ranges of over 100 mm at this rate can be achieved at higher levels of SNR. Preliminary calibration of the transmission array would be necessary in order to estimate the CAP width and intensity (amplitude) at different points along the nerve before the placement of the receiving module. The calibration would provide the operating parameters needed to determine the achievable range of the maximum bit rate. The detection of the CAP pulse using a cuff electrode, signal amplification and pulse thresholding is described in more detail in the next chapter (§6.4.1).

Chapter 6

Drug-delivery to the Brain

6.1 Introduction

We now model a specific scenario: the use of neural data pulses transmitted along the vagus nerve, to communicate with a programmable drug-delivery system in the brain as shown in Fig. 6.1. Asynchronous data packets composed of neural pulses can deliver instructions to an embedded device using a unidirectional neural transmission system. Detecting neural data pulses requires lower power than receiving wireless EM signals. Unidirectional transmission implies that no acknowledgement or resend messages can be sent in the reverse direction. We, therefore, analyse the use of *forward error correction (FEC)* in the receiver. We also assess the possibility of using glucose harvesting for powering for the implant.

6.2 Vagus Nerve

The vagus nerve is a cranial nerve extending from the stem of the brain and branching to different organs in the abdomen. It carries neuronal signals to moderate functions such as heart rate, breathing and rate of digestion. Two main branches, the left and the right, can be accessed either side of the neck. The left branch of the vagus nerve, where vagus nerve stimulation (VNS) electrodes are normally placed in humans, does not include cardiac branches with motor neurons and so does not cause cardiac side effects. The main side effects are hoarseness, cough or shortness of breath (Krahl, 2012), with no interference to normal brain function (Howland, 2014).

The neural stimulus system delivers current pulses (> 0.2mA) comparable to those delivered by FDA-approved VNS systems (0.2 mA to 5 mA). The fascicles of the vagus nerve contain both myelinated and unmyelinated axons (Pereyra et al., 1992) usually in
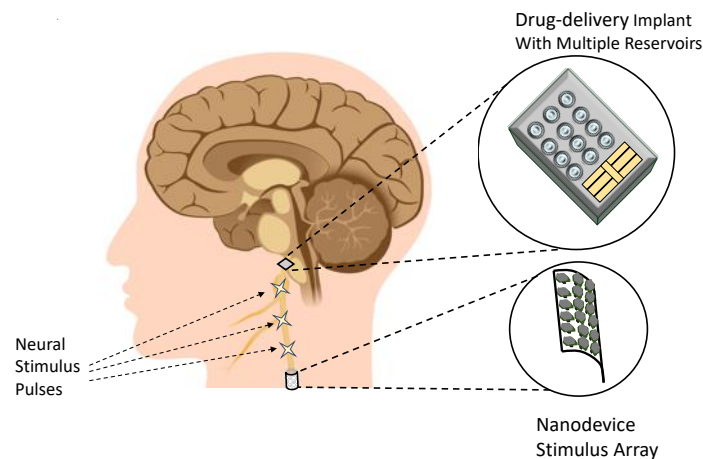
Fig. 6.1 Vagus nerve transmission path delivering data pulses from the stimulus array to the embedded drug-delivery system.

Table 6.1 Vagus Nerve Axons in Left Branch

Axon Type	Diameter (μm)	Average Number
Aβ	9-12	825
Aβ, Aδ	3-9	2475
Aδ	1-3	13200

the proportion of 20% "efferent" fibers (sending signals from the brain to the body) and 80% "afferent" (sensory) fibers (carrying information from the body to the brain) (Howland, 2014). The vast majority are small unmyelinated visceral sensory neurons which carry information from the stomach, intestines, liver, pancreas, and spleen. These are not activated by VNS and would not be activiated by our neural stimulus system. In an adult there can be an average of 16,500 myelinated axons in the left branch and 20,000 in the right branch (Schnitzlein et al., 1958). The diameter of the myelinated axons varies with 80% less than 3 μm, 15% between 3 μm and 9 μm and 5% greater than 9 μm. The distribution of myelinated axons in the left branch of the vagus nerve, derived in (Schnitzlein et al., 1958), is shown in Table 6.1. We use a random distribution of 3300 larger diameter axons (3 μm to 12 μm) as input to (5.6) to generate vagus nerve CAPs as shown in Fig. 6.2.

The left vagus nerve is located at a depth of 2-3 cm from the side of the neck. This makes it surgically accessible for placing an ultrasound harvesting array and stimulating electrode. A stimulus applied at the neck could travel either to the brain or to the abdomen. If directed towards the abdomen, the stimulus would get distributed over all subsequent branches of the nerve and it wouldn't be possible to target a specific
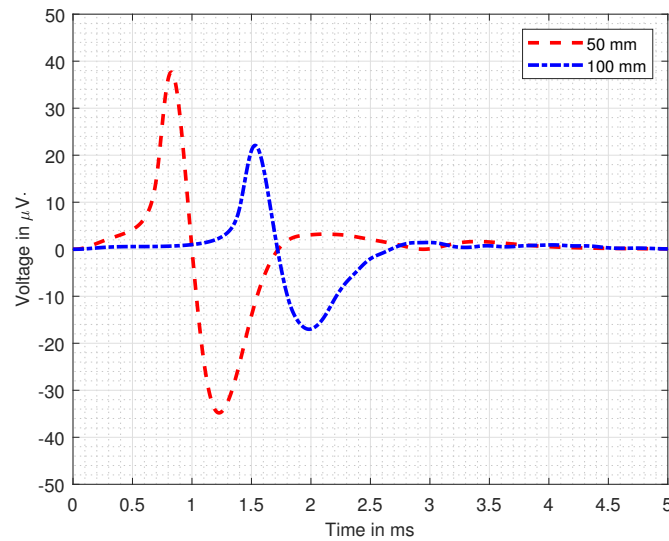
Fig. 6.2 Vagus nerve CAP showing amplitude reduction at two different measuring distances.

organ like the heart. The nerve branches towards the abdomen also (i) have fewer myelinated axons than the main nerve and (ii) traverse a greater distance from neck to abdominal locations than from neck to brain stem. Consequently a CAP to any abdominal location will have lower initial intensity (fewer axons) and experience greater attenuation (longer distance) than a CAP to the brain. We therefore will consider only the higher intensity CAPs that can be directed towards the brain stem along the main vagus nerve. At present, electrodes used for VNS are placed at a point on the neck that is equidistant between the clavicle (collar bone) and the base of the skull. This is equivalent to a point half way along the cervical spinal section. In an adult the cervical spinal sections have a total approximate length of 12 cm (Busscher et al., 2010) so our stimulus array will be placed at least 60 mm from the base of the skull and the brain stem (Fig. 6.1). A stimulus applied at the neck could travel to the brain and be detected by a receiver. In our model we will use a maximum range of 100 mm to allow for physiological variation in the distance from the stimulus array in the neck to the brain stem. Our modelled vagus nerve CAPs are similar in amplitude to therapeutic stimulus CAPs (Evans et al., 2004). A typical epilepsy treatment stimulus cycle is 30 s on and 5 minutes off (Krahl, 2012) applied continuously throughout the day. The CAP data pulse stream will have a much shorter time span (ms) than VNS and this should help minimise the possibility of side effects.

6.2.1 Channel Capacity

We computed the channel capacity of a typical peripheral nerve (sural nerve) in §5.3 taking into account (i) CAP attenuation with distance, (ii) the ceiling imposed by the refractory period and (iii) the background normal neural activity. We now calculate the channel capacity of our modelled vagus nerve and compute the transmission range, subject to these constraints. The CAP attenuation is modelled as a reduction in mean amplitude, $A(z)$, using an empirical exponential function as follows:

$$A(z) = G_v e^{-\alpha_v z}. \tag{6.1}$$

The empirical parameters G_v and α_v have values that depend on the distribution of axon diameters and the number of activated neurons in the vagus nerve. Normal background neural activity is modelled as AWGN with root mean square (*rms*) values in the range 5 μV to 10 μV (Harrison, 2003). The maximum possible capacity, C bit/s, of a noisy channel with bandwidth U is given by Shannon's formula :

$$C = U log_2(1 + SNR). \tag{6.2}$$

The SNR is the ratio between CAP power and noise power and is derived from the *root mean square (rms)* noise level, σ_n, and the rms amplitude of the CAP, $A(z)/\sqrt{2}$ (6.1), as follows:

$$
\begin{aligned}
SNR(z) &= \frac{A(z)^2}{2\sigma_n{}^2} \\
&= \frac{(G_v e^{-\alpha_v z})^2}{2\sigma_n{}^2}.
\end{aligned}
\tag{6.3}
$$

The SNR will decrease with distance, because of reduced CAP amplitude, and with higher background noise levels as shown in Fig. 6.3. A capacity plot for the vagus nerve, derived from (6.2) and (6.3) using a Nyquist bandwidth of 100 Hz (Freeman, 1998) is also shown in Fig. 6.3. The capacity ceiling of 200 bit/s can be achieved as long as the SNR is greater than or equal to 3 (equivalent to 4.77 dB). The SNR values at a range of 100 mm are 11 dB (5 μV) and 5 dB (10 μV) so a capacity of 200 bit/s is possible over all noise levels at all ranges up to 100 mm. We can also calculate the normalised SNR, E_b / N_0, from (6.3) and (5.18) using a bandwidth, B, of 100 Hz and a channel data rate, f_b, of 200 bit/s :

$$\frac{E_b}{N_0} = \frac{A(z)^2 B}{2\sigma_n{}^2 f_b} = \frac{(G_v e^{-\alpha_v z})^2}{4\sigma_n{}^2}. \tag{6.4}$$
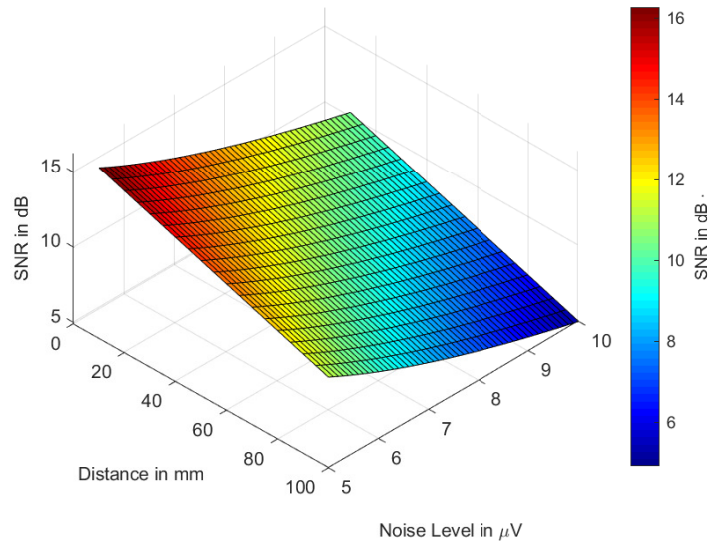
Fig. 6.3 SNR for vagus nerve CAP.

6.2.2 Metabolic Energy Requirements

A conventional EM wireless transmission system can increase the transmission range by increasing the signal power and hence improving the SNR. A wired transmission system can increase the range through the use of regenerators to re-shape and amplify digital signals. Our neural transmission system has elements of both wireless and wired behaviour in that APs are regenerated at each node of Ranvier but the overall CAP is attenuated because of interaction between the APs. The CAP reaches maximum initial amplitude when all larger diameter neurons are activated. A further increase in stimulus energy will trigger lower diameter neurons with slower AP velocities and this will in fact cause greater CAP spreading and a more rapid reduction in amplitude (as shown in §5.2.2).

The metabolic energy needed to create the electrical energy of a CAP can be calculated from the amount of ATP that must be hydrolised to support APs. During the transmission of an AP, ATP molecules provide energy to sodium and potassium pumps in the neuron membrane at *every* node of Ranvier to return the neuron to the resting state. The total CAP transmission energy along a specific range in terms of ATP, E_{CAP}, can be calculated as follows:

$$E_{CAP} = \frac{Nl}{g} m E_{AP},$$

(6.5)

where the number of activated neurons is N, the length of the neural transmission path is l, the distance between nodes of Ranvier is g (typically 2 mm), the number of ATP

78
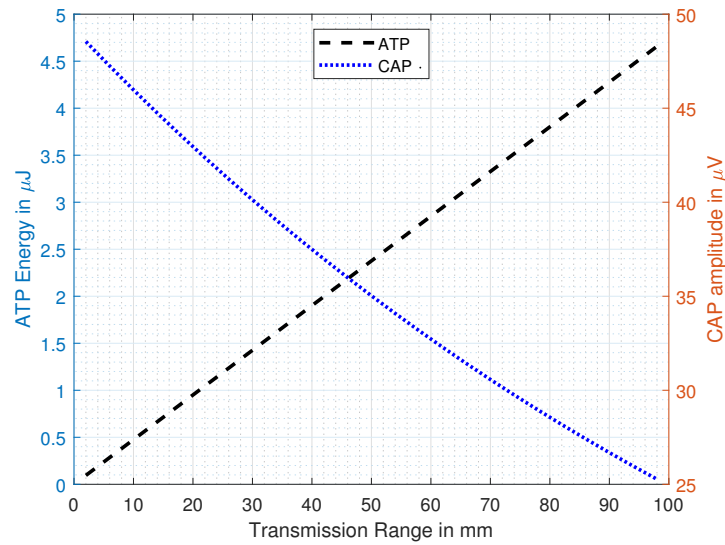
Fig. 6.4 Vagus nerve CAP increase in ATP energy level requirement and decrease in electrical amplitude with distance.

molecules required per AP at each node of Ranvier is *m* and the energy released per ATP molecule is E_{AP}. The ATP hydrolysis energy is about 30.6 kJ/mol or 5 zJ per molecule (Cole, 2016). The energy per molecule is often expressed as approximately $12k_B T$ where k_B is Boltzmann's constant and T is the absolute operating temperature. The number of ATP molecules per AP, per node of Ranvier, is estimated to be a minimum of 10^6 (Aiello and y Rita, 2000). Other studies show ranges from 400 to 800×10^6 (Hallermann et al., 2012) and we will use an average of 600×10^6 molecules of ATP.

A plot of ATP energy requirements for a vagus nerve CAP against transmission range is shown in Fig. 6.4. The ATP energy requirement is linear and directly proportional to the transmission range (46 nJ/mm). The plot also shows the decrease in CAP amplitude (voltage) over the same range based on (6.1). The total number of ATP molecules needed to support a CAP for a range of 100 mm is approximately 98×10^{12}. This is a small fraction of the estimated total daily use of 2×10^{26} transient molecules of ATP in the human body (Cole, 2016).

6.3   Neural Data Link Protocol

The modelled neural CAP communications channel is serial, unidirectional, low bit-rate and therefore suitable for asynchronous transmission, where the sender and receiver have separate clocks. Asynchronous data link messages (packets) are of short

79

duration to ensure that the clocks remain closely timed to each other. A packet usually consists of a start-bit, a character coded as pulses (typically an 8-bit byte) and a stop-bit. Such a packet would have a length of 10 bits and a transmission time of 50 ms with an overhead-to-data ratio of 2/8 or 25%. The send and receive clocks are both based on the expected bit rate and can differ by up to 5% without mis-interpreting the last bit of a ten-bit sequence.

The data packet will deliver instructions to an embedded multi-reservoir drug-delivery system. This can supply repeated doses of either same drug or a selection of different drugs but is likely to be serially activated one reservoir at a time. In our model, a single packet could contain, for example, a two-bit release command and up to six bits of address information (maximum 64 reservoir locations). The number of reservoirs will determine the actual number of addresses so the packet could be shorter than 8 bits if there are fewer than 64 reservoirs. Alternatively a wide range of stored programmes could be activated using an 8-bit command or smaller, though these would all be pre-set with associated addresses and with no scope for customisation.

6.3.1 Forward Error Correction

A unidirectional system has no return path for requesting the re-sending of a faulty packet. Error detection and correction, if required, must therefore be provided within the packet and the receiver. An additional parity bit, or check bit, can be used to check that the correct number of "1" values has been received but it can not specify the location of, or change, a faulty data value. There are other methods for forward error correction *(FEC)* that can locate and correct faulty bits.

Code repetition is a technique where each bit in a packet of length *g* bits is sent $n = 2t + 1$ times, $t \geq 1$. The receiver decodes the group of *n* into the single value that occurs most often. This will correct up to *t* errors and will extend the total packet length to $gn + 2$ bits (including the start/stop bits). The transmission time will increase to $(gn + 2)5$ ms, based on a refractory period of 5 ms. Code repetition is simple to implement but the packet length would cause synchronisation challenges between asynchronous transmitter and receiver. One low bit rate protocol in current use is the unidirectional, asynchronous X10 protocol for addressing and sending commands to simple electrical appliances (e.g. lights) over in-house power lines Cruzl et al. (2008). The highest possible transmission rate is 50 bits/s. The protocol transmits a four bit start-code (1 1 1 0), a four bit "house code" device address followed by a "unit code" (five bits ending in "0") or a device command (five bits ending in "1"). All messages in X10 are transmitted twice to guarantee delivery as there is no acknowledgement

possible from the receiver. Other types of code add fewer extra bits to the packet and these are now discussed.

Block codes add additional parity bits to a byte using a particular algorithm to form a codeword (MacWilliams and Sloane, 1977). Decoding and correction is carried out by comparing the received codeword with stored standard generated codewords and finding the closest match. Block codes can be classed as *linear* or *cyclical* and include Hamming linear codes, Golay binary code, Bose-Chaudhuri-Hocquenghem *(BCH)* cyclic codes, Reed-Solomon *(RS)* cyclic codes and Turbo Product codes. Convolutional codes use more complex encoding and decoding methods on data streams rather than blocks. They use previous bits to encode or decode following bits and hence have memory, unlike block codes that are memoryless. We will model the use of Hamming, Golay and BCH coding on our neural transmission system to study the effect of multiple error detection and correction.

The block code parameters of BCH can be generated from integers $m \geq 3$ and $t < 2^{m-1}$ as follows:

- Codeword length is $n = 2^m - 1$.

- The number of data bits is $k \geq n - mt$ and the number of added parity bits is $n - k \leq mt$.

- The number of errors that can be corrected is t.

- Minimum Hamming distance, $d_{min} \geq 2t + 1$, is a measure of the difference between a received codeword and the closest stored codeword.

- The number of errors that can be detected is $d_{min} - 1$.

Hamming codes are a subset of BCH codes with set values $d_{min} = 3$ and $t = 1$. They can detect two errors and correct one error Ahmadpour et al. (2009). Block codes are often expressed in the form (n, k) or (n, k, d_{min}). Table 6.2 shows examples of the maximum data payload and correction potential in bits for particular Hamming, Golay and BCH codes. Hamming (7 4 3) and BCH (15 5 7) codes are for the shortest packets (4 and 5 bits respectively) and we will not use these. We are interested in modelling those codes that can be used for a data payload of 7 or 8 bits and can correct 1, 2 or 3 errors. These are Hamming (15 11 3), BCH (15 7 5) and Golay (23 12 7).

6.3.2 Error Correction Overhead

The more errors an FEC can correct, the greater the cost in additional processing load, longer packets and increased transmission time. With a Hamming (15 11 3) code the

Table 6.2 Error Correction Codes

Code	Data Bits (max.)	Parity Bits	Correction Potential (bits)
Hamming(15 11 3)	11	4	1
BCH(15 7 5)	7	8	2
BCH(15 5 7)	5	10	3
BCH(31 21 5)	21	10	2
Golay(23 12 7)	12	11	3
BCH(31 16 7)	16	15	3

minimum number of additional error correction bits for an 8-bit data message is 4 bits and the total packet length (including start and stop bits) is 14 bits. The overhead to data ratio is 6/8 or 75% and the packet will have a transmission time of at least 70 ms. The BCH (15 7 5) and Golay (23 12 7) have overhead to data ratios of 142% and 162.5% with transmission times of 85 ms and 105 ms. The larger overall packet size could increase the probability of a loss of synchronisation between the sender and receiver clocks.

The additional FEC overhead implies that an additional 46 nJ/mm of ATP is needed for each parity bit. A Hamming (15 11 3) code would require an additional 184 nJ/mm of ATP along the neural transmission path. The BCH (31 21 5) and Golay (23 12 7) coding would require additional levels of 460 nJ/mm and 506 nJ/mm respectively. We now examine the gain provided by the different FEC coding methods.

6.3.3 Coding Gain

The *coding gain* of an FEC is the effective improvement in *bit error rate (BER)* resulting from the use of a particular code on a noisy communications channel. In order to compute the gain we must first compute the uncoded BER for CAP transmission along a vagus nerve that has AWGN. The BER measures the probability of data-detection errors occurring as the SNR decreases and is based on the *complementary error function (erfc)* (Ippolito, 2008), the probability that a "0" is detected instead of a "1" or vice versa. The threshold of detection for unipolar OOK is usually set at $A(z)/2$ for a detection distance z. The erfc is then defined as the *cumulative probability* of detecting a particular value of noise, x, in the range $A(z)/2$ to ∞ as follows:

$$erfc\left(\frac{A(z)}{2}\right) = \int_{A(z)/2}^{\infty} \frac{1}{\sqrt{2\pi}\sigma_n} e^{-x^2/2\sigma_n} dt. \qquad (6.6)$$
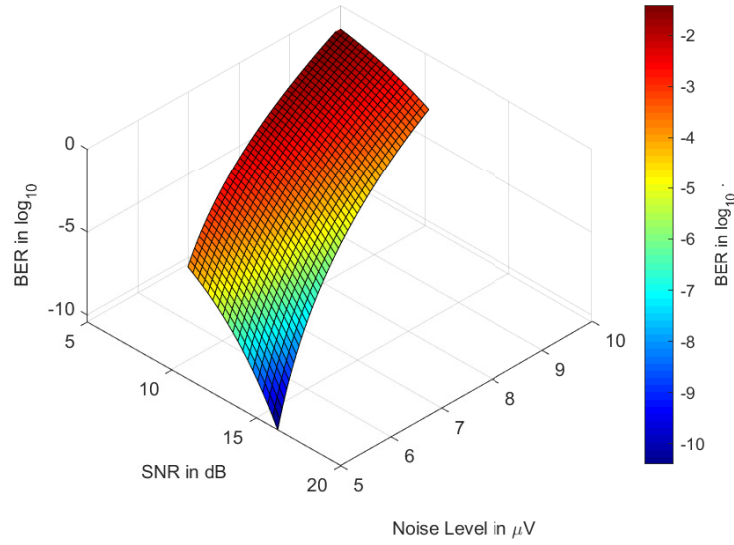
Fig. 6.5 BER for vagus nerve CAP showing increase with noise level and SNR for a data rate of 200 bits/s.

Making a change of variable, $y = x/\sigma_n$ we get the integral:

$$erfc\left(\frac{A(z)}{2\sigma_n}\right) = \int_{A(z)/2\sigma_n}^{\infty} \frac{1}{\sqrt{2\pi}} e^{-y^2/2} dy. \tag{6.7}$$

This can be further refined by making the following change:

$$\frac{A(z)}{2\sigma_n} = \sqrt{\frac{A(z)^2}{4\sigma_n^2}} = \sqrt{\frac{E_b}{N_0}}. \tag{6.8}$$

This allows the erfc to be expressed in terms of E_b/N_0 as shown previously in (6.4). The total probability of bit error for an uncoded OOK stream, BER_{uc}, is calculated as follows:

$$\begin{aligned} BER_{uc} &= \frac{1}{2} erfc\sqrt{\frac{A(z)^2}{4\sigma_n^2}} \\ &= \frac{1}{2} erfc\sqrt{\frac{(G_v e^{-\alpha_v z})^2}{4\sigma_n^2}}. \end{aligned} \tag{6.9}$$

The uncoded BER is shown as a surface plot in Fig. 6.5 across a range of noise levels. The coded BER at the input of the decoder, BER_{id}, is calculated as follows (Goldsmith,

83

2005):

$$BER_{id} = \frac{1}{2} erfc\sqrt{\frac{k}{n}\frac{(G_v e^{-\alpha_v z})^2}{4\sigma_n^2}}, \tag{6.10}$$

where the codeword length is n, the number of data bits is k and the coding rate is k/n. We then use the values of BER_{id} to first calculate the output word error probability, WEP_{od}, as follows:

$$WEP_{od} = \binom{n}{t+1}(BER_{id})^{t+1}(1-BER_{id})^{n-(t+1)}, \tag{6.11}$$

where the expression $\binom{n}{t+1}$ represents the binomial coefficient. The output coded BER, BER_{od} can then be expressed as:

$$BER_{od} = \frac{d_{min}}{n}(WEP_{od}). \tag{6.12}$$

It should be noted that (6.12) is an approximation that becomes less reliable and applicable at very low values of SNR. Higher noise levels can drive the error rate beyond the capability of simple error correction. The coding gain is a measure of the difference in SNR between uncoded and coded systems for the same BER. The BER is normally plotted against SNR in dB but in our model it can also be plotted against transmission range. The BER plot for our neural transmission system between uncoded data, Hamming (15 11 3), BCH (15 7 5) and Golay (23 12 7) coded data, based on (6.12), is shown in Fig. 6.6 for noise levels of 5 μV and 10 μV. The curves show that with FEC (i) a fixed BER can be achieved at a greater range and (ii) a fixed range can have a lower BER.

The plots show that at the lower noise level of 5 μV there is coding gain up to the maximum range of 100 mm. At the higher noise level of 10 μV there is no coding gain after 30 mm range because of the high BER. The coding curves cross over the uncoded curve where the level of errors increases beyond the correction capability of the code (Freeman, 1997). The Hamming (15 11 3) gain can also be expressed in terms of ATP, calculated from the coding gain in mm. This ATP gain must be offset against the extra ATP needed to carry the corresponding 4 parity bits. Levels of ATP Hamming (15 11 3) gain and the corresponding ATP parity bit cost is shown in Table 6.3. In every case the ATP cost is greater than the ATP gain, and the difference increases with range. FEC can produce gains and improvements in performance in our neural transmission model but the benefits are sharply reduced with increasing noise level.
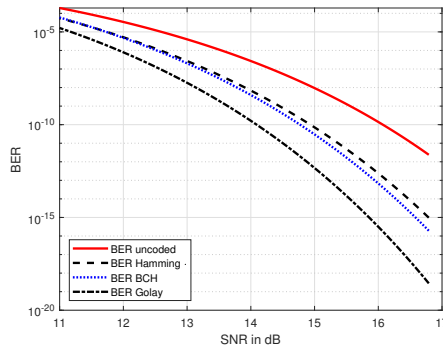
(a) BER and SNR for 5 μV.
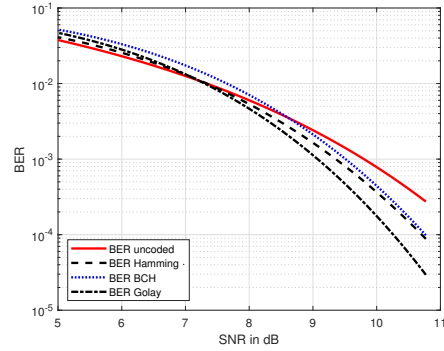
(b) BER and SNR for 10 μV.
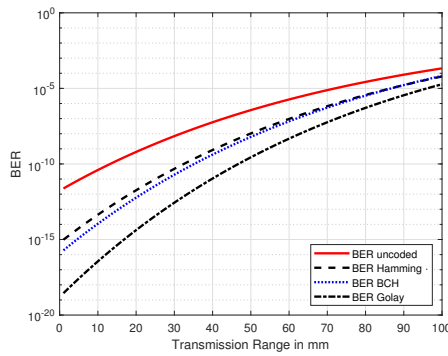
(c) BER and range for 5 μV.
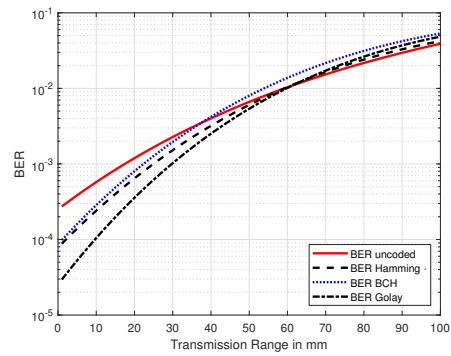
(d) BER and range for 10 μV.

Fig. 6.6 BER plots against SNR and transmission range for three different types of FEC and two levels of noise.

6.4   Drug-delivery System

The embedded drug-delivery system that receives the data packets will have (i) an electrode attached to the nerve to detect the CAP pulse, (ii) an amplification and conversion system to boost the signal power and create a digital bitstream, (iii) a microcontroller unit (MCU) to collect and interpret the bitstream (iv) a drug-release mechanism and (v) a power source sufficient to meet all energy demands.
CAP detection is through a front-end single-channel, single-electrode system similar to those used at present for recording neural activity (Loeb and Peck, 1996). The detected pulses will be in the microvolt range. This low voltage is insufficient to switch a transistor directly with existing complementary metal-oxide-semiconductor (CMOS) technology and must be amplified and analysed before it can be designated a logic "1". The detection and amplification function alone places a minimum requirement on the power needed to operate the receiving system, without considering the follow-on drug-delivery functions.

Table 6.3 ATP Code Gain and Parity Bit Cost

BER	Uncoded mm	Gain mm	ATP Gain nJ	ATP Cost nJ
10^{-10}	13	20	920	2392
10^{-8}	31	19	874	5704
10^{-6}	56	16	736	10304
10^{-4}	90	13	598	16560

(a) CAP with noise level of 5 μV (b) CAP with noise level of 10 μV
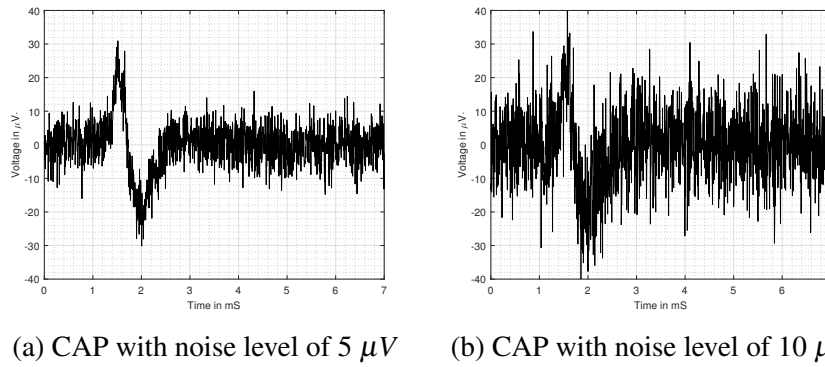
Fig. 6.7 Vagus nerve CAP at a detection range of 100 mm showing the effect of noise.

6.4.1   Detection Electrode and Signal Amplification

The CAP detection electrode must be in close proximity to the transmitting nerve. It may be wrapped around it as a cuff electrode (Yu et al., 2014) and have a tripolar configuration for optimum low-noise measurement (Loeb and Peck, 1996). The length of a tripolar electrode is typically from 15 mm to 30 mm (Andreasen and Struijk, 2002). The low voltage level of the CAP requires that the cuff electrode must be connected to a low-noise preamplifier. The amplified signal can then be sent through filters to a comparator for conversion to logic "1" or "0" using an appropriate sampling rate, and detection threshold set between the noise floor and the expected maximum amplitude. The effect of noise on the CAP waveform at the receiver end is shown in Fig. 6.7. Suitable filters can remove unwanted higher frequency components from the signal as well as having a role in pulse shaping.

Single channel and multi-channel neural amplification and digitalisation is described by Muller et al. (2012) and their system has a power consumption of 5 μW. Other comparable neural amplifier systems are reviewed in (Muller et al., 2012) and the power consumption is also in the low μW range.

6.4.2   Microcontroller Unit and Drug-delivery Function

The MCU would decode the incoming raw bitstream from the comparator and perform any error corrections. The architecture of a comparable MCU is described by Huang et al. (2012) for a drug delivery system. This has a universal asynchronous receiver/transmitter (UART) to convert serial bits into parallel, a clock input for timing and a decoder to format and forward commands. The power consumption of the MCU and clock generator is 10.68 μW.

Electrophoretic drug-delivery, as described by Proctor et al. (2018), applies a voltage difference (typically 1 V) to pump ions from a reservoir across an ion exchange membrane using a *microfluidic ion pump (μFIP)*. The amount of drug delivered depends on the length of time that the voltage is applied. A single type of drug was delivered in trials and the system is being extended for multiple delivery channels that can be singly activated. The operating voltage (1 V) is low and this would indicate a low power requirement. An alternative method, *electrothermal membrane activation*, was first proposed by Santini Jr et al. (1999) for multiple drug-delivery. A metallic membrane covering each drug reservoir is heated by an applied electrical current, the membrane ruptures and the drug reservoir then releases its contents. This release model is used in (Huang et al., 2012) for a fabricated delivery system that has a total volume of approximately 30 mm^3.

A multi-reservoir delivery system can deliver repeated doses of the either same drug or a selection of different drugs but is likely to be serially activated one reservoir at a time. The power dissipated will depend on the specific materials used in the membrane and the maximum values of current and voltage that can be applied. The activation current in Maloney et al. (2005) has a nominal value of 1 A and is applied for 10 μs resulting in an activation energy of 25 μJ. A lower activation current with a maximum value of 45 mA is used in Huang et al. (2012), applied for 100 ms, results in an activation energy of 6.75 mJ. The power level in both cases would be in the milliwatt range. The number of reservoirs will determine the number of addresses. The drug delivery system in (Huang et al., 2012) has eight addressable reservoirs. Drug release is activated by a ten-bit OOK command that consists of start and stop bits, a five bit activation key and a three bit address. The authors state that a more robust forward error correction system would be required in future models.

In our model, a single packet with Hamming (15 11 3) FEC could contain, for example, a two-bit release command, four bits of error correction and six bits of address information (up to 64 reservoir locations) as shown in Fig. 6.8. The addressable

S2	A6	A5	A4	A3	H4	A2	A1	C2	H3	C1	H2	H1	S1

S2 = Stop Bit   A1 – A6 = Address Bits   S1 = Start Bit

C1 – C2 = Command Bits

H1 – H4 = Hamming Correction Bits
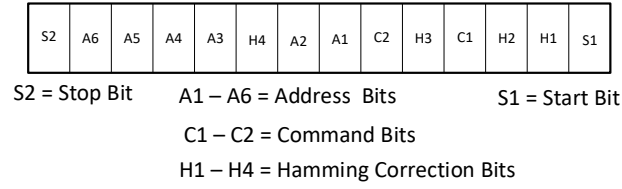
Fig. 6.8 Drug-delivery data packet with command and error correction.

reservoirs could be distributed to different parts of the brain, delivering targetted brain-tumour therapy to locations identified by brain-scans.

6.4.3   Receiver Powering

The electrode, amplification and processor systems will require constant power as they will have to be always-on. The drug delivery function of the implant will have an intermittent and short duration power requirement. At present the power would be delivered by a long-life battery. Biological energy harvesting could provide a biocompatible and long-life method for delivering the necessary power, either directly to the delivery unit or to provide a trickle charge to a rechargeable battery. A fuel cell using glucose from cerebrospinal fluid circulating around the brain is described by Rapoport et al. (2012). The fuel cell has a roughened platinum anode separated from a carbon nanotube cathode by a cation-selective membrane. Glucose is oxidised at the anode while oxygen is reduced to water at the cathode. The efficiency of different types of glucose cells varies from a high of 80% to a low of 8%. The glucose flux J_g in milligrams per second (based on 180 mg of glucose per mole) needed to produce a particular power level P is as follows Rapoport et al. (2012):

$$J_g = \frac{180P}{\eta \Delta G_g} \tag{6.13}$$

where the conversion efficiency is η and the energy released per mole is $\Delta G_g = 2880$ kJ. The flux of glucose, in milligrams per second, needed to produce a range of power levels at different conversion efficiencies based on (6.13) is shown in Fig. 6.9. The amount of glucose per day needed to produce a continuous power level of 10 mW ranges from 67.5 mg to 675 mg depending on the efficiency η. The daily flow of glucose through the cerebral space is between 250 mg and 440 mg., so the production of higher levels of power could have a major impact on the glucose levels of the
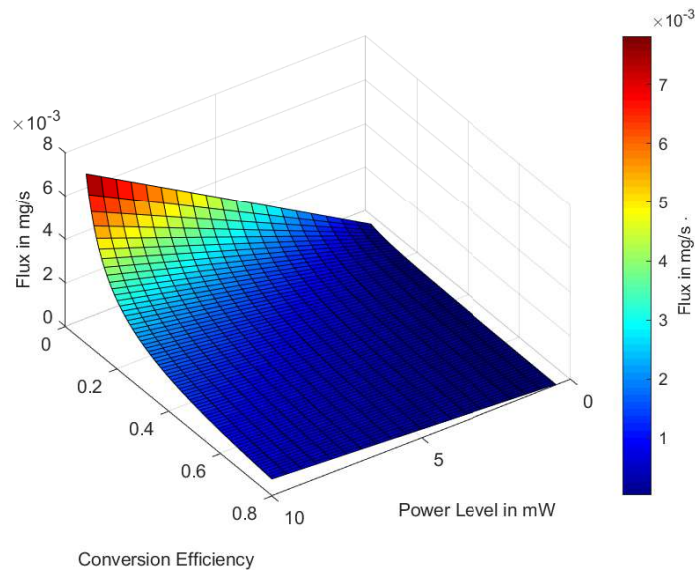
Fig. 6.9 Glucose flux requirement with increase in efficiency and power demand.
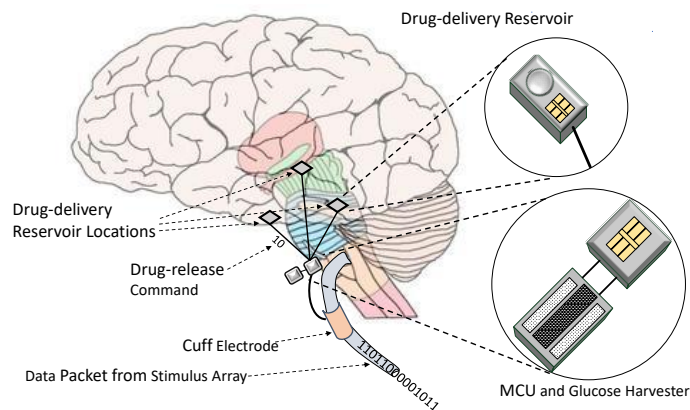
Fig. 6.10 Distributed drug-delivery at multiple locations in the brain.

cerebrospinal fluid especially at low conversion efficiency levels. The Rapoport fuel cell has power density of .034 μW per mm^2 in a steady state and 1.8 μW per mm^2 in a transient state with an open-circuit voltage of 192 mV. A glucose powered drug-delivery system with distributed reservoirs in the brain is shown in Fig. 6.10. Improvements in performance have been demonstrated by Kwon et al. (2018) who developed a hybrid biofuel cell that uses metallic cotton fibre cathode and has a power density of 37 μW per mm^2. Power levels in the microwatt range may be sufficient to power the amplification and MCU components especially if lower-power and lower-voltage electronic technologies emerge, like those described by Theis and Solomon (2010). There would, however, need to be power density into the milliwatt region if drug release using electrothermal membrane activation is to be achieved.

Electrophoretic drug delivery might be a more achievable alternative if the voltage level of a glucose powered system could be boosted to 1 V using a step-up converter of the type described by Jayaweera et al. (2015). Either way, more efficient glucose harvesting systems would be required if a fully self-powering system is to be realised.

6.5   Summary

Using the vagus nerve for the transmission of digital CAP pulses is a variation on existing therapeutic VNS. The left branch of the vagus nerve can be accessed at the neck and is at a shallow enough depth to allow ultrasound pulses to penetrate and activate a neural stimulus array. The stimulus pulses travel towards the brain stem and can be intercepted by a receiving electrode and a drug-delivery system. The maximum OOK bit rate of 200 bit/s is constrained by the neural refractory period. The transmission range is also constrained by CAP attenuation and noise level but would be between 60 mm and 100 mm.

The unidirectional, asynchronous transmission system would use short packets to maintain synchronisation at both ends. With no return path, there is a need to correct data errors and we modelled the use of block codes for FEC to improve the effective range. The addition of extra parity bits increases the total packet length,transmission time and ATP consumption. There are measurable coding gains but these become less significant at greater transmission ranges and lower SNRs. Simple one-byte (8-bit) commands with additional FEC parity bits can activate an embedded drug-delivery system near the brain. The packet transmission time of tens of milliseconds is an acceptable timeframe in relation to the diffusion and absorption time of a drug in brain tissue.

Existing drug delivery implants require power in the milliwatt region and voltage levels of 1 V or greater. At present these requirements are met by long-life batteries. It may also be the case that the drug reservoirs would be exhausted before the battery has expired, depending on the frequency of drug release. The system would have to be removed for replenishment. Alternatively a longer-term slower release programmable system would be better powered by a rechargeable battery that could be trickle-charged through energy harvesting. A slow-release system would be applicable in the management of ongoing chronic conditions. We believe that biological energy harvesting using, for example, glucose in the cerebrospinal fluid would be a preferable biocompatible solution in the longer term for direct powering or trickle-charging. Another potential application would be providing power to a therapeutic microstimulus

system embedded in the brain. There would need to be major improvements in the power density of the harvesting system and reductions in the power and voltage requirement of the implanted device before systems would be feasible.

Chapter 7

Conclusions and Future Work

7.1 Conclusions

Powering and communicating with implanted biomedical devices will continue to be important research topics, especially as the demand for such devices grows. At present, electrical power is usually provided by batteries that may have to be replaced at regular intervals. Communications is either through wired connections or wireless EM systems. Energy harvesting could provide a safe and viable alternative to batteries for delivering power, and some implanted devices already use near-field EM harvesting. A potential harvesting option, ultrasound, is in wide use at present for medical imaging and could also deliver power through human tissue. We have shown how an ultrasound beam could deliver power to arrays of piezoelectric nanowire energy-harvesting devices, stimulating peripheral or cranial nerves in response to modulated ultrasound pulses. This, in turn, provides an alternative biologically-based data communications system along the nerve. The OOK modulated neural pulses would convey short data packets to a deeper embedded implant to trigger specific functions, such as drug-delivery. The neural transmission system is biocompatible, with a maximum data rate of 200 bit/s, and is also unidirectional. A transmission range of 100 mm can be achieved even with higher background noise levels. The receiver detects these pulses through a simple electrode rather than a more power-intensive radio receiver. The coding and decoding process can incorporate forward error correction to improve performance.

A low-power, deeply implanted receiver might not be able to avail of ultrasound harvesting as there would be too much absorption and reflection through the intervening tissue. Ideally another form of energy harvesting, glucose energy harvesting, could be used instead of battery powering to avoid repeated surgical intervention. Energy harvesting and neural data communications are part of the wider

development of bio-inspired solutions for closed-loop communications between implanted miniature devices and external networked systems.

7.2 Future Work

The proposals for future research work are based on the two main topics of this thesis: energy harvesting and neural data communications. The energy supplied to any device is determined by the power requirement, which may be continuous (e.g. sensor) or intermittent (e.g. command delivery). The harvesting method has to be able to supply the power either directly, or through charging an energy storage system (battery or capacitor). The physical size of the harvesting system must also be determined as it may add considerable bulk to an otherwise small device and make implantation more difficult. The harvesting system and the implanted device must be bio-compatible in order to reduce the risk of rejection or inflammation. This would require that the system components should be bio-compatible or encased in a bio-compatible container. Unidirectional neural communications may be suitable for some simple applications but in many cases a return path must be provided in order to provide diagnostic or therapeutic feedback. There are options for realising bidirectional communications, but again these must be modelled and tailored to the specific device application, the uplink and downlink capacities and the physical constraints of the location. Additional harvested power is needed to support a return path and this must be factored in when modelling the harvesting system.

7.2.1 Power Harvesting

Ultrasound energy-harvesting piezoelectric nanowire devices could be used to power other implanted devices such as chemical sensors or communications nodes. In every case the trade-off between ultrasound frequency, device power requirement and physical size must be modelled to test the viability of such solutions. Nanowire-based devices should also be compared to resonant crystal-based alternatives in order to determine the optimum harvesting solution at different tissue depths and in confined physical locations (e.g. inside the skull).

Glucose energy harvesting should also be investigated as a power source, once the function and power requirement of specific types of device have been modelled. The potential flux of glucose at different points in the body needs to be determined as part of this modelling. The physical size of a glucose harvesting system must also be modelled as this would have implications for suitable implantation sites in the body.

7.2.2 Neural Communications

The neural communications system described in this thesis generates one CAP data pulse from all the stimulated fascicles. If individual fascicles in a nerve are stimulated, then this could increase the number of transmitted pulses per second by interleaving CAPs. The nanodevice stimulus array would require some local processing power and multiple electrodes in order to transfer a pattern of ultrasound pulses across multiple fascicles. The receiver would need to have a detection electrode for each fascicle in order to detect the interleaved CAPs. A major challenge in the development of an interleaved CAP model is the minimisation of interference (crosstalk) between adjacent fascicles.

Ideally the neural communications system should be bidirectional, allowing the return transmission of data out of the body to an external processing system. Creating a bidirectional system could be done by (i) having an energy-harvesting stimulus array at both ends of the neural path or (ii) using a different transmission method from the distant node such as molecular communications. An energy harvesting stimulus array at a deeper tissue level could not be powered by ultrasound (because of absorption and reflection) so an alternative method, such as glucose harvesting, would be required. The receiving device function, the power requirement and the projected data throughput would all provide inputs for the modelling and simulation of a truly bidirectional neural transmission system.

Energy harvesting and neural communications are part of the longer-term vision for BANs. Networks of energy-harvesting nanodevices could be established in the skin or in specific organs, such as the heart, in order to detect changes in key chemical concentrations. These networks would then communicate this information to an external monitoring system and receive other external information in return. Once this communication sub-system of the nervous system is interconnected to the Internet this will form part of the vision of a closed-loop, context-aware Internet of Bio-Nano Things (Akyildiz et al., 2015).

Bibliography

Abbasi, N. A., Lafci, D., and Akan, O. B. (2018). Controlled information transfer through an in vivo nervous system. *Scientific Reports*.

Ahmadpour, A., Sha, A. A., and Ziabari, M. (2009). A novel formulation of hamming code. In *2009 6th International Conference on Electrical Engineering/Electronics, Computer, Telecommunications and Information Technology*, volume 02, pages 808–811.

Aiello, G. L. and y Rita, P. B. (2000). The cost of an action potential. *Journal of Neuroscience Methods*, 103(2):145 – 149.

Akyildiz, I., Pierobon, M., Balasubramaniam, S., and Koucheryavy, Y. (2015). The internet of bio-nano things. *IEEE Communications Magazine*, 53(3):32–40.

Akyildiz, I. F., Brunetti, F., and Blázquez, C. (2008). Nanonetworks: A new communication paradigm. *Computer Networks (Elsevier)*, 52(12):2260–2279.

Altman, K. W. and Plonsey, R. (1990). Point source nerve bundle stimulation: effects of fiber diameter and depth on simulated excitation. *IEEE Transactions on Biomedical Engineering*, 37(7):688–698.

Amon, A. and Alesch, F. (2017). Systems for deep brain stimulation: review of technical features. *Journal of Neural Transmission*, 124(9):1083–1091.

Andreasen, L. N. S. and Struijk, J. J. (2002). Signal strength versus cuff length in nerve cuff electrode recordings. *IEEE Transactions on Biomedical Engineering*, 49(9):1045–1050.

Andreu-Perez, J., Leff, D., Ip, H., and Yang, G.-Z. (2015). From wearable sensors to smart implants- toward pervasive and personalized healthcare. *IEEE Transactions on Biomedical Engineering*, 62(12):2750–2762.

Apollo, N. V., Maturana, M. I., Tong, W., Nayagam, D. A. X., Shivdasani, M. N., Foroughi, J., Wallace, G. G., Prawer, S., Ibbotson, M. R., and Garrett, D. J. (2015). Soft, flexible freestanding neural stimulation and recording electrodes fabricated from reduced graphene oxide. *Advanced Functional Materials*, 25(23):3551–3559.

Atakan, B., Akan, O. B., and Balasubramaniam, S. (2012). Body area nanonetworks with molecular communications in nanomedicine. *IEEE Communications Magazine*, 50(1):28–34.

Balevi, E. and Akan, O. B. (2013). A physical channel model for nanoscale neuro-spike communications. *IEEE Transactions on Communications*, 61(3):1178–1187.

95

Barros, M. T., Balasubramaniam, S., Jennings, B., and Koucheryavy, Y. (2014). Transmission protocols for calcium-signaling-based molecular communications in deformable cellular tissue. *IEEE Transactions on Nanotechnology*, 13(4):779–788.

BeMent, S. L. and Jr., J. B. R. (1969). A model for electrcal stimulation of central myelinated fibers with monopolar electrodes. *Experimental Neurology*, 24(2):171 – 186.

Berger, T. W., Song, D., Chan, R. H. M., Marmarelis, V. Z., LaCoss, J., Wills, J., Hampson, R. E., Deadwyler, S. A., and Granacki, J. J. (2012). A hippocampal cognitive prosthesis: Multi-input, multi-output nonlinear modeling and vlsi implementation. *IEEE Transactions on Neural Systems and Rehabilitation Engineering*, 20(2):198–211.

Berrou, C., Glavieux, A., and Thitimajshima, P. (1993). Near shannon limit error-correcting coding and decoding: Turbo-codes. 1. In *Proceedings of ICC '93 - IEEE International Conference on Communications*, volume 2, pages 1064–1070 vol.2.

Bertrand, A., Seo, D., Maksimovic, F., Carmena, J., Maharbiz, M., Alon, E., and Rabaey, J. (2014). Beamforming approaches for untethered, ultrasonic neural dust motes for cortical recording: A simulation study. In *36th Annual International Conference of the IEEE Engineering in Medicine and Biology Society (EMBC), 2014*, pages 2625–2628.

Bicen, A. O. and Akyildiz, I. F. (2014). End-to-end propagation noise and memory analysis for molecular communication over microfluidic channels. *IEEE Transactions on Communications*, 62(7):2432–2443.

Bicen, A. O. and Akyildiz, I. F. (2015). Interference modeling and capacity analysis for microfluidic molecular communication channels. *IEEE Transactions on Nanotechnology*, 14(3):570–579.

Bicen, A. O., Lehtomäki, J. J., and Akyildiz, I. F. (2018). Shannon meets fick on the microfluidic channel: Diffusion limit to sum broadcast capacity for molecular communication. *IEEE Transactions on NanoBioscience*, 17(1):88–94.

Bihr, U., Liu, T., and Ortmanns, M. (2014). Telemetry for implantable medical devices: Part 3 - data telemetry. *IEEE Solid-State Circuits Magazine*, 6(4):56–62.

Bock, D. C., Marschilok, A. C., Takeuchi, K. J., and Takeuchi, E. S. (2012). Batteries used to power implantable biomedical devices. *Electrochimica Acta*, 84:155 – 164.

Bose, R. and Ray-Chaudhuri, D. (1960). On a class of error correcting binary group codes. *Information and Control*, 3(1):68 – 79.

Brocker, D. T. and Grill, W. M. (2013). Chapter 1 - principles of electrical stimulation of neural tissue. In Lozano, A. M. and Hallett, M., editors, *Brain Stimulation*, volume 116 of *Handbook of Clinical Neurology*, pages 3 – 18. Elsevier.

Browning, K. N., Verheijden, S., and Boeckxstaens, G. E. (2017). The vagus nerve in appetite regulation, mood, and intestinal inflammation. *Gastroenterology*, 152(4):730 – 744.

Busscher, I., Ploegmakers, J. J., Verkerke, G. J., and Veldhuizen, A. G. (2010). Comparative anatomical dimensions of the complete human and porcine spine. *European Spine Journal*, 19(7):1104–1114.

Cacciapuoti, A. S., Piras, A., and Caleffi, M. (2016). Modeling the dynamic processing of the presynaptic terminals for intrabody nanonetworks. *IEEE Transactions on Communications*, 64(4):1636–1645.

Capogrosso, M., Milekovic, T., Borton, D., Wagner, F., Moraud, E. M., Mignardot, J.-B., Buse, N., Gandar, J., Barraud, Q., Xing, D., Rey, E., Duis, S., Jianzhong, Y., Ko, W. K. D., Li, Q., Detemple, P., Denison, T., Micera, S., Bezard, E., Bloch, J., and Courtine, G. (2016). A brain -spine interface alleviating gait deficits after spinal cord injury in primates. *Nature*, 539(7628):284–288.

Cartee, L. A. and Plonsey, R. (1992). The transient subthreshold response of spherical and cylindrical cell models to extracellular stimulation. *IEEE Transactions on Biomedical Engineering*, 39(1):76–85.

Chahibi, Y. and Akyildiz, I. F. (2014). Molecular communication noise and capacity analysis for particulate drug delivery systems. *IEEE Transactions on Communications*, 62(11):3891–3903.

Chahibi, Y., Akyildiz, I. F., and Balasingham, I. (2016). Propagation modeling and analysis of molecular motors in molecular communication. *IEEE Transactions on NanoBioscience*, 15(8):917–927.

Chahibi, Y., Akyildiz, I. F., Balasubramaniam, S., and Koucheryavy, Y. (2015). Molecular communication modeling of antibody-mediated drug delivery systems. *IEEE Transactions on Biomedical Engineering*, 62(7):1683–1695.

Charthad, J., Baltsavias, S., Samanta, D., Chang, T. C., Weber, M. J., Hosseini-Nassab, N., Zare, R. N., and Arbabian, A. (2016). An ultrasonically powered implantable device for targeted drug delivery. In *2016 38th Annual International Conference of the IEEE Engineering in Medicine and Biology Society (EMBC)*, pages 541–544.

Charthad, J., Chang, T. C., Liu, Z., Sawaby, A., Weber, M. J., Baker, S., Gore, F., Felt, S. A., and Arbabian, A. (2018). A mm-sized wireless implantable device for electrical stimulation of peripheral nerves. *IEEE Transactions on Biomedical Circuits and Systems*, 12(2):257–270.

Charthad, J., Weber, M. J., Chang, T. C., and Arbabian, A. (2015). A mm-sized implantable medical device (imd) with ultrasonic power transfer and a hybrid bi-directional data link. *IEEE Journal of Solid-State Circuits*, 50(8):1741–1753.

Chude-Okonkwo, U. A. K., Malekian, R., Maharaj, B. T., and Vasilakos, A. V. (2017). Molecular communication and nanonetwork for targeted drug delivery: A survey. *IEEE Communications Surveys Tutorials*, 19(4):3046–3096.

Clapham, D. E. (2007). Calcium signaling. *Cell*, 131(6):1047 – 1058.

Cogan, S. F. (2008). Neural stimulation and recording electrodes. *Annual Review of Biomedical Engineering*, 10(1):275–309. PMID: 18429704.

Cogan, S. F., Ludwig, K. A., Welle, C. G., and Takmakov, P. (2016). Tissue damage thresholds during therapeutic electrical stimulation. *Journal of Neural Engineering*, 13(2):021001.

Cole, L. A. (2016). Chapter 10 - adenosine triphosphate energetics. In Cole, L. A., editor, *Biology of Life*, pages 65 – 77. Academic Press.

Cosnier, S., Goff, A. L., and Holzinger, M. (2014). Towards glucose biofuel cells implanted in human body for powering artificial organs: Review. *Electrochemistry Communications*, 38:19 – 23.

Cruzl, M. D., Ortegal, J. A., Barriga, Á., and Fernández-Montes, A. (2008). Development environment using fpga for domotics applications based on x10 technology. In Sobh, T., Elleithy, K., Mahmood, A., and Karim, M. A., editors, *Novel Algorithms and Techniques In Telecommunications, Automation and Industrial Electronics*, pages 150–153, Dordrecht. Springer Netherlands.

Dambrot, S. M. (2017). Enplants: Genomically engineered neural tissue with neuroprosthetic and communications functionality. In *2017 13th International Conference and Expo on Emerging Technologies for a Smarter World (CEWIT)*, pages 1–6.

Delgado-Martínez, I., Badia, J., Pascual-Font, A., Rodríguez-Baeza, A., and Navarro, X. (2016). Fascicular topography of the human median nerve for neuroprosthetic surgery. *Frontiers in Neuroscience*, 10(286).

Diedrich, A., Charoensuk, W., Brychta, R. J., Ertl, A. C., and Shiavi, R. (2003). Analysis of raw microneurographic recordings based on wavelet de-noising technique and classification algorithm: wavelet analysis in microneurography. *IEEE Transactions on Biomedical Engineering*, 50(1):41–50.

Dimitrova, N. A., Dimitrov, A. G., and Dimitrov, G. V. (1999). Calculation of extracellular potentials produced by an inclined muscle fibre at a rectangular plate electrode. *Medical Engineering & Physics*, 21(8):583 – 588.

Dong, X. (2018). Current strategies for brain drug delivery. *Theranostics*, 8(6):1481–1493.

Durand, D. M., Grill, W. M., and Kirsch, R. (2005). *Electrical Stimulation of the Neuromuscular System*, pages 157–191. Springer US, Boston, MA.

Evans, M. S., Verma-Ahuja, S., Naritoku, D. K., and Espinosa, J. A. (2004). Intraoperative human vagus nerve compound action potentials. *Acta Neurologica Scandinavica*, 110(4):232–238.

Falces, J. R., Trigueros, A. M., Useros, L. G., Carreno, I. R., and Irujo, J. N. (2005). A mathematical analysis of sfap convolutional models. *IEEE Transactions on Biomedical Engineering*, 52(5):769–783.

Farra, R., Sheppard, N. F., McCabe, L., Neer, R. M., Anderson, J. M., Santini, J. T., Cima, M. J., and Langer, R. (2012). First-in-human testing of a wirelessly controlled drug delivery microchip. *Science Translational Medicine*, 4(122):122ra21–122ra21.

Farsad, N., Yilmaz, H. B., Eckford, A., Chae, C., and Guo, W. (2016). A comprehensive survey of recent advancements in molecular communication. *IEEE Communications Surveys Tutorials*, 18(3):1887–1919.

Felicetti, L., Femminella, M., Reali, G., and Liò, P. (2016). Applications of molecular communications to medicine: A survey. *Nano Communication Networks*, 7:27 – 45.

Feynman, R. P. (1992). There's plenty of room at the bottom [data storage]. *Journal of Microelectromechanical Systems*, 1(1):60–66.

Freeman, J. (1997). Introduction to forward-error-correcting coding. *NASA Reference Publication 1367*.

Freeman, R. L. (1998). Bits, symbols, bauds, and bandwidth. *IEEE Communications Magazine*, 36(4):96–99.

Galluccio, L., Palazzo, S., and Santagati, G. E. (2012). Capacity analysis for signal propagation in nanomachine-to-neuron communications. In *2012 IEEE International Conference on Communications (ICC)*, pages 6198–6202.

Gao, Y. and Wang, Z. L. (2007). Electrostatic potential in a bent piezoelectric nanowire. the fundamental theory of nanogenerator and nanopiezotronics. *Nano Letters*, 7:2499–2505.

Geddes, L. A. (2004). Accuracy limitations of chronaxie values. *IEEE Transactions on Biomedical Engineering*, 51(1):176–181.

Ghassemlooy, Z., Hayes, A. R., Seed, N. L., and Kaluarachchi, E. D. (1998). Digital pulse interval modulation for optical communications. *IEEE Communications Magazine*, 36(12):95–99.

Goldsmith, A. (2005). *Coding for Wireless Channels*, chapter 8, pages 228–283. Cambridge University Press.

Grill, W. M. and Mortimer, J. T. (1995). Stimulus waveforms for selective neural stimulation. *IEEE Engineering in Medicine and Biology Magazine*, 14(4):375–385.

Grill, W. M. and Mortimer, J. T. (1996). The effect of stimulus pulse duration on selectivity of neural stimulation. *IEEE Transactions on Biomedical Engineering*, 43(2):161–166.

Groves, D. A. and Brown, V. J. (2005). Vagal nerve stimulation: a review of its applications and potential mechanisms that mediate its clinical effects. *Neuroscience & Biobehavioral Reviews*, 29(3):493 – 500.

Guillory, K. and Normann, R. (1999). A 100-channel system for real time detection and storage of extracellular spike waveforms. *Journal of Neuroscience Methods*, 91(1):21 – 29.

Hallermann, S., de Kock, C. P. J., Stuart, G. J., and Kole, M. H. P. (2012). State and location dependence of action potential metabolic cost in cortical pyramidal neurons. *Nature Neuroscience*, 15(7):1007–1014.

Hampson, R. E., Song, D., Robinson, B. S., Fetterhoff, D., Dakos, A. S., Roeder, B. M., She, X., Wicks, R. T., Witcher, M. R., Couture, D. E., Laxton, A. W., Munger-Clary, H., Popli, G., Sollman, M. J., Whitlow, C. T., Marmarelis, V. Z., Berger, T. W., and Deadwyler, S. A. (2018). Developing a hippocampal neural prosthetic to facilitate human memory encoding and recall. *Journal of Neural Engineering*, 15(3):036014.

Hanisch, N. and Pierobon, M. (2017). Digital modulation and achievable information rates of thru-body haptic communications. In *Proc SPIE 10206*, volume 10206.

Harrison, R. R. (2003). A low-power integrated circuit for adaptive detection of action potentials in noisy signals. In *Proceedings of the 25th Annual International Conference of the IEEE Engineering in Medicine and Biology Society (IEEE Cat. No.03CH37439)*, volume 4, pages 3325–3328 Vol.4.

Helmers, S. L., Begnaud, J., Cowley, A., Corwin, H. M., Edwards, J. C., Holder, D. L., Kostov, H., Larsson, P. G., Levisohn, P. M., De Menezes, M. S., Stefan, H., and Labiner, D. M. (2012). Application of a computational model of vagus nerve stimulation. *Acta Neurologica Scandinavica*, 126(5):336–343.

Hendee, W. R. and Ritenour, E. R. (2003a). *Ultrasound Transducers*, chapter 20, pages 317–330. John Wiley & Sons, Ltd.

Hendee, W. R. and Ritenour, E. R. (2003b). *Ultrasound Waves*, pages 303–316. John Wiley & Sons, Inc.

Hinchet, R., Ferreira, J., Keraudy, J., Ardila, G., Pauliac-Vaujour, E., Mouis, M., and Montes, L. (2012). Scaling rules of piezoelectric nanowires in view of sensor and energy harvester integration. In *IEEE International Electron Devices Meeting (IEDM), 2012*, pages 6.2.1–6.2.4.

Ho, J. S., Kim, S., and Poon, A. S. Y. (2013). Midfield wireless powering for implantable systems. *Proceedings of the IEEE*, 101(6):1369–1378.

Hodgkin, A. L. and Huxley, A. F. (1952). A quantitative description of membrane current and its application to conduction and excitation in nerve. *The Journal of Physiology*, 117(4):500–544.

Howland, R. H. (2014). Vagus nerve stimulation. *Current Behavioral Neuroscience Reports*, 1(2):64–73.

Huang, Y.-J., Liao, H.-H., Huang, P.-L., Wang, T., Yang, Y.-J., Wang, Y.-H., and Lu, S.-S. (2012). An implantable release-on-demand cmos drug delivery soc using electrothermal activation technique. *J. Emerg. Technol. Comput. Syst.*, 8(2):12:1–12:22.

IEEE (2019). Ieee standard for safety levels with respect to human exposure to electric, magnetic, and electromagnetic fields, 0 hz to 300 ghz. *IEEE Std C95.1-2019 (Revision of IEEE Std C95.1-2005/ Incorporates IEEE Std C95.1-2019/Cor 1-2019)*, pages 1–312.

Ippolito, L. J. (2008). *Appendix B: Error Functions and Bit Error Rate*, pages 363–366. John Wiley & Sons, Ltd.

Jabaley, M. E., Wallace, W. H., and Heckler, F. R. (1980). Internal topography of major nerves of the forearm and hand: A current view. *The Journal of Hand Surgery*, 5(1):1 – 18.

Jalali, N., Briscoe, J., Woolliams, P., Stewart, M., Weaver, P. M., Cain, M., and Dunn, S. (2013). Passivation of zinc oxide nanowires for improved piezoelectric energy harvesting devices. *Journal of Physics: Conference Series*, 476:012131.

Jayaweera, H. M. P. C., Pathirana, W. P. M. R., and Muhtaroğlu, A. (2015). Fully integrated ultra-low voltage step-up converter with voltage doubling LC-tank for energy harvesting applications. *Journal of Physics: Conference Series*, 660:012017.

Jegadeesan, R., Nag, S., Agarwal, K., Thakor, N. V., and Guo, Y. (2015). Enabling wireless powering and telemetry for peripheral nerve implants. *IEEE Journal of Biomedical and Health Informatics*, 19(3):958–970.

Johari, P. and Jornet, J. M. (2018). Nanoscale optical wireless channel model for intra-body communications: Geometrical, time, and frequency domain analyses. *IEEE Transactions on Communications*, 66(4):1579–1593.

Johnson, B. C., Shen, K., Piech, D., Ghanbari, M. M., Li, K. Y., Neely, R., Carmena, J. M., Maharbiz, M. M., and Muller, R. (2018). Stimdust: A 6.5mm3, wireless ultrasonic peripheral nerve stimulator with 82 In *2018 IEEE Custom Integrated Circuits Conference (CICC)*, pages 1–4.

Joucla, S. and Yvert, B. (2012). Modeling extracellular electrical neural stimulation: From basic understanding to mea-based applications. *Journal of Physiology-Paris*, 106:146 – 158. Neuronal Ensemble Recordings in Integrative Neuroscience.

Katic, J., Rodriguez, S., and Rusu, A. (2018). A high-efficiency energy harvesting interface for implanted biofuel cell and thermal harvesters. *IEEE Transactions on Power Electronics*, 33(5):4125–4134.

Kerzenmacher, S., Ducrée, J., Zengerle, R., and von Stetten, F. (2008). Energy harvesting by implantable abiotically catalyzed glucose fuel cells. *Journal of Power Sources*, 182(1):1 – 17.

Khan, M. S. and Deng, H. (2017). Design and prototyping a smart deep brain stimulator: An autonomous neuro-sensing and stimulating electrode system. *IEEE Intelligent Systems*, 32(5):14–27.

Khodaei, A. and Pierobon, M. (2016a). An intra-body linear channel model based on neuronal subthreshold stimulation. In *2016 IEEE International Conference on Communications (ICC)*, pages 1–7.

Khodaei, A. and Pierobon, M. (2016b). Subthreshold linear modeling of dendritic trees: A computational approach. In *2016 38th Annual International Conference of the IEEE Engineering in Medicine and Biology Society (EMBC)*, pages 235–238.

Kim, A., Ochoa, M., Rahimi, R., and Ziaie, B. (2015). New and emerging energy sources for implantable wireless microdevices. *IEEE Access*, 3:89–98.

Kim, H. J., Hirayama, H., Kim, S., Han, K. J., Zhang, R., and Choi, J. W. (2017). Review of near-field wireless power and communication for biomedical applications. *IEEE Access*, 5:21264–21285.

Kodera, S., Gomez-Tames, J., and Hirata, A. (2018). Temperature elevation in the human brain and skin with thermoregulation during exposure to rf energy. *BioMedical Engineering OnLine*, 17(1):1.

Koopman, F. A., Chavan, S. S., Miljko, S., Grazio, S., Sokolovic, S., Schuurman, P. R., Mehta, A. D., Levine, Y. A., Faltys, M., Zitnik, R., Tracey, K. J., and Tak, P. P. (2016). Vagus nerve stimulation inhibits cytokine production and attenuates disease severity in rheumatoid arthritis. *Proceedings of the National Academy of Sciences*, 113(29):8284–8289.

Korivi, N. S. and Ajmera, P. K. (2011). Clip-on micro-cuff electrode for neural stimulation and recording. *Sensors and Actuators B: Chemical*, 160(1):1514 – 1519.

Krahl, S. (2012). Vagus nerve stimulation for epilepsy: A review of the peripheral mechanisms. *Surgical Neurology International*, 3:47–52.

Krishnaswamy, B., Austin, C. M., Bardill, J. P., Russakow, D., Holst, G. L., Hammer, B. K., Forest, C. R., and Sivakumar, R. (2013). Time-elapse communication: Bacterial communication on a microfluidic chip. *IEEE Transactions on Communications*, 61(12):5139–5151.

Kuncel, A. M. and Grill, W. M. (2004). Selection of stimulus parameters for deep brain stimulation. *Clinical Neurophysiology*, 115(11):2431 – 2441.

Kwon, C. H., Ko, Y., Shin, D., Kwon, M., Park, J., Bae, W. K., Lee, S. W., and Cho, J. (2018). High-power hybrid biofuel cells using layer-by-layer assembled glucose oxidase-coated metallic cotton fibers. *Nature Communications*, 9(1).

Larson, P. J. and Towe, B. C. (2011). Miniature ultrasonically powered wireless nerve cuff stimulator. In *2011 5th International IEEE/EMBS Conference on Neural Engineering*, pages 265–268.

Lazzi, G. (2005). Thermal effects of bioimplants. *IEEE Engineering in Medicine and Biology Magazine*, 24(5):75–81.

Lee, S., Yen, S. C., Sheshadri, S., Delgado-Martinez, I., Xue, N., Xiang, Z., Thakor, N. V., and Lee, C. (2016). Flexible epineural strip electrode for recording in fine nerves. *IEEE Transactions on Biomedical Engineering*, 63(3):581–587.

Leeson, M. S. and Higgins, M. D. (2012). Forward error correction for molecular communications. *Nano Communication Networks*, 3(3):161 – 167.

Lewicki, M. (1993). Bayesian modeling and classification of neural signals. *Neural Computation*, 6:1005–1030.

Loeb, G. and Peck, R. (1996). Cuff electrodes for chronic stimulation and recording of peripheral nerve activity. *Journal of Neuroscience Methods*, 64(1):95 – 103.

Lu, Y., Wang, X., Higgins, M. D., Noel, A., Neophytou, N., and Leeson, M. S. (2017). Energy requirements of error correction codes in diffusion-based molecular communication systems. *Nano Communication Networks*, 11:24 – 35.

MacKay, D. M. and McCulloch, W. S. (1952). The limiting information capacity of a neuronal link. *The bulletin of mathematical biophysics*, 14(2):127–135.

MacWilliams, F. and Sloane, N. (1977). *The Theory of Error-correcting Codes*, volume 16. North Holland Mathematical Library.

Madhavan, M., Mulpuru, S. K., McLeod, C. J., Cha, Y.-M., and Friedman, P. A. (2017). Advances and future directions in cardiac pacemakers: Part 2 of a 2-part series. *Journal of the American College of Cardiology*, 69(2):211 – 235.

Mahnam, A., Hashemi, S. M. R., and Grill, W. M. (2009). Measurement of the current distance relationship using a novel refractory interaction technique. *Journal of Neural Engineering*, 6(3):036005.

Malak, D. and Akan, O. B. (2013). A communication theoretical analysis of synaptic multiple-access channel in hippocampal-cortical neurons. *IEEE Transactions on Communications*, 61(6):2457–2467.

Malmivuo, J. and Plonsey, R. (1995). *Bioelectromagnetism - Principles and Applications of Bioelectric and Biomagnetic Fields*. Oxford University Press.

Maloney, J. M., Uhland, S. A., Polito, B. F., Sheppard, N. F., Pelta, C. M., and Santini, J. T. (2005). Electrothermally activated microchips for implantable drug delivery and biosensing. *Journal of Controlled Release*, 109(1):244 – 255. Proceedings of the Twelfth International Symposium on Recent Advances in Drug Delivery Systems.

Mani, B., Sarawagi, R., and Cherian, R. A. (2011). Review of the dimensions of the median nerve and carpal tunnel using sonography in asymptomatic adults. *Journal of Medical Imaging and Radiation Oncology*, 55(2):126–131.

Martinez, J., Pedreira, C., Ison, M. J., and Quiroga, R. Q. (2009). Realistic simulation of extracellular recordings. *Journal of Neuroscience Methods*, 184(2):285 – 293.

Martinez-Ramirez, D., Hu, W., Bona, A. R., Okun, M. S., and Shukla, A. W. (2015). Update on deep brain stimulation in parkinson's disease. *Translational Neurodegeneration*, 4(1):12.

McAdams, B. H. and Rizvi., A. A. (2016). An overview of insulin pumps and glucose sensors for the generalist. *Journal of clinical medicine*, 5(1).

McCahon, R. and Bedforth, N. (2007). Peripheral nerve block at the elbow and wrist. *Continuing Education in Anaesthesia, Critical Care & Pain*, 7(2):42–44.

McNeal, D. R. (1976). Analysis of a model for excitation of myelinated nerve. *IEEE Transactions on Biomedical Engineering*, BME-23(4):329–337.

Mesiti, F. and Balasingham, I. (2013). Nanomachine-to-neuron communication interfaces for neuronal stimulation at nanoscale. *IEEE Journal on Selected Areas in Communications*, 31(12):695–704.

Mortimer, J. T. and Bhadra, N. (2004). *Peripheral Nerve and Muscle Stimulation*, chapter 4.2, pages 638–682. World Scientific Pub.

Muller, R., Gambini, S., and Rabaey, J. M. (2012). A 0.013mm^2, 5μW, DC-coupled neural signal acquisition IC with 0.5 v supply. *IEEE Journal of Solid-State Circuits*, 47(1):232–243.

Nandedkar, S. and Stalberg, E. (1983). Simulation of single muscle fibre action potentials. *Medical and Biological Engineering and Computing*, 21:158–165.

Naples, G. G., Mortimer, J. T., Scheiner, A., and Sweeney, J. D. (1988). A spiral nerve cuff electrode for peripheral nerve stimulation. *IEEE Transactions on Biomedical Engineering*, 35(11):905–916.

Neely, R. M., Piech, D. K., Santacruz, S. R., Maharbiz, M. M., and Carmena, J. M. (2018). Recent advances in neural dust: towards a neural interface platform. *Current Opinion in Neurobiology*, 50:64 – 71. Neurotechnologies.

Oluigbo, C. O., Salma, A., and Rezai, A. R. (2012). Deep brain stimulation for neurological disorders. *IEEE Reviews in Biomedical Engineering*, 5:88–99.

O'Sullivan, D. and Swallow, M. (1968). The fibre size and content of the radial and sural nerves. *Journal of Neurology, Neurosurgery & Psychiatry*, 31.

Ozeri, S. and Shmilovitz, D. (2010). Ultrasonic transcutaneous energy transfer for powering implanted devices. *Ultrasonics*, 50(6):556 – 566.

Parcerisa-Giné, L. and Akyildiz, I. F. (2009). Molecular communication options for long range nanonetworks. *Computer Networks*, 53(16):2753 – 2766.

Pereyra, P. M., Zhang, W., Schmidt, M., and Becker, L. E. (1992). Development of myelinated and unmyelinated fibers of human vagus nerve during the first year of life. *Journal of the Neurological Sciences*, 110(1):107 – 113.

Pikul, J. H., Gang Zhang, H., Cho, J., Braun, P. V., and King, W. P. (2013). High-power lithium ion microbatteries from interdigitated three-dimensional bicontinuous nanoporous electrodes. *Nature Communications*, 4:1732.

Piro, G., Yang, K., Boggia, G., Chopra, N., Grieco, L. A., and Alomainy, A. (2015). Terahertz communications in human tissues at the nanoscale for healthcare applications. *IEEE Transactions on Nanotechnology*, 14(3):404–406.

Planitzer, U., Steinke, H., Meixensberger, J., Bechmann, I., Hammer, N., and Winkler, D. (2014). Median nerve fascicular anatomy as a basis for distal neural prostheses. *Annals of Anatomy - Anatomischer Anzeiger*, 196(2â€"3):144 – 149.

Plonsey, R. (1974). The active fiber in a volume conductor. *IEEE Transactions on Biomedical Engineering*, BME-21(5):371–381.

Polasek, K. H., Hoyen, H. A., Keith, M. W., and Tyler, D. J. (2007). Human nerve stimulation thresholds and selectivity using a multi-contact nerve cuff electrode. *IEEE Transactions on Neural Systems and Rehabilitation Engineering*, 15(1):76–82.

Proctor, C. M., Slézia, A., Kaszas, A., Ghestem, A., del Agua, I., Pappa, A.-M., Bernard, C., Williamson, A., and Malliaras, G. G. (2018). Electrophoretic drug delivery for seizure control. *Science Advances*, 4(8).

Qin, Y., Howlader, M. M., Deen, M. J., Haddara, Y. M., and Selvaganapathy, P. R. (2014). Polymer integration for packaging of implantable sensors. *Sensors and Actuators B: Chemical*, 202:758 – 778.

Rabaey, J., Mark, M., Chen, D., Sutardja, C., Tang, C., Gowda, S., Wagner, M., and Werthimer, D. (2011). Powering and communicating with mm-size implants. In *Design, Automation Test in Europe Conference Exhibition (DATE), 2011*, pages 1–6.

Ramezani, H. and Akan, O. B. (2018). Information capacity of vesicle release in neuro-spike communication. *IEEE Communications Letters*, 22(1):41–44.

Ramezani, H., Khan, T., and Akan, O. B. (2018). Sum rate of miso neuro-spike communication channel with constant spiking threshold. *IEEE Transactions on NanoBioscience*, 17(3):342–351.

Ranck, J. B. (1975). Which elements are excited in electrical stimulation of mammalian central nervous system: A review. *Brain Research*, 98(3):417 – 440.

Rapoport, B. I., Kedzierski, J. T., and Sarpeshkar, R. (2012). A glucose fuel cell for implantable brain–machine interfaces. *PLOS ONE*, 7(6):1–14.

Rattay (1999). The basic mechanism for the electrical stimulation of the nervous system. *Neuroscience*, 89:335–346.

Rattay, F. (1989). Analysis of models for extracellular fiber stimulation. *IEEE Transactions on Biomedical Engineering*, 36(7):676–682.

Rattay, F. (2008). Current distance relations for fiber stimulation with pointsources. *IEEE Transactions on Biomedical Engineering*, 55(3):1122–1127.

Reed, I. S. and Solomon, G. (1960). Polynomial codes over certain finite fields. *Journal of the Society for Industrial and Applied Mathematics*, 8.

Ritter, R., Handwerker, J., Liu, T., and Ortmanns, M. (2014). Telemetry for implantable medical devices: Part 1 - media properties and standards. *IEEE Solid-State Circuits Magazine*, 6(2):47–51.

Rivnay, J., Wang, H., Fenno, L., Deisseroth, K., and Malliaras, G. G. (2017). Next-generation probes, particles, and proteins for neural interfacing. *Science Advances*, 3(6).

Roes, M., Duarte, J., Hendrix, M., and Lomonova, E. (2013). Acoustic energy transfer: A review. *IEEE Transactions on Industrial Electronics*, 60(1):242–248.

Rosenfalck, P. (1969). Intra and extracellular fields of active nerve and muscle fibers. a physico-mathematical analysis of different models. *Acta Physiologica Scandinavica*.

Rutkove, S. (2007). Introduction to volume conduction. In *The Clinical Neurophysiology Primer*. Humana Press.

Salam, M. T., Mirzaei, M., Ly, M. S., Nguyen, D. K., and Sawan, M. (2012). An implantable closedloop asynchronous drug delivery system for the treatment of refractory epilepsy. *IEEE Transactions on Neural Systems and Rehabilitation Engineering*, 20(4):432–442.

Sanni, A., Vilches, A., and Toumazou, C. (2012). Inductive and ultrasonic multi-tier interface for low-power, deeply implantable medical devices. *IEEE Transactions on Biomedical Circuits and Systems*, 6(4):297–308.

Santagati, G. E. and Melodia, T. (2017). Experimental evaluation of impulsive ultrasonic intra-body communications for implantable biomedical devices. *IEEE Transactions on Mobile Computing*, 16(2):367–380.

Santagati, G. E., Melodia, T., Galluccio, L., and Palazzo, S. (2013). Ultrasonic networking for e-health applications. *IEEE Wireless Communications*, 20(4):74–81.

Santagati, G. E., Melodia, T., Galluccio, L., and Palazzo, S. (2015). Medium access control and rate adaptation for ultrasonic intrabody sensor networks. *IEEE/ACM Transactions on Networking*, 23(4):1121–1134.

Santini Jr, J. T., Cima, M. J., and Langer, R. (1999). A controlled-release microchip. *Nature*, 397:335–338.

Sarpeshkar, R. (2012). Universal principles for ultra low power and energy efficient design. *IEEE Transactions on Circuits and Systems II: Express Briefs*, 59(4):193–198.

Schnitzlein, H. N., Rowe, L. C., and Hoffman, H. H. (1958). The myelinated component of the vagus nerves in man. *The Anatomical Record*, 131(4):649–667.

Schoonhoven, R., Stegeman, D. F., and Oosterom, A. V. (1986a). The forward problem in electroneurography ii: Comparson of models. *IEEE Transactions on Biomedical Engineering*, BME-33(3):335–341.

Schoonhoven, R., Stegeman, D. F., van Oosterom, A., and Dautzenberg, G. F. M. (1988). The inverse problem in electroneurography. i. conceptual basis and mathematical formulation. *IEEE Transactions on Biomedical Engineering*, 35(10):769–777.

Schoonhoven, R., Stegeman, D. F., and Weerd, J. P. C. D. (1986b). The forward problem in electroneurography i: A generalized volume conductor model. *IEEE Transactions on Biomedical Engineering*, BME-33(3):327–334.

Schwartz, A. B., Cui, X. T., Weber, D., and Moran, D. W. (2006). Brain-controlled interfaces: Movement restoration with neural prosthetics. *Neuron*, 52(1):205 – 220.

Seo, D., Carmena, J. M., Rabaey, J. M., Maharbiz, M. M., and Alon, E. (2015a). Model validation of untethered, ultrasonic neural dust motes for cortical recording. *Journal of Neuroscience Methods*, 244:114 – 122. Brain Computer Interfaces; Tribute to Greg A. Gerhardt.

Seo, D., Neely, R., Shen, K., Singhal, U., Alon, E., Rabaey, J., Carmena, J., and Maharbiz, M. (2016). Wireless recording in the peripheral nervous system with ultrasonic neural dust. *Neuron*, 91(3):529 – 539.

Seo, D., Tang, H. Y., Carmena, J. M., Rabaey, J. M., Alon, E., Boser, B. E., and Maharbiz, M. M. (2015b). Ultrasonic beamforming system for interrogating multiple implantable sensors. In *2015 37th Annual International Conference of the IEEE Engineering in Medicine and Biology Society (EMBC)*, pages 2673–2676.

Seriwala, H. M., Khan, M. S., Munir, M. B., bin Riaz, I., Riaz, H., Saba, S., and Voigt, A. H. (2016). Leadless pacemakers: A new era in cardiac pacing. *Journal of Cardiology*, 67(1):1 – 5.

Shannon, C. E. (1949). Communication in the presence of noise. *Proceedings of the IRE*, 37(1):10–21.

Shannon, R. V. (1992). A model of safe levels for electrical stimulation. *IEEE Transactions on Biomedical Engineering*, 39(4):424–426.

Sherwood, W. E. (2013). *FitzHugh–Nagumo Model*, pages 1–11. Springer New York, New York, NY.

Shi, Q., Wang, T., and Lee, C. (2016). Mems based broadband piezoelectric ultrasonic energy harvester (pueh) for enabling self-powered implantable biomedical devices. *Scientific Reports*, 6.

Snyder A.W., L. J. (1983). Pulse spreading. In *Optical Waveguide Theory*. Springer, Boston, MA.

Stegeman, D. and Weerd, J. D. (1982). Modelling compound action potentials of peripheral nerves in situ. i. model description; evidence for a non-linear relation between fibre diameter and velocity. *Electroencephalography and Clinical Neurophysiology*, 54(4):436 – 448.

Stegeman, D. F., Schoonhoven, R., Dautzenberg, G. F. M., and Moleman, J. (1988). The inverse problem in electroneurography. ii. computational aspects and evaluation using simulated data. *IEEE Transactions on Biomedical Engineering*, 35(10):778–788.

Stewart, J. D. (2003). Peripheral nerve fascicles: Anatomy and clinical relevance. *Muscle & Nerve*, 28(5):525–541.

Struijk, J. (1997). The extracellular potential of a myelinated nerve fiber in an unbounded medium and in nerve cuff models. *Biophysical Journal*, 72(6):2457 – 2469.

Sunderland, S. (1945). The intraneural topography of the radial, median and ulnar nerves. *Brain*, 68(4).

Sweeney, J. D., Ksienski, D. A., and Mortimer, J. T. (1990). A nerve cuff technique for selective excitation of peripheral nerve trunk regions. *IEEE Transactions on Biomedical Engineering*, 37(7):706–715.

Tarler, M. D. and Mortimer, J. T. (2004). Selective and independent activation of four motor fascicles using a four contact nerve-cuff electrode. *IEEE Transactions on Neural Systems and Rehabilitation Engineering*, 12(2):251–257.

Taynnan Barros, M., Balasubramaniam, S., and Jennings, B. (2015). Comparative end-to-end analysis of ca2+-signaling-based molecular communication in biological tissues. *IEEE Transactions on Communications*, 63(12):5128–5142.

Teshome, A. K., Kibret, B., and Lai, D. T. H. (2019). A review of implant communication technology in wban: Progress and challenges. *IEEE Reviews in Biomedical Engineering*, 12:88–99.

Theis, T. N. and Solomon, P. M. (2010). In quest of the "next switch": Prospects for greatly reduced power dissipation in a successor to the silicon field-effect transistor. *Proceedings of the IEEE*, 98(12):2005–2014.

Uguz, I., Proctor, C. M., Curto, V. F., Pappa, A.-M., Donahue, M. J., Ferro, M., Owens, R. M., Khodagholy, D., Inal, S., and Malliaras, G. G. (2017). A microfluidic ion pump for in vivo drug delivery. *Advanced Materials*, 29(27).

Veletić, M., Floor, P. A., Chahibi, Y., and Balasingham, I. (2016). On the upper bound of the information capacity in neuronal synapses. *IEEE Transactions on Communications*, 64(12):5025–5036.

Wang, X., Gao, Y., Wei, Y., and Wang, Z. (2009). Output of an ultrasonic wave-driven nanogenerator in a confined tube. *Nano Research*, 2(3):177–182.

Wang, X., Liu, J., Song, J., , and Wang, Z. L. (2007a). Integrated nanogenerators in biofluid. *Nano Letters*, 7(8):2475–2479. PMID: 17604406.

Wang, X., Song, J., Liu, J., and Wang, Z. L. (2007b). Direct-current nanogenerator driven by ultrasonic waves. *Science*, 316(5821):102–105.

Wang, Z. L. (2008). Towards self-powered nanosystems: From nanogenerators to nanopiezotronics. *Advanced Functional Materials*, 18(22):3553–3567.

Wang, Z. L. and Song, J. (2006). Piezoelectric nanogenerators based on zinc oxide nanowire arrays. *Science*, 312(5771):242–246.

Ward, M. P., Qing, K. Y., Otto, K. J., Worth, R. M., John, S. W. M., and Irazoqui, P. P. (2015). A flexible platform for biofeedback-driven control and personalization of electrical nerve stimulation therapy. *IEEE Transactions on Neural Systems and Rehabilitation Engineering*, 23(3):475–484.

Wicker, S. B. (1995). *Error Control Systems for Digital Communication and Storage*. Prentice Hall.

Wijesinghe, R. S., Gielen, F. L. H., and Wikswo, J. P. (1991). A model for compound action potentials and currents in a nerve bundle i: The forward calculation. *Annals of Biomedical Engineering*, 19(1):43–72.

Wirdatmadja, S., Johari, P., Desai, A., Bae, Y., Stachowiak, E. K., Stachowiak, M. K., Jornet, J. M., and Balasubramaniam, S. (2019). Analysis of light propagation on physiological properties of neurons for nanoscale optogenetics. *IEEE Transactions on Neural Systems and Rehabilitation Engineering*, 27(2):108–117.

Xia, M. and Aissa, S. (2015). On the efficiency of far-field wireless power transfer. *IEEE Transactions on Signal Processing*, 63(11):2835–2847.

Xu, H., Handwerker, J., and Ortmanns, M. (2014). Telemetry for implantable medical devices: Part 2 - power telemetry. *IEEE Solid-State Circuits Magazine*, 6(3):60–63.

Yang, Z., Erturk, A., and Zu, J. (2017). On the efficiency of piezoelectric energy harvesters. *Extreme Mechanics Letters*, 15:26 – 37.

Yu, H., Xiong, W., Zhang, H., Wang, W., and Li, Z. (2014). A parylene self-locking cuff electrode for peripheral nerve stimulation and recording. *Journal of Microelectromechanical Systems*, 23(5):1025–1035.

Zhang, F., Aghagolzadeh, M., and Oweiss, K. (2012). A fully implantable, programmable and multimodal neuroprocessor for wireless, cortically controlled brain-machine interface applications. *J. Signal Process. Syst.*, 69(3):351–361.

Appendix A

Examples of Matlab Coding used in this Thesis

1. Simulation of a single fibre action potential (SFAP) propagating along a neuron.

```matlab
1  %calculate the single fibre action potential (SFAP)
2  %with respect to time based on Nandedkers IAP model
3  %This requires a single differentiation of a modified
4  %Rosenfalck model convoluted with a weighting function
5  clear t;
6  clearvars;
7  %diameter of the axon in micrometres
8  dia=input('Diameter of the neuron in micrometres:');
9  %conduction velocity in metres per second or mm per ms
10 %v in m/s is 6 times the diameter in microm.
11 vel=dia*6;
12 %time range in milliseconds
13 trange= input('Time range in milliseconds:');
14 tstep=input('Time step in milliseconds:');
15 %set electrode position w.r.t excitation point
16 %longitudinal distance of electrode from excitation in mm
17 zed=input('Longitudinal distance in mm:');
18 %distance of electrode from fibre in mm
19 raddis=input('Perpendicular distance of electrode from fibre ...
       in mm:');
20 %conductivity in siemens per millimetre from Plonsey and Joucla
21 coni=.001;
22 cone=.0003;
23 %radius is half the diameter expressed in millimetres
24 rad=(dia/2)*10^-3;
```

```matlab
25  %compute the constant for membrane current
26  %this may vary and include different parameters
27  Fac=(rad^2*coni)/(4*cone*vel);
28  %use the derivative based on the Nandedkar formula in time
29  alpha=36860;
30  beta=8;
31  gamma=70;
32  %set up variables
33  syms t iap1
34  %empirical formula for IAP
35  iap1=alpha*(t^3)*exp(-beta*t)-gamma;
36  %differentiate once as part of dimitrova process
37  iap2=diff(iap1,t,1);
38  %now assign values to get source model
39  %time range in milliseconds
40  t=0:tstep:trange;
41  %find the number of elements in t for later plotting
42  tsize=size(t,2);
43  %expand formulae to allow for correct computation by vectors
44  iap3=alpha.*(t.^3).*exp(-beta.*t)-gamma;
45  %first diff of iap1
46  iap4=110580.*(t.^2).*exp(-8.*t) - 294880.*(t.^3).*exp(-8.*t);
47  %correction factor
48  iap5=Fac.*iap4;
49  %next part is to calculate weighting function based on radial ...
        distance
50  %calculate full distance, Pythagorean
51  Dis1=((zed-vel.*t).^2 +raddis^2).^1.5;
52  %first diff of Pythagorean, as part of DD formulation
53  Dis2=vel*(zed-vel.*t);
54  Dis3=Dis2./Dis1;
55  %next perform convolution
56  Sfapdim=tstep*conv(iap5,Dis3);
57  %Sfapdim is twice the length of the time steps.
58  %Plot data using t to reduce the range of Sfapdim
59  %and convert the millivolt output to microvolts
60  plot(t,Sfapdim(1,1:tsize)*10^3,'-.r', 'LineWidth',2)
61  axis([0 7 -0.05 0.05])
62  grid on
63  grid minor
64  ylabel('Voltage in {\mu}V ','FontSize',10)
65  xlabel('Time in mS','FontSize',10)
```

2. BER plots for Hamming, BCH and Golay FEC methods.

```matlab
1  %Calculate Compound Action Potentials (CAP)
2  %and SNR\BER for the same set of Vagus neurons over
3  %a range of distance and time. Calculate coding gain for
4  %Hamming, BCH and Golay coding.
5  clear
6  %maximum longitudinal distance of electrode from excitation ...
      in mm
7  zedmax=input('Longitudinal max distance in mm:');
8  %set range of distances
9  zedrange=1:1:zedmax;
10 zedsize=size(zedrange,2);
11 noiselevel=input('Minimum Noise Level in {\mu}V:');
12 %calculate the range of amplitudes using a unique exp function
13 %for the vagus nerve derived from a range of CAPs
14 amprange=49.21*exp(-.0068.*zedrange);
15 %allow for rms of  this value and square it for power
16 amppower1=(amprange.^2)./2;
17 noisepower1=noiselevel.^2;
18 %calculate snr and EbN0 as a ratio and then as dB
19 snr11=amppower1./(noisepower1);
20 EbN0=amppower1./(noisepower1*2);
21 snrdb11=10*log10(snr11);
22 %calculate OOK bit error rate (BER)
23 per11=EbN0.^.5;
24 ber11=.5.*erfc(per11);
25 %calculate Hamming 12 8 3 snr using 8/12 (.67)
26 snr15= .67*EbN0;
27 snrdb15=10*log10(snr15);
28 %calculate initial coded ber for Hamming 12 8 3
29 per15=snr15.^.5;
30 ber15=.5.*erfc(per15);
31 %calculate decoded word error for Hamming 12 8 3
32 %using binomial 12C2 for one error detected +1
33 wordec15=66.*(ber15).^2.*(1-ber15).^10;
34 %calculate decoded bit error for Hamming 12 8 3
35 %using dmin/n (.25)
36 berdec15=0.25.*wordec15;
37 %calculate BCH 15 7 5 snr using 7/15 (.47)
38 snrBCH= .47*EbN0;
39 snrdbBCH=10*log10(snrBCH);
40 %calculate initial coded ber for BCH 15 7 5
```

```matlab
41  perBCH=snrBCH.^.5;
42  berBCH=.5.*erfc(perBCH);
43  %calculate decoded word error for BCH 15 7 5
44  %using binomial 15C3 for two errors corrected plus 1
45  wordecBCH=455.*(berBCH).^3.*(1-berBCH).^12;
46  %calculate decoded bit error for BCH 15 7 5
47  %using dmin/n (.34)
48  berdecBCH=0.34.*wordecBCH;
49  %calculate Golay 19 8 7 snr using 8/19 (.42)
50  snrGOL= .42*EbN0;
51  snrdbGOL=10*log10(snrGOL);
52  %calculate initial coded ber for golay 19 8 7
53  perGOL=snrGOL.^.5;
54  berGOL=.5.*erfc(perGOL);
55  %calculate decoded word error for Golay 19 8 7
56  %using binomial 19C4 for three errors corrected plus 1
57  wordecGolay=3876.*(berGOL).^4.*(1-berGOL).^15;
58  %calculate decoded bit error for Golay 19 8 7
59  %using dmin/n (.37)
60  berdecGolay=0.37.*wordecGolay;
61  colormap jet
62  semilogy(zedrange,ber11,'-r', 'LineWidth',2)
63  hold on
64  semilogy(zedrange,berdec15,'--k', 'LineWidth',2)
65  semilogy(zedrange,berdecBCH,':b', 'LineWidth',2)
66  semilogy(zedrange,berdecGolay,'-.k', 'LineWidth',2)
67  xlim([0 100])
68  grid on
69  hold off
70  xlabel('Transmission Range in mm','FontSize',10)
71  ylabel('BER','FontSize',10)
72  legend('BER uncoded','BER Hamming {\cdot}','BER BCH','BER ...
          Golay','Location','southeast' )
73  set(gca,'Fontsize',10)
```